Source Parameters Inversion for Recent Large Undersea Earthquakes from GRACE Data

Dissertation

Presented in Partial Fulfillment of the Requirements for the Degree Doctor of Philosophy in the Graduate School of The Ohio State University

By

Chunli Dai

Graduate Program in Geodetic Science

The Ohio State University

2015

Committee:

Prof. C.K. Shum, Advisor

Prof. Michael Bevis

Prof. Christopher Jekeli

Abstract

The north component of gravity and gravity gradient changes from the Gravity Recovery And Climate Experiment (GRACE) are used to study the coseismic gravity change for five earthquakes over the last decade: the 2004 Sumatra-Andaman earthquake, the 2007 Bengkulu earthquake, the 2010 Maule, Chile earthquake, the 2011 Tohoku earthquake, and the 2012 Indian Ocean earthquakes. We demonstrate the advantage of these north components to reduce north-south stripes and preserve higher spatial resolution signal in GRACE Level 2 (L2) monthly Stokes Coefficients data products. By using the high spherical harmonic degree (up to degree 96) data products and the innovative GRACE data processing approach developed in this study, the retrieved gravity change is up to –34±1.4 μGal for the 2004 Sumatra and 2005 Nias earthquakes, which is by far the highest coseismic signal retrieved among published studies. Our study reveals the detectability of earthquakes as small as Mw 8.5 (i.e., the 2007 Bengkulu earthquake) from GRACE data. The localized spectral analysis is applied as an efficient method to determine the practical spherical harmonic truncation degree leading to acceptable signal-to-noise ratio, and to evaluate the noise level for each component of gravity and gravity gradient change of the seismic deformations.

By establishing the linear algorithm of gravity and gravity gradient change with respect to the double-couple moment tensor, the point source parameters are estimated through the least squares adjustment combined with the simulated annealing algorithm. The

GRACE-inverted source parameters generally agree well with the slip models estimated using other data sets, including seismic, GPS, or combined data. For the 2004 Sumatra-Andaman and 2005 Nias earthquakes, GRACE data produce a shallower centroid depth (9.1 km) compared to the depth (28.3 km) from GPS data, which may be explained by the closer-to-trench centroid location and by the aseismic slip over the shallow region. For the 2011 Tohoku earthquake, the inversions from two different GRACE data products and two different forward modeling produce similar source characteristics, with the centroid location southwest of and the slip azimuth 10° larger than the GPS/seismic solutions. The GRACE-estimated dip angles are larger than that from GPS/seismic data for the 2004 Sumatra-Andaman and 2005 Nias earthquakes, the 2010 Maule, Chile earthquake, and the 2007 Bengkulu earthquake. These differences potentially show the additional offshore constraint from GRACE data, compared to GPS/seismic data. With more accurate and higher spatial resolution measurements anticipated from the GRACE Follow-on mission, with a scheduled launch date in 2017, we anticipate the data will be sensitive to even smaller earthquake signals. Therefore, GRACE type observations will hopefully become a more viable measurement to further constrain earthquake focal mechanisms.

Acknowledgements

I gratefully thank my advisor, Prof. C.K. Shum, who has been guiding the research direction for me ever since I came to OSU. I am open-minded by his extensive knowledge, various pioneering ideas, and intuitions to the frontier research, but also amazed by how much he values students' research interest and encourages independent studies. I thank him for offering broad learning opportunities to me, and I appreciate his training on my English writing skills, on expanding my knowledge in seismology, as well as the training on developing skills over broad research topics and collaborating with other experts. Moreover, I am grateful for his care to students' health and daily lives.

I thankfully acknowledge Dr. Junyi Guo, Ohio State University, who has provided very useful research guidance and technical assistance throughout my PhD research. Dr. Guo is always happy to spend his valuable time on helping solving my questions every time I knock on his door. I really appreciate his insightful suggestions on how to do research, appreciate his support on the theoretical model prediction, and appreciate him pointing out the keys to my each question.

The initial research benefited from help from Dr. Lei Wang at the Ohio State University. I thank Lei for his guidance and suggestions on how to balance different tasks in PhD study. I appreciate his perceptive suggestions on research directions. Also, I thank him for generously offering his codes and software for me to follow up his research.

I'd like to thank Dr. Rongjiang Wang, GFZ, for his collaboration, generously sharing his dislocation software and providing his various inverted models for the 2011 Tohoku earthquake. I would also like to thank Dr. Frederik Simons, Princeton University, for valuable intellectual exchanges and for his open software on localized spectral analysis. I thank Dr. Jeff Freymueller, University of Alaska, for his helpful suggestions on sensitivity analysis. I acknowledge Drs. Shengji Wei, Han Yue, and David Sandwell for providing their coseismic and postseismic slip models of the 2011 Tohoku earthquake. I appreciate the valuable discussion with Dr. Shengji Wei on the benefits and limits from GPS data and GRACE data. I thank other seismologists and geodesists at the USGS and other institutes for providing various data associated with the earthquakes chosen in this study and the associated inverted slide models.

I acknowledge the valuable suggestions and comments from Profs. Michael Bevis and Christopher Jekeli on my dissertation. I'd also like to thank our teachers in Earth Science, who teach us the fundamental knowledge and skills for our future research.

I am thankful to Mr. Peter Luk for his assistance and help through out my study. Thanks to Mrs. Mary Shum for her hospitality and care for us. Many thanks to my classmates, student-colleagues, who enrich my student lives, and leave me good memories.

Thanks to my hubby Kun Shang. I benefit a lot from the discussions with him. He is always patient to my questions and many times lead me out of puzzles. Last but not the least, I am grateful for my parents, who give me the motivation to move forward.

This research is primarily supported by NASA's Earth and Space Science Fellowship (ESSF) Program (Grant NNX12AO06H), partially supported by National Science Foundation (NSF) Division of Earth Sciences (Grant EAR-1013333). GRACE data products are from NASA's PODAAC via Jet Propulsion Laboratory/California Institute of Technology (JPL), University of Texas Center for Space Research (CSR), and GeoForschungsZentrum Potsdam (GFZ). Preliminary GPS time series provided by the ARIA team at JPL and Caltech. All original GEONET RINEX data were provided to California Institute of Technology by the Geospatial Information Authority (GSI) of Japan. Some figures in this paper were generated using the Generic Mapping Tools (GMT) [*Wessel and Smith*, 1991]. This work was also supported in part by an allocation of computing resources from the Ohio Supercomputer Center (http://www.osc.edu).

Vita

2007.....B. Sc. Geophysics, Wuhan University, Wuhan, China, 2007

2011.....M. Sc. Astrometry and Celestial Mechanics, Chinese Academy of Sciences, Shanghai, China

2012.....M. Sc. Geodetic Science, The Ohio State University, Columbus, Ohio, USA, 2012

2009 to present .....Graduate Research Assistant, Division of Geodetic Science, School of Earth Sciences, The Ohio State University

Publications

Dai, C., C. Shum, R. Wang, L. Wang, J. Guo, K. Shang, and B. Tapley, Improved Constraints on Seismic Source Parameters of the 2011 Tohoku Earthquake from GRACE Gravity and Gravity Gradient Changes, *Geophys. Res. Lett.*, 41, doi:10.1002/2013GL059178, 2014.

Dai, C.L., Research on the Application of GPS/GNSS, Chinese Academy of Sciences, Master Thesis, 2011.

Guo, J., Y.B. Li, **C. Dai**, C. Shum, A technique to improve the accuracy of Earth orientation prediction algorithms based on least squares extrapolation, *J. Geodynamics*, 70, 36-48, 2013.

Iz, H.B., C. Shum, **C.L. Dai**, Polyaxial figures of the Moon from the lunar reconnaissance orbiter laser altimetry and multi-mission synthesis of the lunar shape, *J. Geodetic Science*, 2(2), 107–112, doi:10.2478/B/v10156-011-0031-x, 2012.

Wang, L., C.K. Shum, F. J Simons, Byron Tapley, **C.L. Dai**, Coseismic and Postseismic Deformation of the 2011 Tohoku-Oki Earthquake Constrained by GRACE Gravimetry, *Geophys. Res. Lett.*, 39 (7), L07301, doi:10.1029/2012GL051104, 2012.

Iz, B., X. Ding, **C. Dai**, C. Shum, Polyaxial figures of the Moon, *J. Geodetic Science*, 1(4), 348–354, doi:10.2478/v10156-011-0013-z, 2011.

Iz, H. B., C.K. Shum, Y.Q. Chen, **C.L. Dai**, Improved Geometric Lunar Figure from Chang'E-1 and SELENE Laser Altimetry, *Journal of Applied Geodesy*, Vol. 15, 1–12, doi:10.1515/JAG.2011.011, 2011.

Iz, H.B., C.K. Shum, X.L. Ding, **C.L. Dai**, Orientation of the Geometrically Best fitting Triaxial Lunar Ellipsoid with Respect to the Mean Earth/Polar Axis Reference Frame, *Jl. of Geodetic Sci.*, 1, 52–58, 2011.

Shum, C., K. Tseng, C. Kuo, K. Cheng, **C.L. Dai**, J. Duan, Z. Huang, H. Lee, S. Song, M. Yang, W. Zhu, Validation of GNSS-Observed Climate Variables Over Tibetan Plateau, *Jl. Astronau. Sci.*, 43, 1, 9–16, 2011.

Sun, J., **C.L. Dai**, N.C. Jian, Y.H. Zhou, G.G. Wang, J.S. Ping, Using VLBI-CONT 08 data to measure the daily ERP variations in Summer (in Chinese), *Chinese Science Bulletin*, 55: 2177–2182, 2010.

Tseng, K., C. Shum, Y. Yi, **C.L. Dai,** H. Lee, D. Bilitza, A. Komjathy, C. Kuo, J. Ping, M. Schmidt, Regional Validation of Jason-2 Dual-Frequency Ionosphere Delays, *Marine Geodesy*, 33(S1), 272–284, 2010.

Fields of Study

Major Field: Geodetic Science

Table of Contents

Abstract ii

Acknowledgements iv

Vita vii

Publications vii

Fields of Study viii

Table of Contents ix

List of Tables xi

List of Figures xiii

Chapter 1. Introduction 1

1.1 Traditional methods to study earthquakes and their limitations. 1

1.2 GRACE data on constraining focal mechanisms 3

1.3 Outline 5

Chapter 2. Forward Modeling and Source Parameters Inversion Method 7

2.1 Forward modeling based on finite fault model 7

2.1.1 Gravity and gravity gradient change predicted from slip distribution model 7

2.1.2 Sensitivity analysis of gravity and gravity gradient change to different finite fault models 16

2.2 Forward modeling based on double-couple point source 23

2.2.1 Double-couple point source 23

2.2.2 Linear algorithm between gravity change and point-source moment tensor 27

2.3 The least-squares estimation of double-couple point source 33

2.3.1 Estimation from GRACE data 34

2.3.2 Estimation from GPS data 37
2.3.3 Joint Estimation from GRACE data and GPS data 39
2.4 Simulation 40

Chapter 3. Improved GRACE Data Processing 49
3.1 Heaviside step function for coseismic gravity change detection 49
3.2 Localized spectral analysis 55
3.3 North component of gravity and gravity gradient change 57

Chapter 4. Inversion for Source Parameters 63
4.1 Inversion for finite fault model with the Simulated Annealing algorithm 63
4.1.1 Simulated Annealing algorithm 63
4.1.2 The 2011 Tohoku earthquake 65
4.2 Inversion of point source parameters for recent large undersea earthquakes 78
4.2.1 The 2004 Sumatra-Andaman and 2005 Nias earthquakes 78
4.2.2 The 2011 Tohoku earthquake 95
4.2.3 The 2010 Maule, Chile earthquake 97
4.2.4 The 2012 Indian Ocean earthquakes 108
4.2.5 The 2007 Bengkulu earthquake 119

Chapter 5. Conclusions 129

References 133

Appendix A. Depth of the Slip Model 142

Appendix B. Derivation of Gravity Disturbance and Gravity Gradient Tensor Disturbance from Spherical Harmonic Coefficients 145

Appendix C. Retrieve Centroid Moment Tensor and Location From Finite Fault Slip Distribution Model 148

List of Tables

Table 2.1. Accuracy and precision of estimated parameters for several schemes. 47

Table 2.2. The correlation between parameters. 48

Table 4.1. Comparison of Fault Parameters..... 76

Table 4.2. RMS and relative differences between the GRACE observation and two slip models predictions. 77

Table 4.3. Earth Model [*Chlieh et al.,* 2007] 82

Table 4.4. Comparison of Source Parameters..... 93

Table 4.5. The correlation between parameters 93

Table 4.6. The correlation between parameters for SA inversion. 96

Table 4.7. Earth Model from CRUST 2.0..... 99

Table 4.8. Comparison of g_N/g_D for three special cases. 104

Table 4.9. Comparison of Source Parameters..... 106

Table 4.10. The correlation between parameters for SA inversion using CSR RL05 data 108

Table 4.11. Earth Model from CRUST 2.0..... 111

Table 4.12. Comparison of different GRACE products. 111

Table 4.13. Comparison of Source Parameters..... 118

Table 4.4.15. The correlation between parameters for SA inversion. 119

Table 4.15. Earth Model from CRUST 2.0..... 121

Table 4.16. Comparison of different GRACE products. 122

Table 4.17. Comparison of Source Parameters. 127

List of Figures

Figure 2.1. Gravity change, vertical displacement and 'equivalent' vertical displacement on ocean floor. 11

Figure 2.2. Schematic view for equivalent vertical displacement due to horizontal motion. 12

Figure 2.3. Gravity (down component) change at ocean floor from three sources. 14

Figure 2.4. Gravity change at Earth surface. 15

Figure 2.5. Sensitivity to length. 17

Figure 2.7. Sensitivity to width. 20

Figure 2.8. Sensitivity to dip. 21

Figure 2.9. Sensitivity to depth. 22

Figure 2.10. Finite fault model and a double-couple point source model. 25

Figure 2.11. The comparison of directly computed gravity change and displacement with that from the linear relationship. 31

Figure 2.12. The comparison of directly computed gravity change due to both solid Earth deformation and ocean response with that from the linear algorithm. 33

Figure 2.13. Simulated surface displacement on GPS stations and five sea floor sites.... 43

Figure 2.14. Solution uncertainty for the inversion from onshore and offshore GPS/Acoustic displacements. 46

Figure 3.1. Geoid residual degree variance (relative to GOCO02S background model) for each monthly solution from January 2003 to July 2013 for the CSR RL05 NMAX 96 product. 51

Figure 3.2. Time series of GRACE gravity and gravity gradient disturbances. 54

Figure 3.3. Comparison in the spectral domain. 57

Figure 3.4. The absolute value of the north (*left*), east (*middle*), down (*right*) components of the LOS position vector . The plot is for GRACE satellite 1 in March 2011..... 60

Figure 3.5. Comparison of GRACE-observed and model-predicted coseismic and postseismic (March 2011) gravity changes up to degree 70 from CSR RL05 NMAX 96 product. 61

Figure 3.6. Comparison of GRACE-produced and model-predicted gravity gradient change up to degree 70 from CSR RL05 NMAX 96 product..... 62

Figure 4.1. Time series of GRACE gravity and gravity gradient disturbances. 67

Figure 4.2. Comparison of GRACE-observed and model-predicted coseismic and postseismic (March 2011) gravity changes..... 69

Figure 4.3. Comparison of GRACE-produced and model-predicted gravity gradient change. 70

Figure 4.4. Comparison in the spectral domain and along a profile. 71

Figure 4.5. Solution uncertainty for rake angle. 73

Figure 4.6. Comparison of slip distribution models. 75

Figure 4.7. Time series of g_N, *Txz* at 95°E 4.05°N. 85

Figure 4.8. Comparison in the spectral domain. 86
Figure 4.9. Comparison of GRACE-observed and model-predicted coseismic gravity changes up to degree 65 from GFZ RL05a product. 86
Figure 4.10. Comparison of GRACE-produced and model-predicted gravity gradient change up to degree 65 from GFZ RL05a product. 87
Figure 4.11. Comparison in the spectral domain for CSR RL05 NMAX 60 solution results. 88
Figure 4.12. Comparison of GRACE-observed and model-predicted coseismic gravity changes up to degree 60 from CSR RL05 NMAX 60 product. 88
Figure 4.13. Comparison of GRACE-produced and model-predicted gravity gradient change up to degree 60 from CSR RL05 NMAX 60 product. 89
Figure 4.14. Comparison of centroid moment tensor solutions. 94
Figure 4.15. Comparison of centroid moment tensor solutions. 97
Figure 4.16. Time series at 69.4°W 32.45°S. 100
Figure 4.17. Comparison in the spectral domain. 101
Figure 4.18. Comparison of GRACE-observed and model-predicted coseismic gravity changes up to degree 60 from CSR RL05 product. 102
Figure 4.19. Comparison of GRACE-produced and model-predicted gravity gradient change up to degree 60 from CSR RL05 product. 103
Figure 4.21. Time series of g_N, *Txz* at 88.4°E 3.45°N. 113
Figure 4.22. Comparison in the spectral domain. 113

Figure 4.23. Comparison of GRACE-observed and model-predicted coseismic gravity changes up to degree 40. 114

Figure 4.24. Comparison of GRACE-produced and model-predicted gravity gradient change up to degree 40. 115

Figure 4.25. Comparison of centroid moment tensor solutions. 119

Figure 4.26. Time series of g_N, Txz at 100.6°E 7.95°S. 123

Figure 4.27. Comparison in the spectral domain. 123

Figure 4.28. Comparison of GRACE-observed and model-predicted coseismic gravity changes. 124

Figure 4.29. Comparison of GRACE-produced and model-predicted gravity gradient change. 125

Figure 4.30. Comparison of CMT solutions. 128

Figure A.1. The diagram for different geocentric radial distances 144

Chapter 1. Introduction

1.1 Traditional methods to study earthquakes and their limitations.

There were several large undersea earthquakes in the past decade, including the 1 April 2014 Mw 8.2 Iquique, Chile earthquake, the 24 May 2013 Mw 8.3 Okhotsk Sea earthquake, the 11 April 2012 Indian Ocean (Mw 8.6 and Mw 8.2) earthquakes, the 11 March 2011 Mw 9.0 Tohoku earthquake, the 27 February 2010 Mw 8.8 Maule, Chile earthquake, the 12 September 2007 Mw 8.5 Bengkulu earthquake, the 15 November 2006 Mw 8.3 and 13 January 2007 Mw 8.1 Kuril Islands earthquakes, and the 26 December 2004 Mw 9.2 Sumatra-Andaman earthquake. The quantification of these earthquakes, including their exact sizes, location, the geometry and orientation of the faults, is critical for improving our understanding of fault mechanisms, as well as for application in tsunami warning. *Geist et al.* [2007] point out that the centroid location and seismic moment are essential parameters for tsunami forecast and assessment models. It is evident that the magnitude of the moment would directly affect tsunami amplitude. The souse location is also essential in tsunami generation, as shown by the fact that horizontal displacements over the very steep trench zone can generate large tsunamis [*Tanioka and Satake,* 1996; *Meng et al.,* 2012]. Other first-order source parameters such as dip, fault length and width also affect the tsunami wave field [*Geist et al.,* 2007]; for example, vertical dip-slip induces stronger tsunami due to its large vertical deformation [*Tanioka and Satake,* 1996]. Traditional measurements for studying focal mechanisms include

seismological data, GPS data, Interferometric Synthetic Aperture Radar (InSAR) data, tsunami data, vertical displacements on coral reefs, and recently repeated airborne LiDAR data, and so on. However, there are limitations for those traditional methods on estimating the source parameters of large undersea earthquakes.

Seismological methods have difficulty in estimating source parameters such as seismic moment for rupture with long duration due to the overlap of interfering arrivals [*Lay et al.*, 2005; *Bilek et al.*, 2007; *Chlieh et* al., 2007]. Seismic waves data are also inadequate for detecting slow or aseismic slip and postseismic slip [*Chlieh et* al., 2007; *Han et al.,* 2013], for example the 2004 Sumatra-Andaman earthquake had a long duration, slow rupture [*Banerjee et al.,* 2005; *Lay et al.,* 2005; *Park et al.,* 2005; *Seno and Hirata*, 2007] and large magnitude of aseismic afterslip [*Chlieh et* al., 2007]. *Lay et al.* [2010] indicate that seismic inversions are sensitive to waveform types and the frequency band, which is shown by the fact that different slip models are obtained from seismic waves with different frequency bands for the 2010 Maule, Chile earthquake. In addition, since seismic inversions are highly dependent on the velocity structure [*Ji et al.*, 2002], they have instabilities for shallow ruptures [*Lay et al.*, 2011].

Although geodetic measurements, such as GPS data, have the potential to overcome the inadequacy of seismological data in detecting slow/aseismic slip, they are limited by the spatial distribution of their ground-based sites. Particularly, for undersea megathrust earthquakes, GPS stations are usually located at one side of the fault area, thus providing limited constraints on the source parameters [*Chlieh et al.,* 2007; *Lay et al.*, 2011; *Wei et al.*, 2012]. For example, *Chlieh et al.* [2007] showed that the resolution for shallower patches on the finite fault near the trench are poorer than the resolution for deeper patches

due to the sparse distribution of the measurements on the islands farther away from the trench. *Wei et al.* [2012] also show that the inland static GPS data are quite insensitive to the shallow rupture and the resolution of the inverted slip model decreases rapidly away from the coast.

1.2 GRACE data on constraining focal mechanisms

The twin-satellite Gravity Recovery And Climate Experiment (GRACE) mission [*Tapley et al.,* 2004] has been producing temporal global gravity field observations with monthly sampling rate and a spatial resolution longer than ~330 km (half-wavelength). The GRACE data have revolutionized our understanding of Earth's mass redistribution, including the terrestrial hydrologic water balance, ocean mass variations and sea level rise, ice-sheet and glacier ablation, and their possible links with anthropogenic climate change. As one of such mass redistribution processes, earthquakes trigger crustal/mantle dilation or compression and surface uplift or subsidence, causing permanent change in the Earth's gravity field. By surveying right above the rupture region over the ocean, although with a coarse spatial and temporal resolution, GRACE data have been demonstrated to have the feasibility to complement other data for detecting and constraining focal mechanisms of large undersea earthquakes. GRACE data have a better spatial coverage as compared to GPS data, and have better capability to detect aseismic slip as compared to seismic data. Several large earthquakes have been detected by GRACE data and analyzed in contemporary studies, including the 2004 Sumatra-Andaman earthquake [e.g., *Han et al.*, 2006; *Wang et al.*, 2012c; *Panet et al.*, 2010], 2010 Maule, Chile earthquake [e.g., *Han et al.*, 2010, *Heki & Matsuto*, 2010, *Wang et al.*, 2012a], and the 2011 Tohoku earthquake [e.g., *Matsuo & Heki*, 2011; *Cambiotti and*

Sabadini, 2012; *Han et al.*, 2011, 2013; *Wang et al.*, 2012b; *Dai et al.,* 2014; *Li and Shen*, 2015].

These coseismic deformation studies for large undersea earthquakes were demonstrated by using the inferred gravity gradient changes computed from GRACE temporal gravity field solutions, which resulted in spatial resolution enhancement and improved constraints for the 2004 Sumatra-Andaman earthquake [*Wang et al.*, 2012c]. The direct gravity gradient change measured by Gravity field and steady-state Ocean Circulation Explorer (GOCE) gravity gradiometry were also shown to be able to detect the coseismic deformation [*Fuchs et al.*, 2013]. Other studies that improve the GRACE data processing include spatial enhancement of the gravity change using Slepian basis functions [*Simons et al.*, 2006] for the 2010 Maule, Chile earthquake [e.g., *Wang et al.*, 2012a], and the direct processing of the inter-satellite K-band range (KBR) data [*Han et al.*, 2011]. *Wang et al.* [2012a, 2012b] for the first time utilized Slepian functions to analyze GRACE observed coseismic signals. Similar techniques were applied to the GRACE observed 2011 Tohoku earthquake seismic signals and source parameter inversion by *Cambiotti and Sabadini* [2012]. *Wang et al.* [2012c] first demonstrated that the correlated errors in the GRACE temporal gravity field solution can be substantially suppressed using the *Txx* and *Txz* (*x*, *z* refers to north and up directions, respectively) components of gravity gradient change. *Li and Shen* [2011] also conducted a study on the 2004 Sumatra-Andaman earthquake and addressed the suppression to the correlated errors using the *Txz* component only.

The inversion for several source parameters, such as the seismic moment, dip angle and rake angle, based on normal mode formulation [*Dahlen and Tromp,* 1998] assuming

point-source dislocation are demonstrated for the 2011 Tohoku earthquake [*Han et al.*, 2011]. *Wang et al.* [2012a, 2012b] adopted the simulated annealing algorithm to invert for fault length, width and uniform slip of the 2010 Chilean Maule and the 2011 Tohoku earthquakes, based on a finite fault model. *Cambiotti & Sabadini* [2013] presented the estimation of all parameters (centroid location and moment tensor) for a point source using GRACE data. *Han et al.* [2013] further solved for the seismic moment tensors of multiple centroids but with the location fixed based on the normal mode formulation for a number of large earthquakes over the last decade using GRACE data.

1.3 Outline

In this dissertation, a new approach for GRACE data processing using only the *north* component of the observed gravity change and the corresponding gravity gradient change is described and applied to five recent large undersea earthquakes. As a result, no decorrelation or spatial filtering of the GRACE data is needed, leading to the improved spatial resolution. The resulting gravity and gravity gradient change data are then used in the inversion for the source parameters based on two different source models, i.e., the seismic moment, fault width, rake angle, and the centroid location for a finite fault model, and the seismic moment, dip, strike, rake angle, and the centroid location and depth for a point-source model.

Chapter 2 describes the forward modeling of the gravity and gravity gradient change from the slip distribution model. Then I conduct the sensitivity analysis of gravity and gravity gradient change to different finite fault parameters. Another forward modeling based on point-source moment tensor is also presented. This simple point-source model is considered mainly because of the linear relationship between the coseismic gravity and

gravity gradient change and the double-couple moment tensor elements, as well as the lower sensitivity of GRACE data to finite fault length. Based on the linear algorithm, I perform the least-squares estimation of double-couple moment tensor from GRACE-derived gravity and gravity gradient change, from GPS surface displacement, and from the combination of GRACE data and GPS data. Then I evaluate the accuracy and precision of inverted source parameters based on the linear algorithm from simulated GRACE data and GPS data. The comparison of the inversion from simulated GPS data and GRACE data and their combination is analyzed to demonstrate the distinctive constraint from different data sets, and to show the contribution of GRACE data on offshore seismic deformation. Chapter 3 presents the improved GRACE data processing methods developed in this study, which includes the Heaviside step function, the localized spectral analysis, and the approach of using the north component of gravity and gravity gradient change. In Chapter 4, I present the inversion of the finite fault model for the 2011 Tohoku earthquake using the simulated annealing algorithm. Finally, the inversion of point source parameters for five recent large undersea earthquakes are carried out using the least-squares adjustment method combined with the simulated annealing algorithm. Chapter 5 presents the discussion and conclusions of this study.

Chapter 2. Forward Modeling and Source Parameters Inversion Method

2.1 Forward modeling based on finite fault model

2.1.1 Gravity and gravity gradient change predicted from slip distribution model

Here we outline our approach for the model prediction of gravity and gravity gradient change based on dislocation theory in a layered half-space [*Wang et al.*, 2006]. First, the coseismic gravity and surface displacement changes responding to the solid Earth deformation are evaluated at the ocean floor using Wang's PSGRN/PSCMP software [*Wang et al.*, 2006, Courtesy, *R. Wang*]. Second, we evaluate the effect of the ocean response [*de Linage et al.*, 2009; *Cambiotti et al.*, 2011] and the effect of topography [*Li & Chen*, 2013] on the surface density change, therefore its effect on the gravity change. For example, the surface density may decrease corresponding to the flowing out of the ocean water due to an uplift crustal motion, and the effect of topography is evaluated by considering the equivalent vertical displacement due to the horizontal motion over a sloped topography. Next, the gravity change due to solid earth deformation and surface density change at ocean floor is transformed to geopotential spherical harmonic coefficients up to degree 899. Then, each component of gravity and gravity gradient change is computed at a regular grid on Earth's mean semi-major axis (6378.1363 km) from the geopotential coefficients up to the maximum degree (say 60) commensurable with the respective GRACE data products. The reason why to expand the gravity change

on a dense grid up to a high spherical harmonic degree (899) and then truncate the expansion at a low degree (60) is that in this way the low degree part of the coseismic signal can be reliably retrieved, and the aliasing error caused by sparse sampling may be reduced. Given the spherical harmonic coefficients of the disturbing gravitational potential, three components of gravity disturbance, g_N, g_E, g_D, which are the first derivatives of the disturbing gravitational potential, T, in the local north-east-down frame, can be expressed using equations (B.11)~(B.13). The gravity gradient disturbance, *Txx*, *Txy*, *Txz*, *Tyy*, *Tyz*, *Tzz* (*x, y, z* axis points to north, west, up direction, respectively), as the second derivatives of T, can be expressed using equations (B.14)~(B.19).

Taking the 2011 Tohoku earthquake as an example, the coseismic slip distribution model created by [*Wei et al.*, 2012] using teleseismic body waves and near source GPS observations, and the postseismic slip distribution model produced by *Ozawa et al.* [2011] using GPS measured displacements during 12–25 March 2011, are adopted to predict the gravity field change resulting from the 2011 Tohoku earthquake. The coseismic fault plane boundary is shown as the black rectangle in Figure 2.1, with the strike angle of 201° and the dip angle of 9°; the maximum slip is 48 m, at the depth of 10.58 km with the rake angle of 90°, indicating the oceanic plate subducting beneath the continental crust (http://www.tectonics.caltech.edu/slip_history/2011_taiheiyo-oki), as shown in Figure 2.2. The postseismic slip model suggests that the afterslip, overlapping the coseismic area and peripheral to it, extends along the dipping direction. Resembling the coseismic slip, the afterslip, with the seismic moment of about 10% of the main shock, has the mean rake angle of 90°, average strike angle at 193°, average dip angle of about 18°, and the maximum slip is up to 1 meter at the depth of 38 km.

The predicted gravity and gravity gradient change, corresponding to the coseismic and postseismic slip distribution model [*Wei et al.*, 2012; *Ozawa et al*., 2011], are calculated using our developed code for each step of the model prediction procedure built on the PSGRN/PSCMP software [*Wang et al.*, 2006], based on the 1D velocity model from Shengji Wei [*personal communication*, 2013] that is extracted from a 3D model [*Takahashi et al.*, 2004], with the top replaced by an ocean layer. The ocean depth (3.94 km) is the average value from the bathymetry data in CRUST2.0 model over the fault region. Since the provided fault segments' depth is relative to the average elevation of GPS stations being used [*Ji et al.*, 2002], these fault patches' depths are then adjusted to be relative to the ocean floor (equation A.1). The down component of gravity (Figure 2.1 left) and vertical displacement change (Figure 2.1 middle) corresponding to the solid Earth deformation are evaluated at the ocean floor using the PSGRN/PSCMP software, with significant uplift up to 12 m near the trench and with slightly subsidence for about 1 m near the coast. Consistent with the sea floor vertical movement, the gravity increases to about 1000 μGal near the trench and decreases to about 300 μGal near the coast.

As the fault dislocation is under sea, the passive response of the ocean water is considered. Near trench where crust goes up, water is evacuated; while near coastline where crust subsides, water flows in. As compared to coseismic crustal vertical displacement, the geoid change or the average sea level change is negligible, only up to several centimeters. So the thickness of the water layer has changed $-H$, where H is the ocean floor vertical displacement (positive upwards) as shown in Figure 2.1 (*middle*). We assume that the water layer is condensed on a zero thick shell at the ocean floor, both

before and after the earthquake. Hence, the effect of oceanic response on gravity is like adding a shell of surface density at the ocean floor:

$$\sigma = -H \times \rho_w \times OF \tag{2.1}$$

where ρ_w is the ocean water density and *OF* is the ocean function (1 over ocean, 0 over land). *Broerse et al.* [2014] discussed the large influence of the ocean function on modeled coseismic gravity changes compared to the uniform ocean assumption, which assumes the Earth is globally covered by ocean. They showed that it is essential to distinguish the marine and terrestrial area, especially for the 2010 Maule, Chile earthquake, which has crustal subsidence over land and uplift over ocean area.

The topography/bathymetry effects on coseismic surface displacement are usually neglected; here we evaluate its effect on gravity. The effect of topography on gravity is estimated by considering the 'equivalent' vertical displacement [*Li and Chen*, 2013] due to the horizontal displacement over the sloped oceanic trench. For the ocean trench at the fault region, the depth of water goes deeper to the southeast direction according to the bathymetry data from ETOPO1 [*Amante and Eakins*, 2009]. Seismic model predicted horizontal displacement at ocean floor is at the southeast direction, which would cause an equivalent uplift (Figure 2.1 *right*), thus mass increase at the ocean trench. Surface density change would be $\sigma = \bar{h} \times \rho_s - \bar{h} \times \rho_w \times OF$, where ρ_s is the density of sediments, $\bar{h}$ is the equivalent vertical displacement, which can be estimated from horizontal displacements and topography (ETOPO1).

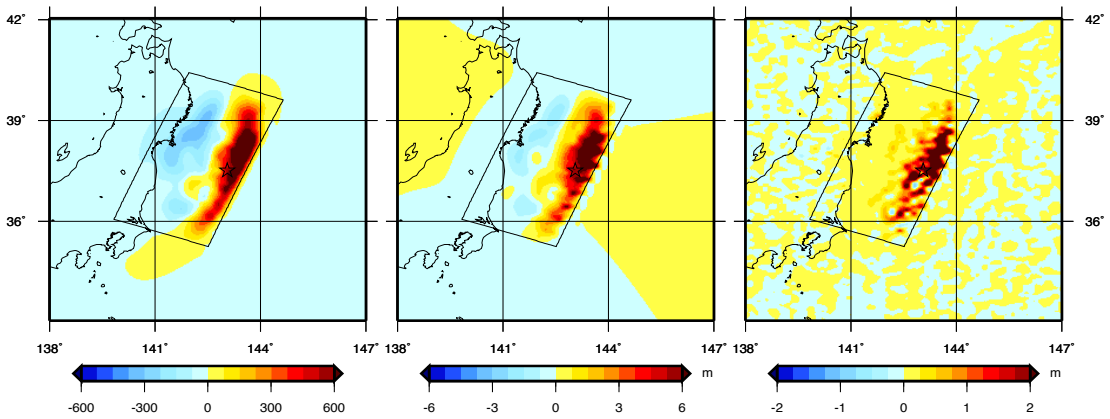

Figure 2.1. Gravity change, vertical displacement and 'equivalent' vertical displacement on ocean floor.
The coseismic and postseismic slip distribution model [*Wei et al*., 2012; *Ozawa et al*., 2011] is adopted. *Left*: Gravity change (μGalμGal) (without free air correction) corresponding to solid Earth change; *Middle*: Vertical displacement, H (meter) with upward as positive direction; *Right*: 'Equivalent' vertical displacement caused by topography with horizontal displacement. Black Rectangle is the boundary of the fault plane.

As shown in Figure 2.2, the equivalent vertical displacement is, $\bar{h} = H(\theta', \lambda') - H(\theta, \lambda)$, where H is the topography as a function of longitude λ, and colatitude θ. (θ', λ') is the coordinate of the point that shifts to the location (θ, λ) due to the earthquake. (θ', λ') is calculated based on the equations $\theta - \theta' = u_N / a$, $\lambda - \lambda' = u_E / (a \sin\theta)$, where a is the Earth's mean radius, and (u_N, u_E) is the horizontal displacement along North, East direction for location (θ', λ'). Under the assumption that horizontal displacement is the same over a small area (e.g. area with the radius of 60 meter, the maximum amount of slip during an earthquake), (u_N, u_E) is practically calculated at location (θ, λ) from the slip distribution model.

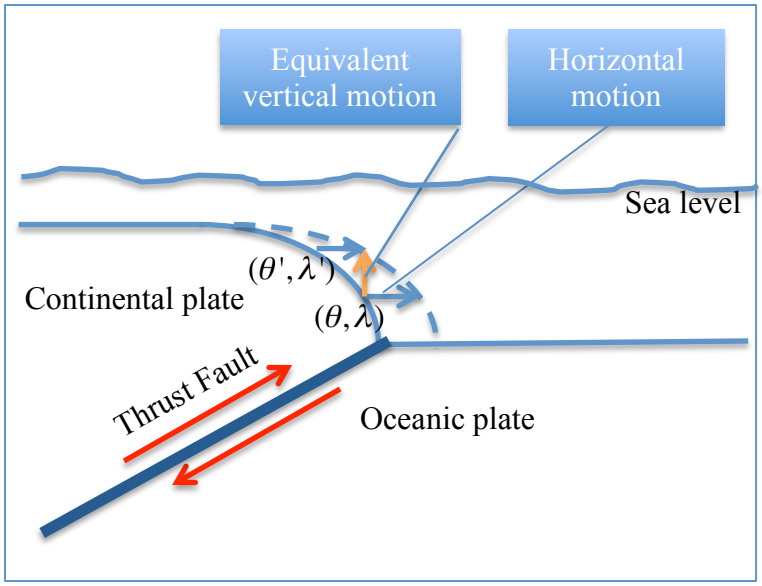

Figure 2.2. Schematic view for equivalent vertical displacement due to horizontal motion. The solid line is the ocean bottom before earthquake, and the dash line is the trench after earthquake due to the horizontal displacement. Orange arrow shows the equivalent vertical displacement due to the horizontal displacement (blue arrow) over the sloped trench. Red arrows show the direction of slip on the fault plane for the 2011 Tohoku earthquake.

Surface density change can be expanded as:

$$\sigma(a_1,\theta,\lambda) = \sum_{n=0}^{\infty}\sum_{m=0}^{n}\left(\Delta\tilde{C}_{nm}\cos m\lambda + \Delta\tilde{S}_{nm}\sin m\lambda\right)\overline{P}_{nm}(\cos\theta) \tag{2.2}$$

$\Delta\tilde{C}_{nm}$ and $\Delta\tilde{S}_{nm}$ are the spherical harmonic expansion coefficients for the surface density change, with the unit as kg/m^2. a_1 is the geocentric radial distance of ocean floor over the fault area (equation A.2), which is computed by subtracting the ocean thickness from the local geoid's geocentric distance (6,370 km, for the fault area of 2011 Tohoku earthquake).

Geopotential change corresponding to the surface density change can be expressed as:

$$T = \frac{GM}{R}\left(\sum_{n=0}^{\infty}\sum_{m=0}^{n}\left(\frac{R}{r}\right)^{n+1}\left(\Delta\overline{C}_{nm}\cos m\lambda + \Delta\overline{S}_{nm}\sin m\lambda\right)\overline{P}_{nm}(\cos\theta)\right) \tag{2.3}$$

where *GM* is the gravitational constant multiplied by the mass of the Earth, m^3/s^2, *R* is the Earth's mean semi-major axis (6378136.3 m), $\Delta\overline{C}_{nm}$ and $\Delta\overline{S}_{nm}$ are the normalized spherical harmonic coefficient differences, $\overline{P}_{nm}$ is the fully normalized associated Legendre function, r is the radius (m), θ is the colatitude (^{0}), and λ is the longitude (^{0}). Refers to [*Wahr et al.*, 1998], we have:

$$\begin{bmatrix} \Delta\overline{C}_{nm} \\ \Delta\overline{S}_{nm} \end{bmatrix} = \left(\frac{a_1}{R}\right)^n \left(\frac{a_1}{a}\right)^2 \frac{3(1+k_n)}{a\rho_{ave}(2n+1)} \begin{bmatrix} \Delta\tilde{C}_{nm} \\ \Delta\tilde{S}_{nm} \end{bmatrix} \tag{2.4}$$

where a is the Earth's mean radius, 6371 km, ρ_{ave} is the average Earth density, kg/m^3, and k_n is the load Love number.

From the changes of geopotential coefficients, the corresponding gravity change due to the passive response of the ocean layer is evaluated as shown in Figure 2.3 (*middle*), and the topography effect is shown in Figure 2.3 (*right*). We can see that the gravity change due to the ocean water redistribution cancels out part of the gravity change due to the solid Earth deformation (Figure 2.3 *left*), e.g., the negative gravity change due to water flowing out near trench is about 40% of the solid Earth gravity increase. This ratio is slightly smaller than the ratio of ocean density over density of sediment (51%), since the solid Earth gravity change is also contributed by the internal density dilation in addition to the vertical displacement at sea floor. The topography effect is up to 16% of the solid earth gravity change. From Figure 2.1 (*right*), we can see that the equivalent uplift corresponding to the horizontal displacement over the trench is positive, which indicates an increase of mass. To fulfill the mass balance principle, the crustal dilation over the coastal/left side of the oceanic trench needs to be further considered, which will reduce the magnitude of the equivalent mass increase [*Li et al.*, 2015, to be submitted, personal

communication]. Thus we choose to neglect this topography correction in this study.

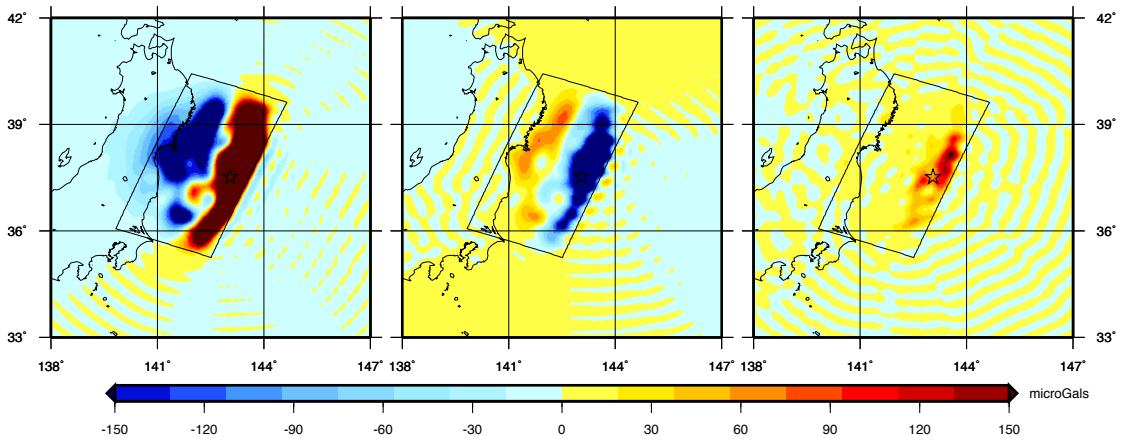

Figure 2.3. Gravity (down component) change at ocean floor from three sources. *Left*: g_D due to solid Earth deformation; *middle*: g_D from passive ocean response; *right*: g_D due to the approximate topographic correction. The black rectangle is the coseismic fault plane boundary, and the black star is the estimated Global Centroid Moment Tensor Project (GCMT) epicenter (143.05°E, 37.52°N).

Next, each component of gravity and gravity gradient change is computed at a regular grid on Earth's mean semi-major axis (6378.1363 km) instead of on the ocean floor. The difference of the gravity change evaluated on the ocean floor and on Earth's semi-major axis can be significant, but it has not been discussed in many previous publications [*Han et al.*, 2006; *Matsuo & Heki*, 2011; *Cambiotti and Sabadini*, 2012; *Wang et al.*, 2012b]. For this 2011 Tohoku earthquake, this upward continuation of gravity from the ocean floor (with radius as 6366.0567 km, g_D up to 633 μGal) to Earth's semi-major axis (6378.1363 km, g_D up to 380 μGal, Figure 2.4 *right*) causes the magnitude to drop for about 40% for the gravity up to degree 899, and causes the magnitude to drop for about 9% for the gravity up to degree 60. Accurate estimation of the modeled gravity change

directly affects the seismic moment inverted from GRACE-observed gravity change. If ignore this upward continuation, the inverted seismic moment will be underestimated.

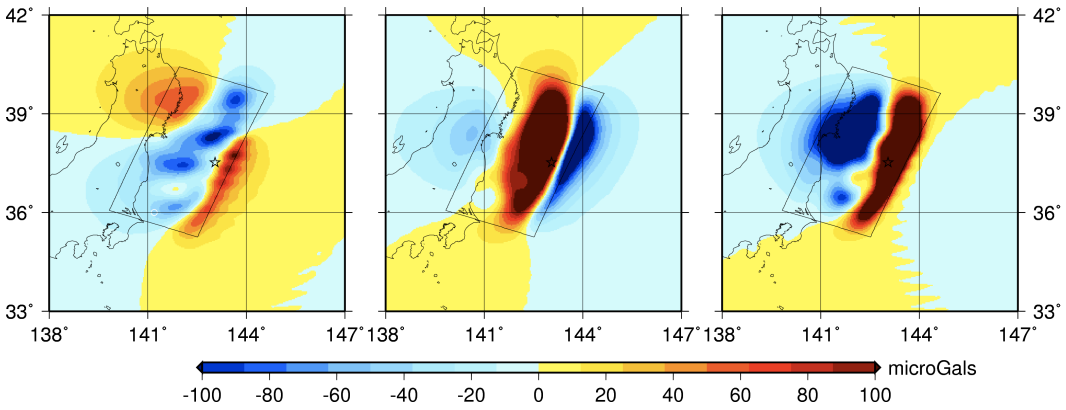

Figure 2.4. Gravity change at Earth surface.
North (*left*), east (*middle*), down (*right*) components of gravity change for both solid Earth deformation and passive oceanic response. Gravity change is computed from spherical harmonic coefficients up to degree 899, at the Earth's surface with R as 6378136.3 m. These high-degree geopotential spherical harmonic coefficients are transformed from the gravity change due to solid Earth deformation and the surface density change due to ocean response at ocean floor on dense grids (0.2° along longitude by 0.1° along latitude).

Then, we compute each component of gravity and gravity gradient change from the spherical harmonic coefficients up to the maximum degree (say degree 60) that's consistent with GRACE data products. The high-resolution gravity change (Figure 2.4), when truncated to degree 60 (Figures 4.2 *d~f*), decreases for about one order of magnitude, with its spatial pattern dilating outward. The troughs and peaks for g_N, g_E, g_D all shift outwards along the east west direction. For instance, for g_D (Figure 2.4 right), the model-predicted maximum is 379.6 μGal, at 143.6°E, 38.25°N; the minimum is –201 μGal, at 142.2°E, 38.65°N. After truncation at degree 60 (Figure 4.2f), there is a maximum at 144.8°E, 37.2°N, 19.53 μGal, and a minimum at 139.6°E, 38.8°N, –30.8 μGal. The g_D change amplitude decreases by one order of magnitude, and the peak and

trough locations dilate outward in the west-east direction, with the trough moving to the west for 2.6°and peak shifting to the east for 1.2°. In addition, the yellow-cyan (positive-negative) ripple effect occurs distinctly (Figure 4.2f), with larger magnitude for the signal closer to the main negative-positive signal.

2.1.2 Sensitivity analysis of gravity and gravity gradient change to different finite fault models

To demonstrate the sensitivity of GRACE-observed north components of gravity and gravity gradient change to various fault parameters for an earthquake, e.g. fault strike, dip angle, rake angle, depth, length, width, dislocation magnitude, we carry out several synthetic scenarios estimating g_N, *Txx*, *Txy*, *Txz*, based on the modeling procedure described above. Here we choose to study the 2011 Tohoku-Oki earthquake for the sensitivity study. For the Tohoku-Oki earthquake's fault parameters in the study, we choose strike angle to be 200°, fault length to be 600 km, fault width to be 300 km, dip angle to be 9°, depth to be 5 km, slip magnitude to be 2 m, rake angle to be 90°. To reveal the north components of gravity and gravity gradient change's sensitivity to a specific fault parameter, all other fault parameters are fixed to the chosen value, with only the looked-for parameter as a variable.

To test the sensitivity of GRACE observation (north components of gravity and gravity gradient change) to the fault length, the value of 300 km, 600 km, or 900 km is taken for the fault length, with all other parameters fixed. As shown in Figure 2.5, the spatial magnitude increases and signal pattern of g_N is elongated along the strike direction when the fault length increases; the spatial pattern of *Txx*, *Txy*, *Txz* has the same characteristic

(figures not shown). Thus, the broadness of the signal along the strike direction will provide constraint on the fault length. However, the solution uncertainty (defined as in Figure 2.14 or Figure 4.5) of length during the inversion in section 4.1.2 is relatively large, around 150 km for GFZ RL05 data and 110 km for CSR RL05 data, respectively, which implies that the sensitivity of graivty to fault length is relatively low. Hence, during the inversion using CSR RL05 data in Section 4.1.2, for the first iteration, we fixed the length parameter at 240 km based on GPS/seismic slip models, and solved for location, width, slip, rake parameters simontaneously. After obtaining location and rake angle, the fault length, width and slip are simultaneously estimated during the second iteration.

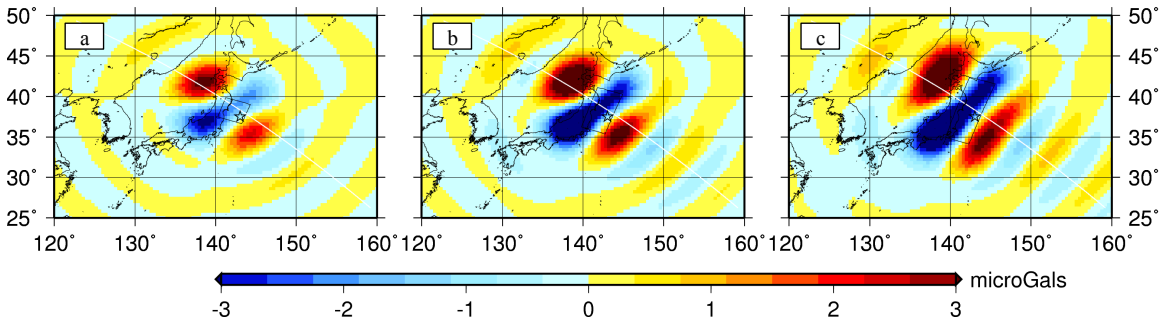

Figure 2.5. Sensitivity to length.
Model derived g_N change for the fault length: 300 km (a), 600 km (b), 900 km (c). Fault parameters are: strike angle 200°, fault width 300 km, dip angle 9°, depth 5 km, slip magnitude 2 m, rake angle 90°. The black rectangle is the fault plane boundary, and the black star is the Tohoku-Oki earthquake epicenter. White line is a chosen profile (through the center of the top edge of the fault plane, 70° to the strike direction) across main peaks.

Figure 2.6 shows the sensitivity of gravity gradient change to the strike angle and rake angle, which determines the direction of slip vector. As the strike angle increase

clockwise from 210° to 270°, the spatial pattern of the GRACE-observed *Txx* rotates clockwise for about 30°, the similar characteristic for g_N, *Txy*, *Txz*. When the dislocation rake angle increases in an anticlockwise direction, from 30°, to 60°, 90° (Figure 2.6 (d, e, f)), the spatial pattern of *Txz* rotates anticlockwise for about 35°. More elaborate simulation for strike angle (animation link: goo.gl/QPJggv) and rake angle (goo.gl/WSIafi) shows that the spatial pattern varies from 'stripes' to 'flowers' when strike or rake angle varies, which in addition help to constrain the slip direction. Since the orientation of the spatial pattern is both affected by rake angle and strike angle, it might be difficult to isolate these two parameters during an inversion. Because strike angle is well constrained by other data sets, e.g. the after shock area, plate boundary direction, we may choose to fix the strike angle and only solve for rake angle.

For each width value of 100 km, 200 km, 300 km, north components of gravity and gravity gradient changes (Figure 2.7) are computed along the chosen profile (white line in Figure 2.5) that crosses the signal peaks. First of all, it is clear that g_N, *Txx*, *Txy*, *Txz* signal magnitude increases since the seismic moment increases, with the sensitivity of around 160% (equation 2.5). The sensitivity of $f(x,y)$ with respect to the independent variable x is defined as,

$$sensitivity(f) = \frac{1}{2}\left(\frac{\max(f(x_1,y)) - \max(f(x_0,y))}{\max(f(x_1,y)) + \max(f(x_0,y))}\frac{x_1 + x_0}{x_1 - x_0} + \frac{\max(f(x_2,y)) - \max(f(x_1,y))}{\max(f(x_2,y)) + \max(f(x_1,y))}\frac{x_2 + x_1}{x_2 - x_1}\right) \quad (2.5)$$

where x, y are two independent variables, x_0, x_1, x_2 are the three given values, e.g. they are 100 km, 200 km, 300 km respectively, for fault width. This formula gives how much the peak value of *f*(*x,y*) changes with respect to the change of independent variable *x*. For example, the first part in the parenthesis is basically the change of the peak value of *f*(*x,y*) divided by the change of *x* from x_0 to x_1, but this ratio is further scaled by the mean of the

peak value of $f(x_0,y)$ and $f(x_1,y)$ divided by the mean of x_0 and x_1. The second part in the parenthesis is the same as the first part but for the case of independent variable x changing from x_1 to x_2. In addition to the signal magnitude, the local peaks of g_N, *Txx*, *Txy*, *Txz* move northwest to about 40 km when the fault width increases from 100 km to 300 km. Thus the magnitude of the gravity and gravity gradient signal and the location of the peak value provide constraint on the fault width.

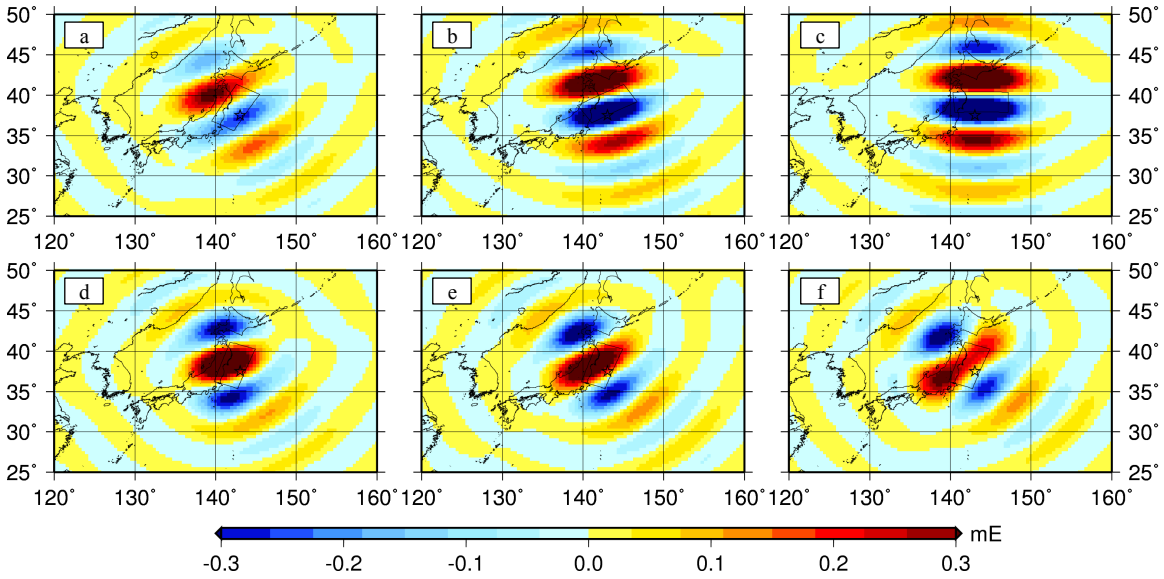

Figure 2.6. Sensitivity to strike and rake.
Model derived *Txx* change for the fault strike angle of 210° (a), 240° (b), 270° (c), and model derived *Txz* change for the slip rake angle of 30° (d), 60° (e), 90° (f). Fixed fault parameters are: fault length 600 km, fault width 300 km, dip angle 9°, depth 5 km, slip magnitude 2 m. Rake angle is 90° for the strike angle case, and strike angle is 200° for the rake angle case. Other labeling is the same as in Figure 2.5.

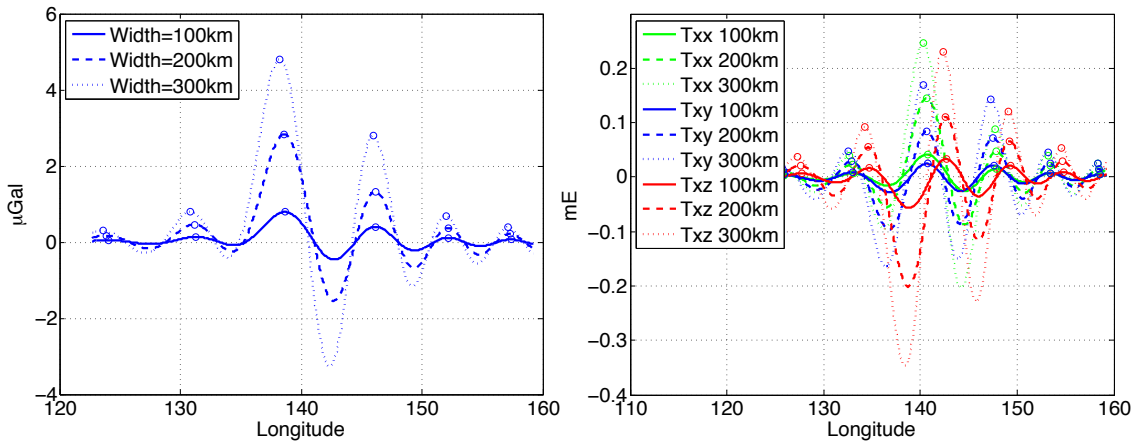

Figure 2.7. Sensitivity to width.
Coseismic g_N change (left) and gravity gradient change (right) along the profile shown in Figure 2.5 for width of 100 km, 200 km, or 300 km, respectively. Center of the fault plane is fixed. Fault strike angle, length, dip angle, depth, slip, rake angle, are fixed at 200°, 600 km, 9°, 5 km, 2 m, 90°, respectively. Circles are the local maxima.

When dip angle takes on the value of 3°, 9°, 15°, the magnitude increases since more mass around two sides of the fault plane is deformed, with the sensitivity of 54%, 51%, 76%, 76% for g_N, *Txx*, *Txy*, *Txz*, respectively. As shown in Figure 2.8, the signal shifts to the northwest for about 55 km when the dip angle increases. Since the signal magnitude increase and signal shift to the west for either an increase dip angle or increase width, it might be difficult to separate those two parameters. Nevertheless, north components of gravity and gravity gradient signals are more sensitive to the width change, it is suggested to fix the dip angle for a finite fault model inversion.

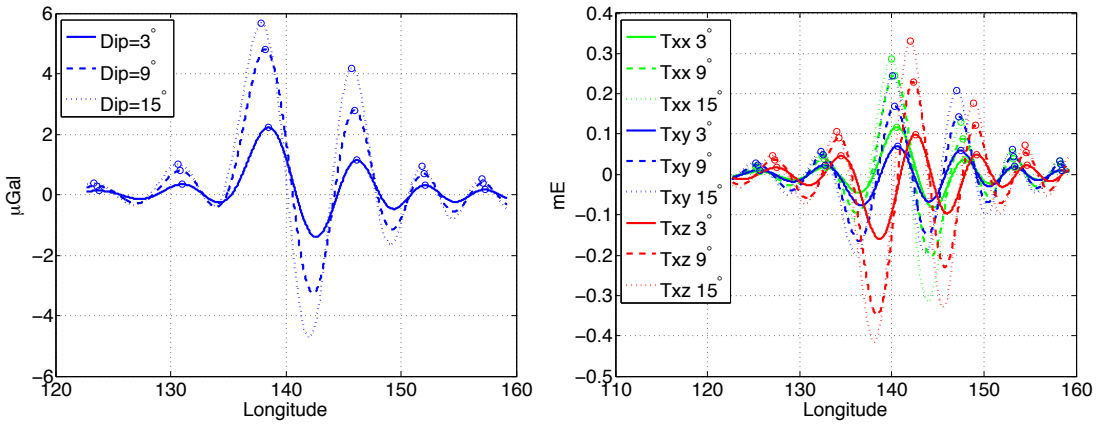

Figure 2.8. Sensitivity to dip.
Coseismic g_N change (left) and gravity gradient change (right) along the profile in Figure 2.5 for dip angle of 3°, 9°, and 15°, respectively. Fault strike angle, length, width, depth, slip, rake angle, are fixed at 200°, 600 km, 300 km, 5 km, 2 m, 90°, respectively. Center of the fault plane is fixed.

To test the GRACE-observed coseismic north components of gravity and gravity gradient change's sensitivity to the depth parameter, with all other parameters fixed, the depth of the top edge of the fault takes the value of 5 km, 30 km, 50 km. When the fault depth increases, on one hand, the gravity change may decrease since the deformed medium gets further away from the ground surface; on the other hand, gravity change may increase since an additional volume of internal medium being elastically deformed. Figure 2.9 shows the overall magnitude of gravity and gravity gradient change increases, with the expected low sensitivity of only about 35%. It is also shown in Figure 2.9 that g_N, *Txx*, *Txy*, *Txz*, shift around 25 km southeast. Considering the signal magnitude is also determined by the dislocation magnitude, there would be a tradeoff among fault depth, dip angle and fault width in determining the location of the peaks. Since the gravity and gravity gradient are least sensitive to the fault depth, it's also suggested to fix the depth angle for a finite fault model inversion.

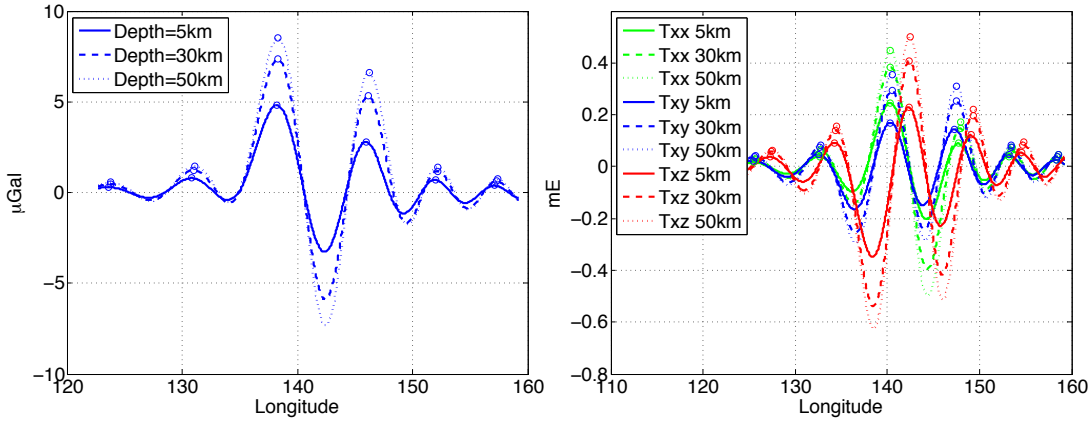

Figure 2.9. Sensitivity to depth.
Coseismic g_N change (*left*) and gravity gradient change (*right*) along the profile in Figure 2.5 for depth of 5 km, 30 km, 50 km. Fault strike angle, length, width, dip angle, slip, rake angle, are fixed at 200°, 600 km, 300 km, 9°, 2 m, 90°, respectively.

The north components of gravity and gravity gradient change magnitude increase with the sensitivity of 100% when the uniform fault slip magnitude increase from 2 m, to 5 m, 8 m. This result is consistent with that the gravity and gravity gradient is linear to the uniform slip magnitude for shear dislocation [*Sun and Okubo*, 1993; *Okada* 1992], with peaks location staying exactly the same (results not shown here). The GRACE-observed gravity and gravity gradient signal magnitude will provide direct constraint on the fault plane dislocation magnitude, in the form of a linear relationship.

The spatial pattern orientation of north components of gravity and gravity gradient are sensitive to strike angle and rake angle. If given the strike angle by other observations, the rake angle can be constrained by GRACE observations. Signal magnitude will provide linear constraint on the fault dislocation magnitude. Since the location of the signal peaks are determined by the fault width, dip angle, and fault depth, it's hard to separate these three parameters. As the GRACE-observed signal is least sensitive to fault

depth and most sensitive to fault width, it is suggested to resolve the fault width during the finite fault model inversion while fixing the fault dip angle and depth. In conclusion, the GRACE-observed north components of gravity and gravity gradient for the 2011 Tohoku-Oki earthquake, can provide excellent constraints on the fault rake angle, fault width, dislocation magnitude, however, they are relatively less sensitive to fault length.

2.2 Forward modeling based on double-couple point source

Instead of utilizing a finite fault model as in section 2.1, this section uses a point source to denote the source model for the forward modeling of GRACE-derived gravity and gravity gradient change resulting from a seismic deformation. The main reason to consider a point source is that a linear algorithm can then be established between the coseismic gravity and gravity gradient change and the double-couple moment tensor elements. Another rationale to consider the point source model is the less sensitivity of GRACE data to the fault extension [*Cambiotti & Sabadini*, 2013], especially to the fault length, as shown in the sensitivity analysis.

2.2.1 Double-couple point source

A shear fault model can be expressed using the strike, ϕ_s, dip, δ, rake angle, λ, and the seismic moment, M_0. The strike angle (Figure 2.10a) is the azimuth (with respect to North) of the projection of fault plane on the Earth's surface, which is measured clockwise from north with the fault dipping down to the right of the strike direction [*Aki and Richards*, 1980, pp. 106], ranging from 0 to 2π. The dip angle is the angle between fault plane and horizon, characterizing the steepness of the fault, ranging from 0 to $\pi/2$. And the rake angle is the angle between the strike direction and slip direction, ranging from $-\pi$ to π. The seismic moment was originally defined for the point force models, and

it is force F times distance d for a point force couple (Figure 2.10c), where a point force is a force applied to a point in an elastic medium. This is where the term 'moment' comes from. For a shear fault, the seismic moment equals to μAS, where μ is the rigidity of the elastic medium in *Pa*, A is the area of the fault, and S is the amount of fault slip.

The earthquake source with only shear motion on a fault plane can be modeled by a double-couple point source. For example, a vertical strike slip fault (Figure 2.10b) can be represented using the double-couple point source model as in Figure 2.10c. According to the representation theorem [*Aki and Richards*, 1980, pp. 38-50], for seismic wavelengths much larger than the size of the fault, the finite fault model (e.g. Figure 2.10b) with slip S over the fault of area A in an elastic medium of rigidity μ gives the same seismic radiation as the 'double-couple' point forces with moment of μAS. As shown in Figure 2.10c, a double-couple point forces model consists of two pairs or a "double-couple" of point forces. A double couple of point forces have two opposing torques (moment of force) with equal moment, leading to zero translation or rotation effect but resulting in the deformation of the medium. Since the source is approximated as a point in space, the concept of a 'double-couple point source' is introduced.

The seismic moment tensor is used to characterize the information about the source [*Aki and Richards*, 1980, pp. 50-57]. Generally, the direction of the slip and orientation of the fault plane are not known *a priori*. So, for a generally oriented dislocation or slip on an arbitrary fault plane, nine possible couples of forces are required to obtain equivalent forces for the dislocation. Three directions of forces and three possible lever arm directions generate these nine couples, leading to the concept of moment tensor. The moment tensor for a double-couple point source can be denoted as:

$$\boldsymbol{M} = \begin{bmatrix} M_{xx} & M_{xy} & M_{xz} \\ M_{xy} & M_{yy} & M_{yz} \\ M_{xz} & M_{yz} & M_{zz} \end{bmatrix}$$

where *x, y, z* are North, East, Down direction at the source, respectively.

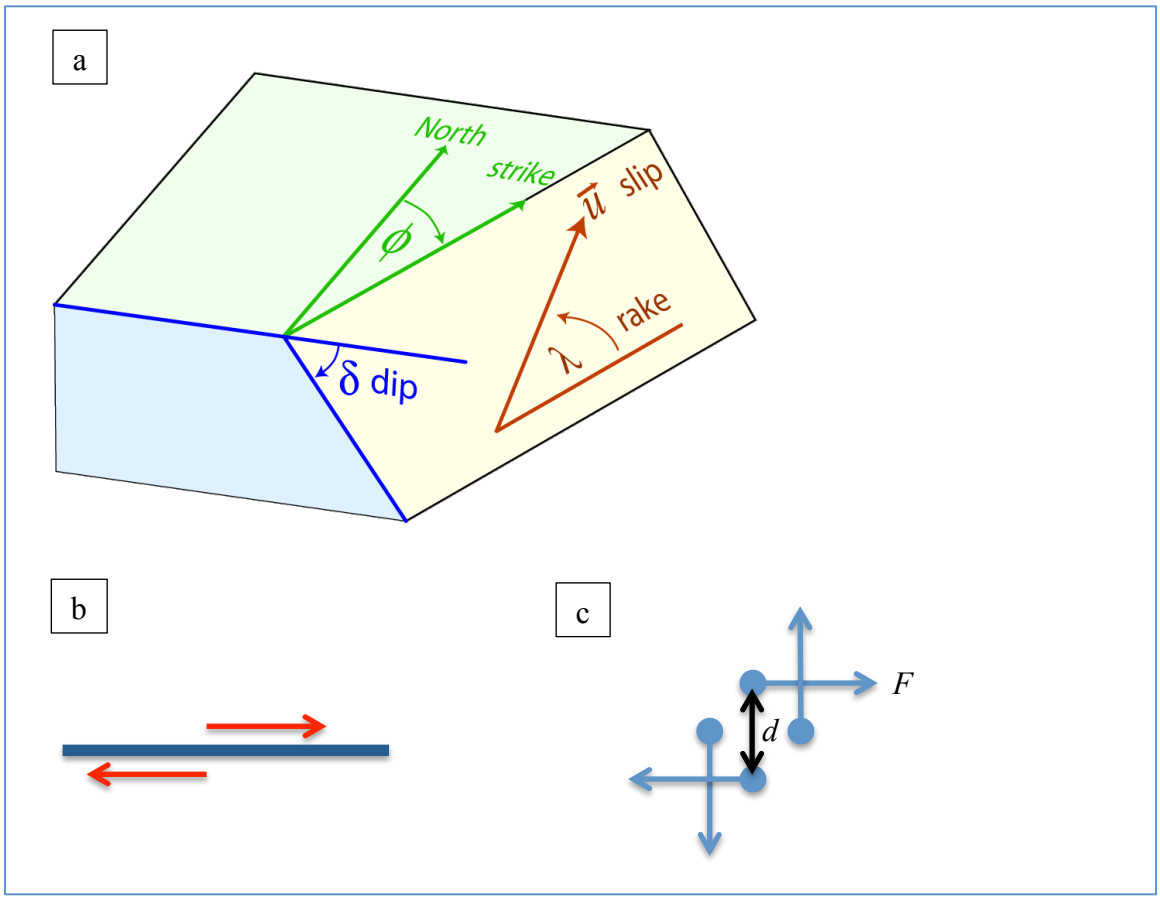

Figure 2.10. Finite fault model and a double-couple point source model.
(a) Definition of strike, dip and rake angles of a shear fault model. This figure is copied from http://www.gps.alaska.edu/jeff/Classes/GEOS655/strike_dip_rake.gif. $\vec{u}$ is the slip vector on the fault plane. (b) Bird's-eye view of a shear fault model for a vertical strike-slip earthquake with dip angle as 90°, and strike angle as 90°. Red arrows show the direction of slip on the fault plane. (c) Double couple point source model, equivalent to the fault model in (b), where *d* is the distance between one pair or 'couple' of point forces, and *F* is the force applied to a point.

The Cartesian components of the moment tensor ***M*** for a shear fault can be expressed by the strike, ϕ_s, dip, δ, rake angle, λ, and the seismic moment, M_0 (page 117 in [*Aki and Richards*, 1980]) as:

$$M_{xx} = -M_0\left(\sin\delta\cos\lambda\sin 2\phi_s + \sin 2\delta\sin\lambda\sin^2\phi_s\right)$$

$$M_{xy} = M_0\left(\sin\delta\cos\lambda\cos 2\phi_s + 1/2\sin 2\delta\sin\lambda\sin 2\phi_s\right) = M_{yx}$$

$$M_{xz} = -M_0\left(\cos\delta\cos\lambda\cos\phi_s + \cos 2\delta\sin\lambda\sin\phi_s\right) = M_{zx} \qquad (2.6)$$

$$M_{yy} = M_0\left(\sin\delta\cos\lambda\sin 2\phi_s - \sin 2\delta\sin\lambda\cos^2\phi_s\right)$$

$$M_{yz} = -M_0\left(\cos\delta\cos\lambda\sin\phi_s - \cos 2\delta\sin\lambda\cos\phi_s\right) = M_{zy}$$

$$M_{zz} = M_0\sin 2\delta\sin\lambda$$

For this double couple moment tensor, there are three invariants.

The first Invariant is: I_1 = Trace of the moment tensor = 0

The second Invariant is:

$$I_2 = 1/2[I_1^2 - \left(M_{xx}^2 + M_{xy}^2 + M_{xz}^2 + M_{yx}^2 + M_{yy}^2 + M_{yz}^2 + M_{zx}^2 + M_{zy}^2 + M_{zz}^2\right)] = -M_0^2$$

The third Invariant is:

$$I_3 = \text{determinant}(\boldsymbol{M}) = M_{xx}M_{yy}M_{zz} + 2M_{xy}M_{xz}M_{yz} - M_{xx}M_{yz}^2 - M_{yy}M_{xz}^2 - M_{zz}M_{xy}^2 = 0$$

Considering the symmetry of the moment tensor, and from the second invariant, we get the formula for the computation of seismic moment, M_0, as:

$$M_0^2 = \frac{1}{2}(M_{xx}^2 + M_{yy}^2 + M_{zz}^2) + M_{xy}^2 + M_{xz}^2 + M_{yz}^2$$

2.2.2 Linear algorithm between gravity change and point-source moment tensor

In this section, we show the linear relationship between coseismic gravity change and moment tensor elements. The design matrix relating moment tensor to gravity change is numerically retrieved from the output of Wang's PSGRN/PSCMP software [*Wang et al.*, 2006], based on dislocation theory in a layered half-space. Then we numerically validate the linear algorithm. This linear relationship is eventually used to establish the observation model for the inversion of source parameters from GRACE data and surface displacement data.

The theories of excitation of a normal mode by a seismic source [*Dahlen and Tromp,* 1998] have been thoroughly developed since the work by *Alterman et al.* [1959]. Based on the excitation theory, the surface displacement excited by a double-couple point source can be expressed as a linear function of moment tensor components [*Kanamori and Given,* 1981; equations 10.51 to 10.61 in *Dahlen and Tromp,* 1998]. Nevertheless, the coseismic surface displacement based on this normal-mode theory involves the infinite summation over the overtone number, which designates the order of eigenfrequencies. Nevertheless, ground based geodetic data such as GPS typically measure the 'static' coseismic displacement, rather than recording the temporal oscillations as seismic waves data do. Hence, the static deformation of the Earth is more suitably calculated from a dislocation theory, e.g., the analytic formula established by *Okada* [1985] for a homogeneous half-space. Starting from a layered spherical Earth, *Pollitz* [1996] further developed a method for calculating the 'static' coseismic displacement from the equation of equilibrium of the deformed Earth, avoiding the summation over the overtone number. Similar to the linear expression between

displacement and moment tensor, the 'static' coseismic gravitational potential perturbation can also be linearly calculated with respect to the point source seismic moment tensor [*Simons et al.,* 2009; *Han et al.,* 2013].

The linear relationship between gravity change and moment tensor can be denoted as:

$$\underset{n\times1}{y} = \underset{n\times1}{A_1}\,M_{xx} + \underset{n\times1}{A_2}\,M_{xy} + \underset{n\times1}{A_3}\,M_{xz} + \underset{n\times1}{A_4}\,M_{yy} + \underset{n\times1}{A_5}\,M_{yz} + \underset{n\times1}{A_6}\,M_{zz}$$

For a double-couple point source, we have the trace of the moment tensor equals zero. So considering $M_{xx} + M_{yy} + M_{zz} = 0$, we get

$$\underset{n\times1}{y} = \left(\underset{n\times1}{A_1} - \underset{n\times1}{A_4}\right)M_{xx} + \underset{n\times1}{A_2}\,M_{xy} + \underset{n\times1}{A_3}\,M_{xz} + \underset{n\times1}{A_5}\,M_{yz} + \left(\underset{n\times1}{A_6} - \underset{n\times1}{A_4}\right)M_{zz} = \underset{n\times5}{B}\,\underset{5\times1}{\xi} \tag{2.7}$$

where, $\underset{n\times1}{y} = [g_{D,1} \quad ... \quad g_{D,i} \quad ... \quad g_{D,n}]^T$, is the $n\times1$ vector, with each element, $g_{D,i}$, representing down component of gravity change at observation point, *i*. The design matrix relating moment tensor to gravity change is represented by *A* or *B*, *B*=[B_1, B_2, B_3, B_4, B_5], where $B_1 = \underset{n\times1}{A_1} - \underset{n\times1}{A_4}$, $B_2 = \underset{n\times1}{A_2}$, $B_3 = \underset{n\times1}{A_3}$, $B_4 = \underset{n\times1}{A_5}$, $B_5 = \underset{n\times1}{A_6} - \underset{n\times1}{A_4}$. $\underset{5\times1}{\xi}$ is composed of the moment tensor elements, $\underset{5\times1}{\xi} = \begin{bmatrix} M_{xx} & M_{xy} & M_{xz} & M_{yz} & M_{zz} \end{bmatrix}^T$, where *x, y, z* are North, East, Down respectively.

To retrieve the design matrix from software PSGRN/PSCMP, five elementary moment tensors are used. First moment tensor is realized by a point source ($\mathbf{M}^{(2)}$ as in pp 117 *Aki and Richards*, 1980) with dip angle as 90°, rake angle as 0°, strike angle as 135°, and the seismic moment as M_0, which yields a moment tensor with M_{xx}=M_0, M_{yy} =–M_0, and other components as zero. So we can get $\underset{5\times1}{\xi} = [\ M_0 \quad 0 \quad 0 \quad 0 \quad 0\ ]^T$; hence the model produced gravity change, y_1, with the input of this point source can give the first column

of design matrix as, $B_1 = \underset{n\times1}{A_1} - \underset{n\times1}{A_4} = y_1/M_0$. The second column of the design matrix, B_2, can be retrieved using the gravity change, y_2, from another point source ($\mathbf{M}^{(2a)}$) with dip angle as 90°, rake angle as 0°, strike angle as 0°, which gives $M_{xy}=M_0$, yielding $\underset{5\times1}{\xi} = [\ 0 \quad M_0 \quad 0 \quad 0 \quad 0\ ]^T$, leading to $B_2 = y_2/M_0$. The third column of the design matrix, B_3, can be retrieved using the gravity change, y_3, from the point source ($\mathbf{M}^{(1)}$) with dip angle as 0°, rake angle as 0°, strike angle as 180°, which gives $M_{xz}=M_0$, yielding $\underset{5\times1}{\xi} = [\ 0 \quad 0 \quad M_0 \quad 0 \quad 0\ ]^T$, leading to $B_3 = y_3/M_0$. The forth column of the design matrix, B_4, can be retrieved using the gravity change, y_4, from the point source ($\mathbf{M}^{(3)}$) with dip angle as 90°, rake angle as 90°, strike angle as 180°, which gives $M_{yz}=M_0$, yielding $\underset{5\times1}{\xi} = [\ 0 \quad 0 \quad 0 \quad M_0 \quad 0\ ]^T$, leading to $B_4 = y_4/M_0$. The last column of the design matrix, B_5, can be retrieved using the gravity change, y_5, from the point source ($\mathbf{M}^{(4)}$) with dip angle as 45°, rake angle as 90°, strike angle as 0°, yielding $M_{zz}=M_0$, $M_{yy}=-M_0$, and other components as zero, i.e., $\underset{5\times1}{\xi} = [\ 0 \quad 0 \quad 0 \quad 0 \quad M_0\ ]^T$, leading to $B_5 = \underset{n\times1}{A_6} - \underset{n\times1}{A_4} = y_5/M_0$. After retrieving the design matrix, the gravity change responding to any moment tensor can be simply computed using the linear relationship $\underset{n\times1}{y} = \underset{n\times5}{B}\,\underset{5\times1}{\xi}$.

Where

$$\mathbf{M}^{(2)} = M_0\begin{bmatrix} 1 & 0 & 0 \\ 0 & -1 & 0 \\ 0 & 0 & 0 \end{bmatrix},\ \mathbf{M}^{(2a)} = M_0\begin{bmatrix} 0 & 1 & 0 \\ 0 & 0 & 0 \\ 0 & 0 & 0 \end{bmatrix},\ \mathbf{M}^{(1)} = M_0\begin{bmatrix} 0 & 0 & 1 \\ 0 & 0 & 0 \\ 0 & 0 & 0 \end{bmatrix}$$

$$\mathbf{M}^{(3)} = M_0 \begin{bmatrix} 0 & 0 & 0 \\ 0 & 0 & 1 \\ 0 & 0 & 0 \end{bmatrix}, \mathbf{M}^{(4)} = M_0 \begin{bmatrix} 0 & 0 & 0 \\ 0 & -1 & 0 \\ 0 & 0 & 1 \end{bmatrix}$$

To numerically verify the linear algorithm, we compare the coseismic gravity change from the direct computation with that from the linear relationship. As shown in Figure 2.11 *upper right*, the down component of gravity change on Earth surface is calculated using Wang's PSGRN/PSCMP software. The given earth model is the Preliminary Reference Earth Model (PREM) model [*Dziewonski and Anderson,* 1981]. The input source parameter is the GCMT (Global Centroid Moment Tensor) centroid solution for the 2011 Tohoku earthquake, with strike angle as 203°, dip as 10°, rake as 88°, and M_0 as 5.312×10^{29} dyne×cm. From these four variables, we compute each moment tensor element using equation (2.6), leading to the parameter vector ξ. Then we calculate the gravity change using the linear relationship $\underset{n\times1}{y} = \underset{n\times5}{B}\,\underset{5\times1}{\xi}$. The difference of the gravity change between the two methods is shown in Figure 2.11 *lower right*, less than 0.1 μGal, which is only 2×10^{-6} of the peak coseismic gravity change, ~50,000 μGal (Figure 2.11 *upper right*). The similar linear relationship between surface displacement and moment tensor is also carried out and numerically validated. The difference for the surface displacement to north direction is up to –10 cm (Figure 2.11 *lower left*), negligible compared to the peak coseismic displacement up to –28,000 cm (Figure 2.11 *upper left*). The difference for the upward surface displacement is up to –35 cm (Figure 2.11 *lower middle*), much smaller than the peak coseismic displacement up to 55,000 cm (Figure 2.11 *upper middle*).

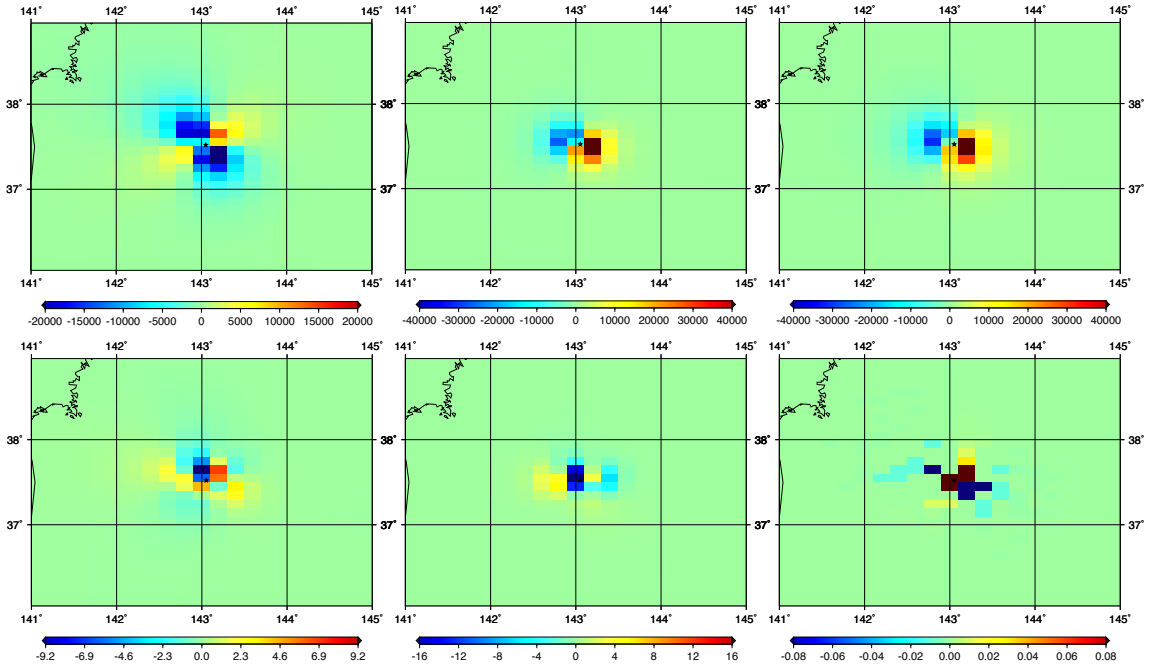

Figure 2.11. The comparison of directly computed gravity change and displacement with that from the linear relationship.
First row: coseismic surface displacement and gravity change by PSGRN/PSCMP for the GCMT centroid solution of 2011 Tohoku earthquake. ***Left:*** surface displacement to north in cm; ***Middle:*** upward surface displacement in cm; ***Right:*** down component of gravity change, g_D, in μGal. ***Second row:*** coseismic displacement and gravity change by the linear algorithm minus the results in first row.

To be consistent with the GRACE-observed gravity and gravity gradient change, the model-predicted all components of gravity and gravity gradient change are further processed as discussed in Section 2.1.1 start from the down component of gravity change and displacement on Earth's surface due to the solid Earth deformation. The further modeling process includes the computation of ocean response on gravity change, the spherical harmonic transformation and truncation, the computation of each component of gravity and gravity gradient from the geopotential coefficients. We can see that each step is a linear algorithm, which leads to a linear relationship between the GRACE-observed gravity and gravity gradient change and the seismic moment tensor. To numerically

validate the linear relationship, we first compute the north, east, down component of gravity change (Figure 2.12 *first row*) up to degree 59 directly using the data processing method as described in section 2.1.1. As a comparison, we then compute the gravity change up to degree 59 from the linear algorithm with the moment tensor elements. The difference between the two methods, as shown in Figure 2.12 *second row*, representing the error in the numerically retrieved linear algorithm, is around 0.02 μGal, about 0.07% of the directly computed gravity change (Figure 2.12 *first row*). This difference/error is dominated by the error in the linear algorithm for gravity change due to the passive ocean response, which is three orders of magnitude larger than the error (about 2×10^{-5} μGal) in the linear algorithm for the gravity change from solid earth deformation. The relative difference/error of the linear algorithm for gravity change due to the passive ocean response is at the same order of magnitude of the relative difference for the upward displacement (Figure 2.11 *lower middle*), consistent with the fact that the surface density change is a linear function of the vertical displacement (equation 2.1). This equivalence of the two relative errors implies that the error for the linear algorithm for gravity change due to the passive ocean response mainly comes from the error in the linear algorithm for the vertical displacement, and that the post processing of the gravity change due to the passive ocean response from the vertical deformation does not contribute much numerical error to the linear algorithm. Similarly for gravity gradient change, the error of the linear algorithm is also about 10^{-3} of the directly computed gravity gradient change.

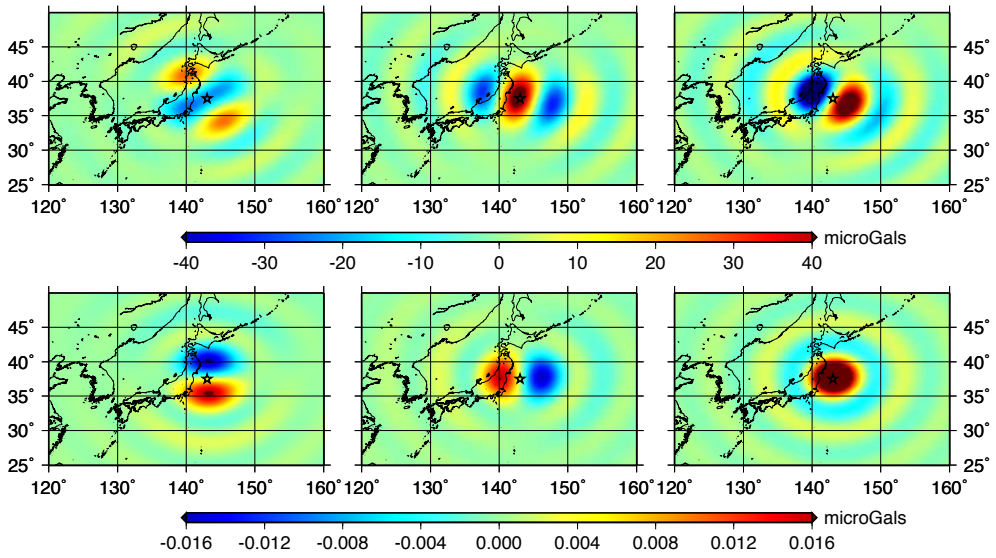

Figure 2.12. The comparison of directly computed gravity change due to both solid Earth deformation and ocean response with that from the linear algorithm.
First row: north (***left***), east (***middle***), down (***right***) component of gravity up to degree 59 due to both solid Earth deformation and ocean response, computed from the surface displacement and gravity change due to solid Earth deformation only (Figure 2.11 *first row*). ***Second row:*** coseismic gravity change by the linear algorithm minus the results in first row.

2.3 The least-squares estimation of double-couple point source

As discussed above, the north component of gravity and gravity gradient change due to solid Earth deformation and the passive response of ocean water can be expressed as an explicit linear function of seismic moment tensor components. From this linear algorithm, the seismic moment tensor can be straightforwardly resolved using least-squares adjustment. Nevertheless, the coseismic deformation and gravitational perturbation is a non-linear function of centroid depth and location, so the simulated annealing algorithm [*Kirkpatrick et al.*, 1983; *Goffe et al.*, 1994] is adopted to solve for the centroid depth and location. This section describes the method to solve for source parameters of a point source from GRACE data and GPS data.

2.3.1 Estimation from GRACE data

Based on the linear relationship shown in section 2.2.2, we have the observation model for GRACE-derived north component of gravity and gravity gradient change as:

$$\underset{4n_1\times 1}{y_I} = \underset{4n_1\times 5}{A_I}\ \underset{5\times 1}{\xi} + \underset{4n_1\times 1}{e_I} \tag{2.8}$$

$\underset{4n_1\times 1}{y_I}$ is the vector of observations, composed of the g_N, Txx, Txy, and Txz at grid point 1 to n_1, $y_I^T = \begin{bmatrix} g_{N,1} & \cdots & g_{N,n_1} & T_{xx,1} & \cdots & T_{xx,n_1} & T_{xy,1} & \cdots & T_{xy,n_1} & T_{xz,1} & \cdots & T_{xz,n_1} \end{bmatrix}$, where $g_{N,1}$ is g_N at point 1; $\underset{4n_1\times 5}{A_I}$ is the design matrix; $\underset{5\times 1}{\xi}$ is the unknown parameter vector, composed of the moment tensor elements, $\underset{5\times 1}{\xi} = \begin{bmatrix} M_{xx} & M_{xy} & M_{xz} & M_{yz} & M_{zz} \end{bmatrix}^T$, where x, y, z are North, East, Down direction, respectively. $\underset{4n_1\times 1}{e_I}$ is the error vector for the observations. The dispersion matrix for this error vector is given as,

$$\underset{4n_1\times 4n_1}{\Sigma_I} = \underset{4n_1\times 4n_1}{D\{e_I\}} = \begin{bmatrix} \underset{n_1\times n_1}{D\{g_N\}} & 0 & 0 & 0 \\ 0 & \underset{n_1\times n_1}{D\{T_{xx}\}} & 0 & 0 \\ 0 & 0 & \underset{n_1\times n_1}{D\{T_{xy}\}} & 0 \\ 0 & 0 & 0 & \underset{n_1\times n_1}{D\{T_{xz}\}} \end{bmatrix} \tag{2.9}$$

where $\underset{n_1\times n_1}{D\{g_N\}} = \begin{bmatrix} \sigma^2_{g_N,1} & 0 & 0 \\ 0 & \ddots & 0 \\ 0 & 0 & \sigma^2_{g_N,n_1} \end{bmatrix}$, with the unit as μGal^2; $\sigma^2_{g_N,1}$ is the square of the standard deviation of g_N change at point 1, which is evaluated by the error propagation of the linear fit model with the Heaviside step function. The similar diagonal dispersion

matrix for *Txx*, *Txy*, and *Txz* is denoted as, $D\{T_{xx}\}$, $D\{T_{xy}\}$, and $D\{T_{xz}\}$, respectively, with the unit as mE^2. As shown, we assume there is no correlation between g_N change at different observation points, and there is no correlation between g_N, *Txx*, *Txy*, and *Txz* change.

From the observation model, we can get the least-squares solution for the point-source moment tensor as:

$\hat{\xi} = \left(A_I^T \Sigma_I^{-1} A_I\right)^{-1} A_I^T \Sigma_I^{-1} y_I$, with its dispersion matrix as $D\left\{\hat{\xi}\right\} = \left(A_I^T \Sigma_I^{-1} A_I\right)^{-1}$ (2.10)

Assuming the point source is a double-couple source, the further constraint of zero determinant must be imposed on the seismic moment. So we aim to solve for the least-squares solution of the observation model with fixed constraint. The fixed constraint, i.e., the third invariant equals to zero, can be expressed as:

$$f(\xi) = M_{xx}M_{yy}M_{zz} + 2M_{xy}M_{xz}M_{yz} - M_{xx}M_{yz}^2 - M_{yy}M_{xz}^2 - M_{zz}M_{xy}^2 = 0 \quad (2.11)$$

To linearize the above fixed constraint, we have

$$f(\xi) \approx f(\xi_0) + \left.\frac{\partial f}{\partial \xi}\right|_{\xi_0} (\xi - \xi_0) = 0$$

Let $\kappa_0 = -f(\xi_0) + \left.\frac{\partial f}{\partial \xi}\right|_{\xi_0} \xi_0$, and $\underset{1\times 5}{K} = \left.\frac{\partial f}{\partial \xi}\right|_{\xi_0}$, then we get the linearized fixed constraint as:

$$\kappa_0 = K\xi \quad (2.12)$$

Then the least-squares solution for the observation model with fixed constraint is:

$$\hat{\xi} = N_I^{-1} c_I + N_I^{-1} K^T \left(K N_I^{-1} K^T\right)^{-1} \left(\kappa_0 - K N_I^{-1} c_I\right) \quad (2.13)$$

Its dispersion matrix is $D\left\{\hat{\xi}\right\} = N_I^{-1} - N_I^{-1} K^T \left(K N_I^{-1} K^T\right)^{-1} K N_I^{-1}$, where $N_I = A_I^T \Sigma_I^{-1} A_I$, $c_I = A_I^T \Sigma_I^{-1} y_I$. The residual vector is: $\tilde{e}_I = y_I - A_I \hat{\xi}$

Using the estimated $\hat{\xi}$ with no constraint in equation (2.10) as the initial value for the ξ_0, we then compute the least-squares solution with the fixed constraint iteratively until the non-linear fixed constraint (equation 2.11) is smaller than the given termination criteria, ε, i.e., the iteration ends when $f\left(\hat{\xi}\right) < \varepsilon$.

To evaluate the strike, ϕ_s, dip, δ, rake angle, λ, and the seismic moment, M_0, from the above estimated moment tensor elements and its dispersion matrix [*Han et al.*, 2013], we start from the equation of moment tensor as a function of the four parameters (equation 2.6). We have $\underset{5\times1}{y_M} = g\left(\xi_a\right) + \underset{5\times1}{e_M}$, where $y_M = \hat{\xi}$, is composed by the estimated moment tensor elements, with its dispersion matrix as $D\{y_M\} = D\left\{\hat{\xi}\right\}$. ξ_a is the unknown parameters, $\xi_a = \begin{bmatrix} \phi_s & \delta & \lambda & M_0 \end{bmatrix}^T$. $g\left(\xi_a\right)$ is composed by the five equations for M_{xx}, M_{xy}, M_{xz}, M_{yz}, M_{zz} as in equation (2.6).

This observation model is then linearized as:

$$\underset{5\times1}{y_M} \approx g\left(\xi_{a,0}\right) + + \left.\frac{\partial g}{\partial \xi_a}\right|_{\xi_{a,0}} \left(\xi_a - \xi_{a,0}\right) + \underset{5\times1}{e_M} \tag{2.14}$$

Hence, the $\hat{\xi}_a$ can be further estimated by the least-squares adjustment through iteration. Its corresponding dispersion matrix $D\left\{\hat{\xi}_a\right\}$ can be used to evaluate the correlation matrix between the four parameters. Assuming $c_{i,j}$ is the *i*-th row and *j*-th column of the dispersion matrix, then the correlation between the *i*-th parameter and *j*-th parameter of $\hat{\xi}_a$ can be computed as

$$\rho_{i,j} = c_{i,j} \Big/ \sqrt{c_{i,i} c_{j,j}} \tag{2.15}$$

Here, the observation model is established for a given centroid location, and the moment tensor elements, or the strike, dip, rake angle and the seismic moment are the to-be-determined parameters. To find the optimal centroid location and depth, we adopt the simulated annealing algorithm discussed in section 4.1.1. During the inversion, the moment tensor is estimated for each trial of centroid location and depth, and then the simulated annealing algorithm is used to find the optimal centroid location and depth that produce the minimum of a target function. We define the target function as the mean of the relative difference for g_N, *Txx*, *Txy*, and *Txz*:

$$\Phi\left(lat, lon, depth\right) = \left(rd_{g_N} + rd_{T_{xx}} + rd_{T_{xy}} + rd_{T_{xz}}\right) / 4 \tag{2.16}$$

where, *lat, lon, depth* is the latitude, longitude, depth of the centroid, respectively. The relative difference, *rd*, between the model estimation, $m(\theta,\lambda)$, and the GRACE observation $y(\theta,\lambda)$ is defined as:

$$rd = \sqrt{\sum_{\theta}\sum_{\lambda}\left(y(\theta,\lambda) - m(\theta,\lambda)\right)^2 / n_1} \Big/ \sqrt{\sum_{\theta}\sum_{\lambda} y(\theta,\lambda)^2 / n_1} \times 100\% \tag{2.17}$$

n_1 is the number of evaluation points; θ is the colatitude, and λ is the longitude of the grid point of the GRACE-derived gravity change. $y(\theta,\lambda)$ could be either g_N, or *Txx*, *Txy*, *Txz*. As shown, the difference between model GRACE observation and model estimation is actually the residual vector, i.e. $y(\theta,\lambda) - m(\theta,\lambda) = \tilde{e}_1(\theta,\lambda)$.

2.3.2 Estimation from GPS data

The observation model for GPS-measured surface displacement can be expressed as:

$$\underset{3n_2\times 1}{y_{II}} = \underset{3n_2\times 5}{A_{II}}\ \underset{5\times 1}{\xi} + \underset{3n_2\times 1}{e_{II}} \tag{2.18}$$

where $y_{II}^T = \begin{bmatrix} u_{N,1} & \dots & u_{N,n_2} & u_{E,1} & \dots & u_{E,n_2} & u_{D,1} & \dots & u_{D,n_2} \end{bmatrix}$, with u_N, u_E, u_D as the north, east, down component of surface displacement in meters, and u_{N,n_2} is the displacement in north direction at observation point n_2. A_{II} is the design matrix. ξ is the unknown parameter vector of the moment tensor elements. e_{II} is the error vector for the observations. The dispersion matrix for this error vector is given as,

$$\Sigma_{II} = \underset{3n_2\times 3n_2}{D\{e_{II}\}} = \begin{bmatrix} \underset{n_2\times n_2}{D\{u_N\}} & 0 & 0 \\ 0 & \underset{n_2\times n_2}{D\{u_E\}} & 0 \\ 0 & 0 & \underset{n_2\times n_2}{D\{u_D\}} \end{bmatrix} \tag{2.19}$$

where $D\{u_N\}$, $D\{u_E\}$, $D\{u_D\}$ are the diagonal dispersion matrix for u_N, u_E, u_D, respectively, in meter^2, e.g.,

$$D\{u_N\} = \begin{bmatrix} \sigma_{u_N,1}^2 & 0 & 0 \\ 0 & \ddots & 0 \\ 0 & 0 & \sigma_{u_N,n_2}^2 \end{bmatrix}$$

$\sigma_{u_N,1}^2$ is the square of the standard deviation of u_N, which is given along with the measurements. Again, we assume there is no correlation between the three component of displacements, and no correlation between measurements at different observation points. The same as discussed in the previous section, the fixed constraint of the zero determinant is further considered for a double-couple point source. The least-squares solution for the observation model with the fixed constraint is:

$$\hat{\xi} = N_{II}^{-1}c_{II} + N_{II}^{-1}K^T\left(KN_{II}^{-1}K^T\right)^{-1}\left(\kappa_0 - KN_{II}^{-1}c_{II}\right) \tag{2.20}$$

Its dispersion matrix is $D\left\{\hat{\xi}\right\} = N_{II}^{-1} - N_{II}^{-1}K^T\left(KN_{II}^{-1}K^T\right)^{-1}KN_{II}^{-1}$, where $N_{II} = A_{II}^T\Sigma_{II}^{-1}A_{II}$, $c_{II} = A_{II}^T\Sigma_{II}^{-1}y_{II}$. The residual vector is: $\tilde{e}_{II} = y_{II} - A_{II}\hat{\xi}$

The similar iteration is carried out to fulfill the non-linear constraint in equation (2.11). The target function for finding the optimal centroid location and depth is:

$$\Phi\left(lat, lon, depth\right) = \sqrt{\tilde{e}_{II}^T\tilde{e}_{II}} \Big/ \sqrt{y_{II}^T y_{II}} \times 100\% \tag{2.21}$$

where, *lat, lon, depth* is the latitude, longitude, depth of the centroid, respectively. This target function is basically the same as the relative difference in equation (2.17) for GRACE data.

2.3.3 Joint Estimation from GRACE data and GPS data

To combine the two data sets, we establish the combined observation model:

$$\underset{(4n_1+3n_2)\times 1}{y} = \underset{(4n_1+3n_2)\times 5}{A}\underset{5\times 1}{\xi} + \underset{(4n_1+3n_2)\times 1}{e} \tag{2.22}$$

where $y = \begin{bmatrix} y_I \\ y_{II} \end{bmatrix}$, $A = \begin{bmatrix} A_I \\ A_{II} \end{bmatrix}$, $e = \begin{bmatrix} e_I \\ e_{II} \end{bmatrix}$. The dispersion matrix is provided as:

$\Sigma = D\left\{e\right\} = \begin{bmatrix} \Sigma_I & 0 \\ 0 & \Sigma_{II} \end{bmatrix}$, which assumes there is no correlation between GRACE measurements and GPS data.

Based on the least-squares adjustment, the objective is to find the estimated parameter $\hat{\xi}$ that will minimize the Lagrange target function:

$$\Phi\left(\xi\right) = \left(y - A\xi\right)^T\Sigma^{-1}\left(y - A\xi\right) = e_I^T\Sigma_I^{-1}e_I + e_{II}^T\Sigma_{II}^{-1}e_{II}$$

The least-squares solution is:

$$\hat{\xi} = \left(A^T \Sigma^{-1} A\right)^{-1} A^T \Sigma^{-1} y \text{, with its dispersion matrix as } D\left\{\hat{\xi}\right\} = \left(A^T \Sigma^{-1} A\right)^{-1} \quad (2.23)$$

We further impose the zero determinant as a fixed constraint to a double-couple point source. Similar to the previous sections, the least-squares solution for the observation model with the fixed constraint is:

$$\hat{\xi} = N^{-1}c + N^{-1}K^T\left(KN^{-1}K^T\right)^{-1}\left(\kappa_0 - KN^{-1}c\right) \quad (2.24)$$

Its dispersion matrix is $D\left\{\hat{\xi}\right\} = N^{-1} - N^{-1}K^T\left(KN^{-1}K^T\right)^{-1}KN^{-1}$

where $N = A^T\Sigma^{-1}A = A_I^T\Sigma_I^{-1}A_I + A_{II}^T\Sigma_{II}^{-1}A_{II}$, $c = A^T\Sigma^{-1}y = c_I + c_{II}$.

The residual vector is: $\tilde{e} = y - A\hat{\xi}$

The iteration is carried out to fulfill the non-linear constraint of the equation (2.11). To further find the optimal centroid location, we choose the target function to be minimized as:

$$\Phi\left(lat, lon, depth\right) = \sqrt{\left(\tilde{e}_I^T\Sigma_I^{-1}\tilde{e}_I + \tilde{e}_{II}^T\Sigma_{II}^{-1}\tilde{e}_{II}\right)} \Big/ \sqrt{\left(y_I^T\Sigma_I^{-1}y_I + y_{II}^T\Sigma_{II}^{-1}y_{II}\right)} \times 100\% \quad (2.25)$$

where, *lat, lon, depth* is the centroid latitude, longitude, and depth.

2.4 Simulation

This section presents the simulation studies for the inversion of point source from GRACE data and the surface displacement from GPS data. Here we use the 2011 Mw=9.0 Tohoku earthquake as a study case. We adopt the GCMT centroid solution in Section 2.2.2 for the 2011 Tohoku earthquake as the known input source parameters. Then the simulated north component of gravity change up to degree 59 corresponding to the input source parameters can be calculated as shown in Figure 2.12 (*top left*), as well

as for the north component of gravity gradient change. The surface displacement data on 1,216 GPS stations and 5 GPS/acoustic sea-floor sites [*Sato et al.*, 2011] near Japan are also simulated (Figure 2.13). From these simulated GRACE gravity and gravity gradient change data and the surface displacement data, the source parameters are then inverted from either of the data sets or the combination of GRACE and GPS data, using the inversion scheme discussed in Section 2.3.

Several scenarios are carried out to evaluate the accuracy and precision of each source parameter constraint by GRACE data assuming the location of the point source is known. Using the simulated g_N, *Txx*, *Txy*, *Txz* change with no measurement noise, the first scenario (scheme *a0* in Table 2.1) inverts for the five elements of moment tensor based on the least-squares adjustment method discussed in Section 2.3.1, without adding the fixed constraint of the zero determinant. We calculate the error as the difference between the estimated moment tensor element and the input moment tensor element (the first line in Table 2.1) that is computed from the strike, dip, rake angle and the moment. We can see that the error is worst for the M_{xx}, M_{zz} component. To evaluate the effect of adding the fixed constraint to the least-squares adjustment, the second scenario (scheme *a1*) is carried out, which is the same as scheme *a0* except adding the fixed constraint. We can see that by adding the fixed constraint, the error of M_{xx}, M_{zz} component is reduced by about three times, as well as that for M_0 and dip angle. We further add a random noise of 1.2 μGal for g_N and 0.1 mE for gravity gradients for the inversion (scheme *a2*). It is shown that by adding the noise commensurate with GRACE measurements, the error of the north-associated components of moment tensor does not increase much, especially for the M_{xx}, while the error of the east and down components of moment tensor (M_{yz}, M_{zz})

increases by more than ten times, which can be explained by the relatively less sensitivity of GRACE measurements to the east and down component of gravity and gravity gradient change as discussed in Section 3.3. The standard deviation of each moment tensor element is consistent with its error, and similar consistency holds for the three angles, demonstrating that the standard deviation is a reasonable indicator of the absolute error. As shown, M_{zz} has the worst precision, followed by M_{yz}. Compared to the good precision of the dip angle, the worse accuracy and precision in strike and rake angle are probably caused by the trade-off between these two angles as discussed in the sensitivity test, as well as the strong correlation shown between these two angles (Table 2.2 *left panel*).

The GPS coseismic displacement data produced by the ARIA team at JPL and Caltech can be downloaded from ftp://sideshow.jpl.nasa.gov/pub/usrs/ARIA/ (last accessed February 2015). Geodetic observations at five sea-floor sites by using the GPS/acoustic combination technique are available from Table S1 in [*Sato et al.*, 2011]. The surface displacement on these GPS stations and five sea-floor sites are forward modeled corresponding to the GCMT centroid solution for the 2011 Tohoku earthquake.

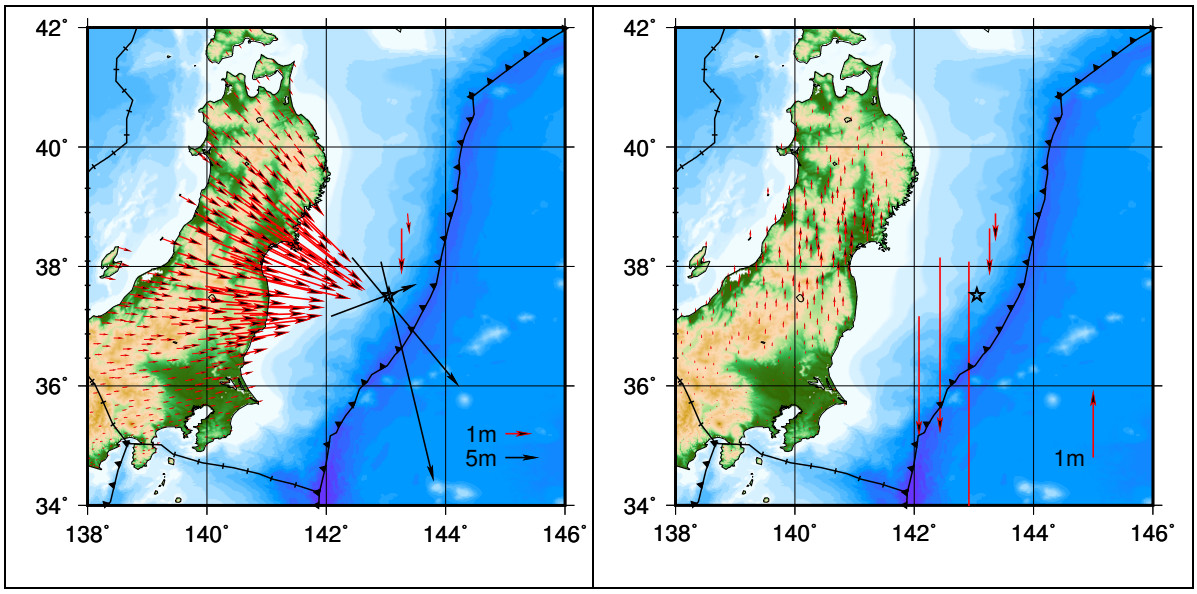

Figure 2.13. Simulated surface displacement on GPS stations and five sea floor sites. The horizontal (***left***) and vertical (***right***) displacements are simulated from the GCMT centroid solution of the 2011 Tohoku earthquake based on PREM earth model using PSGRN/PSCMP software.

Here we evaluate the accuracy and precision of the source parameters that are inverted from the simulated displacement data on over a thousand of stations. First, the simulated surface displacements u_N, u_E, u_D of the on-land GPS stations and seafloor sites with no measurement noise are used to solve for the source parameters (scheme *b1*) with the fixed constraint. Then a random noise of 0.04 meter is added to the displacements (scheme *b2*). We can see that either with or without random noise, GPS data tend to give worst accuracy/precision for M_{xz}, M_{yz}, while GRACE data tend to yield worst precision for M_{yz}, M_{zz}. This indicates that GRACE data and GPS data can compensate each other on the constraint of moment tensor. Nevertheless, similar to the use of GRACE data, there is also strong correlation (Table 2.2 *right panel*) between the strike and rake angles from GPS data, leading to their worse standard deviation as compared to dip angle. In addition, the correlation, –0.8, between dip angle and moment from GPS data (Table 2.2 *right panel*) is larger than that from GRACE data. To test the contribution of the five seafloor

sites, another scenario without the seafloor displacement data (scheme *b3*) is carried out. As shown, accuracy and precision get worse significantly to about one order of magnitude, especially for M_{xz}, M_{yz}, and the three angles. Consistent with the conclusion in [*Wei et al.*, 2012; *Wang et al.,* 2013], the five ocean bottom GPS/acoustic displacement data set greatly improves the precision of the inversion, showing the importance of the GPS stations' configuration on the inversion of source parameter.

By combing the two data sets, it shows the contribution from GRACE data to source parameters inversion, especially for the constraint on the offshore deformation. As discussed in last paragraph, without the ocean floor displacement data, the precision on source parameters from on-land GPS data only (scheme *b3*) is very poor. By combining with GRACE data, the precision (scheme *c3*) improves significantly, showing that GRACE data can compensate the poor configuration of GPS stations. The sensitivity of GRACE data over offshore seismic deformations is supported by the better spatial coverage of the satellite measurements. In addition, even for combining with the ocean floor data, the joint solution (scheme *c2*) improves the solution precision for all source parameters, as shown by the fact that the standard deviation of the estimated parameters is smaller than the standard deviation by either the GRACE data only (scheme *a2*) or that by GPS data only (scheme *b2*). Furthermore, the joint solution significantly reduces the correlation between dip angle and moment to zero (Table 2.2) from the –0.8 in the case of GPS-only solution and the 0.4 for the case of the GRACE-only solution.

The centroid location and depth is further inverted using the SA algorithm. The simulated onshore and offshore displacement data with random noise of 0.04 m are used for the inversion. As shown in the Figure 2.14, the optimal location converges to the input given

location very well, after about 20000 iterations. The relative difference, which is the value of the target function (equation 2.21), is close to zero (0.05%) at the optimal location. For this SA algorithm, we define the solution uncertainty as the half of the range (Figure 2.14), which produces no more than 0.1% of the relative differences as compared to the optimal solution. As shown in Figure 2.14, the uncertainty for longitude, latitude, and depth is 0.1 km, 0.15 km, 0.1 km, respectively. Again, if the five ocean bottom displacement data are not included, the estimated location with the minimum target function (1.7%) is 143.04°E, 37.521°N, 19.875 km, which is about 1 km west, 0.1 km north and 0.1 km shallower relative to the given input location. The target function is larger, about 3.4%, if the location is fixed at the input location. We can see that with the GPS stations distributed on the west side of the centroid, the error of the estimated location got increased largely. The error along east west direction is especially large, ten times of the error along the north south direction, which is due to the fact that no stations distributed on along the east-west dimension of the centroid to constrain the location along this dimension. By measuring right above the fault area, GRACE data can overcome the inadequacy of the poor configuration of GPS stations, and provide good constraint on the centroid location, which is demonstrated by the small error within 0.1 km for the SA inversion of location from the simulated GRACE-observed g_N, *Txx*, *Txy*, *Txz* change with random noise.

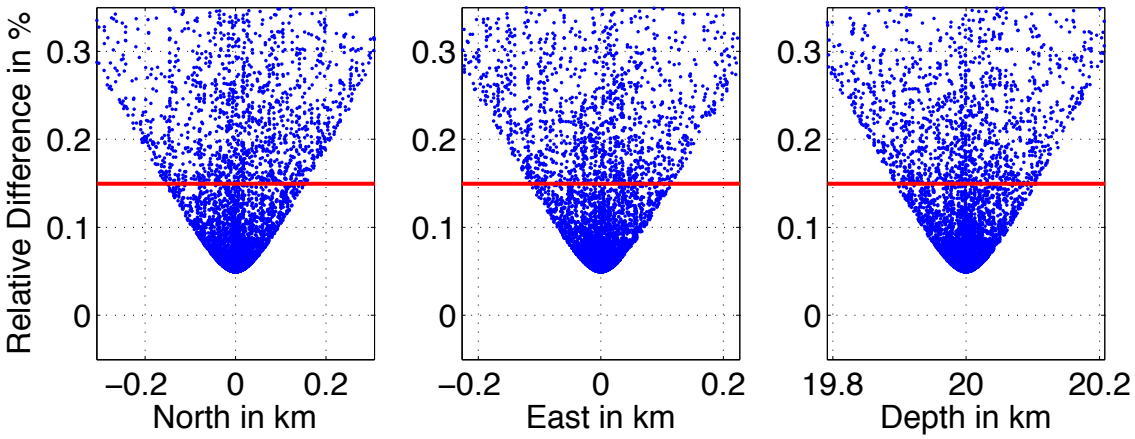

Figure 2.14. Solution uncertainty for the inversion from onshore and offshore GPS/Acoustic displacements.
Each blue dot is a trial of latitude (***left***), longitude (***middle***), and depth (***right***) during inversion. The minimum relative difference gives the optimal solution, which is 143.05°E, 37.52°N, 20 km, same with the given value. The latitude and longitude is transformed to Cartesian coordinates with origin at the optimal location, with first axis pointing to North and second axis pointing to East. The red horizontal line is the threshold bar for the definition of solution uncertainty, which is 0.1 plus the minimum relative difference. As shown, the latitudinal range [–0.15, 0.15] km can give relative differences lower than the red line. This range is defined as solution uncertainty. The uncertainty along longitude direction (***middle***) is 0.1 km, and the uncertainty for depth is 0.1 km (***right***).

		Moment tensor component in (10^{19} Nm)					Moment in (10^{19} Nm), angles in (°)			
		M_{xx}	M_{xy}	M_{xz}	M_{yz}	M_{zz}	M_0	Strike	Dip	Rake
Input value		−300	675	2117	−4521	1816	5312	203	10	88
Scheme *a0*	error	2	−0.1	0.1	0.1	−3	−0.7	−0.06	−0.009	−0.06
Scheme *a1*	error	0.8	−0.5	0.1	0.08	0.7	0.2	−0.08	−0.004	−0.07
Scheme *a2*	error	−0.9	4	0.6	5	10	1	−0.1	0.08	−0.2
	std	2	2	2	4	6	4	0.2	0.03	0.2
Scheme *b1*	error	0.1	−0.1	−0.6	−0.5	−0.08	0.2	0.0007	−0.001	0.01
Scheme *b2*	error	2	−2	−2	−10	−0.5	8	−0.07	−0.02	−0.004
	std	4	4	9	20	6	11	0.4	0.05	0.5
Scheme *b3*	error	10	−7	120	24	−7	27	−2	−0.06	−3
	std	14	11	150	110	23	111	2	0.3	4
Scheme *c2*	error	0.4	1.4	0.08	4.8	7.5	−1.5	−0.15	0.05	−0.2
	std	1.5	1.6	1.9	3.4	3.5	3	0.1	0.02	0.1
Scheme *c3*	error	−0.8	2	0.4	6	7	−2	−0.06	0.04	−0.08
	std	1.9	2	2	3.5	3.9	3	0.1	0.02	0.1

Table 2.1. Accuracy and precision of estimated parameters for several schemes.
Error = estimated value – true value (input value)
Scheme *a0* using simulated GRACE-observed g_N, *Txx*, *Txy*, *Txz* change, with no measurement noise.
Scheme *a1* using simulated GRACE-observed g_N, *Txx*, *Txy*, *Txz* change, with no measurement noise, solved with fixed constraint.
Scheme *a2* using simulated GRACE-observed g_N, *Txx*, *Txy*, *Txz* change, with random noise of 1.2 μGal for g_N and 0.1 mE for gravity gradients, solved with fixed constraint.
Scheme *b1* using simulated surface displacements u_N, u_E, u_D on 1221 onshore and offshore GPS/Acoustic stations with no measurement noise, solved with the fixed constraint.
Scheme *b2* using simulated surface displacements u_N, u_E, u_D on 1221 onshore and offshore GPS/Acoustic stations with random noise of 0.04 meter, solved with fixed constraint.
Scheme *b3* using simulated surface displacements onshore GPS stations only without the five offshore GPS/Acoustic stations, with random noise of 0.04 meter, solved with fixed constraint.
Scheme *c2* combined solution using simulated GRACE-observed g_N, *Txx*, *Txy*, *Txz* change with random noise of 1.2 μGal for g_N and 0.1 mE for gravity gradients (as in scheme *a2*), and simulated surface displacements u_N, u_E, u_D on 1221 onshore and offshore GPS/Acoustic stations with random noise of 0.04 meter (as in scheme *b2*), solved with fixed constraint.

	Strike	Dip	Rake	M_0
Strike	1.0	–0.3	1.0	–0.2
Dip	–0.3	1.0	–0.3	0.4
Rake	1.0	–0.3	1.0	–0.1
M_0	–0.2	0.4	–0.1	1.0

Strike	Dip	Rake	M_0
1.0	–0.3	1.0	0.4
–0.3	1.0	–0.4	–0.8
1.0	–0.4	1.0	0.5
0.4	–0.8	0.5	1.0

Strike	Dip	Rake	M_0
1.0	–0.2	1.0	–0.1
–0.2	1.0	–0.2	0.0
1.0	–0.2	1.0	0.0
–0.1	0.0	0.0	1.0

Table 2.2. The correlation between parameters.
Left panel for GRACE data only (scheme *a2*), the ***middle*** panel for GPS data only (scheme *b2*), and the ***right*** panel is for the joint solution of GRACE data and GPS data (scheme *c2*).

Chapter 3. Improved GRACE Data Processing

3.1 Heaviside step function for coseismic gravity change detection

Different data processing methods [*Han et al.*, 2006; *Matsuo & Heki*, 2011; *Cambiotti and Sabadini*, 2012; *Wang et al.*, 2012b] have been applied to retrieve coseismic gravity change signal from GRACE data. *Han et al.* [2006] took the difference of gravity change several months after the earthquake with the gravity change during the same months of the year before, to suppress the seasonal gravity variations. Similar method of subtracting measurements before and after earthquake was also applied in [*Han et al.,* 2010, 2011]. Although this method of subtracting gravity change before and after the earthquake at the same month of each year can suppress the seasonal change, it is still affected by the long-term trend of the gravity signal over the study region. The biggest disadvantage of this method is in its deficiency on reducing random noise compared to the Heaviside step function method, which isolates coseismic signal using the Heaviside step function together with periodic functions from the gravity time series. Because based on the least-squares adjustment, the difference of two independent variables has a larger standard deviation than each of the variables; while for the Heaviside step function method, the estimated coseismic gravity change has a reduced standard deviation due to the smoothing effect over the long time series. *Wang et al.* [2012a, 2012b] have recently adopted a new method of utilizing Slepian functions [*Simons et al.*, 2006] to spatially localize GRACE data in the surrounding region of the earthquake. Similar techniques

were also applied to the coseismic gravity change and source parameter inversion in [*Cambiotti and Sabadini,* 2012]. The main benefit of this localization method is that the number of coefficients that approximately represent the signal over a targeted region is much less than the number of the global spherical harmonic coefficients, since the Slepian basis function is designed to have the majority of its energy optimally concentrated inside an arbitrarily defined region, that is, this method is intended to mitigate or reduce signal leakage. Nevertheless, the shortcoming of this method lies in the approximation, which makes it not a rigorous representation for the signal over the region. Here we choose to estimate the coseismic gravity change from the time series of monthly gravity disturbance calculated from the spherical harmonic coefficients over the earthquake region, similar to the method applied in [*Heki & Matsuto*, 2010; *Matsuo & Heki*, 2011], however, with improved processing without smoothing and decorrelations. Monthly geopotential solutions complete to degree 70 from CSR L2 Release 05 (RL05) NMAX 96 product are used to generate the disturbing potential by subtracting a reference model (GOCO02S with maximum degree up to 250), from January 2003 to September 2014. We choose to truncate the spherical harmonic coefficients to maximum degree 70 instead of the given maximum degree 96, based on the localized spectral analysis in the next section. For the available monthly solutions over ten years, we exclude the solutions for March 2011, January 2003, September 2004, and June 2012. The solution for March 2011 is excluded since it contains both the gravity signal before the earthquake and the signal after the earthquake. The other three extra excluded solutions are chosen based on their abnormal degree variance characteristics. As shown in Figure 3.1, the geoid residual degree variances for these three months are higher than those for the majority of the

solutions, especially for the degree range from 30 to 60, indicating their higher noise level.

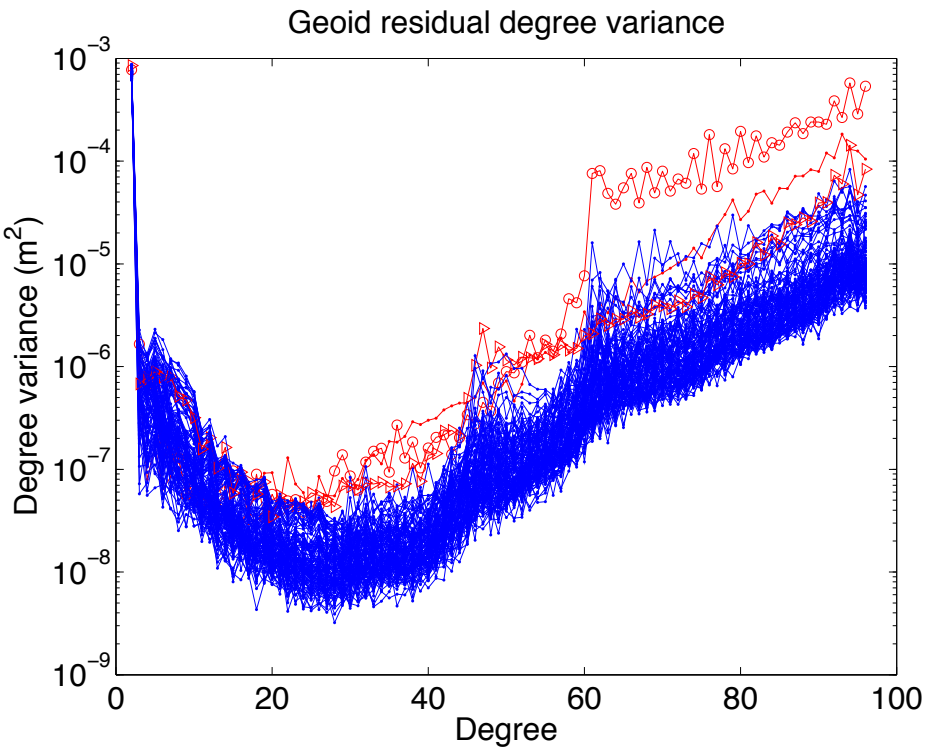

Figure 3.1. Geoid residual degree variance (relative to GOCO02S background model) for each monthly solution from January 2003 to July 2013 for the CSR RL05 NMAX 96 product.
The red dot line is for January 2003, the red circle line is for September 2004 (worst), the red triangle line is for June 2012, and the blue lines are for the other monthly solutions from January 2003 to July 2013.

We then establish a linear model to fit the time series of the gravity and gravity gradient disturbance over the 0.4° by 0.4° gridded study region, and conduct the least-squares adjustment. The linear fitting model is:

$$\begin{aligned} y = {} & a + b(t - t_m) + A_1 \times \cos\left(2\pi(t - t_m)/T_1\right) + B_1 \times \sin\left(2\pi(t - t_m)/T_1\right) \\ & + A_2 \times \cos\left(2\pi(t - t_m)/T_2\right) + B_2 \times \sin\left(2\pi(t - t_m)/T_2\right) \\ & + A_3 \times \cos\left(2\pi(t - t_m)/T_3\right) + B_3 \times \sin\left(2\pi(t - t_m)/T_3\right) + d \times H(t - t_{eq}) \end{aligned} \quad (3.1)$$

a the constant, μGal for gravity or mE for gravity gradient.
b the linear trend rate, μGal/year for gravity or mE/year for gravity gradient.
t_m the mean value of the all epochs, unit is year.
T_1 the annual period, year; T_1=1.
A_1 the annual amplitude of the cosine function, μGal for gravity or mE for gravity gradient.
B_1 the annual amplitude of the sine function, μGal for gravity or mE for gravity gradient.
T_2 the semiannual period, year; T_2 =0.5.
A_2 the semiannual amplitude of the cosine function, μGal for gravity or mE for gravity gradient.
B_2 the semiannual amplitude of the sine function, μGal for gravity or mE for gravity gradient.
T_3 the 161-days period, year.
A_3 the 161-days period amplitude of the cosine function, μGal for gravity or mE for gravity gradient.
B_3 the 161-days period amplitude of the sine function, μGal for gravity or mE for gravity gradient.
d the to-be-estimated coseismic jump, μGal for gravity or mE for gravity gradient changes.
t_{eq} the Tohoku-Oki earthquake epoch, year.
The Heaviside step function is defined as:

$$H(t - t_{eq}) = \begin{cases} 0 & t < t_{eq} \\ 0.5 & t = t_{eq} \\ 1 & t > t_{eq} \end{cases}$$

Figure 3.2 shows the gravity (*north* component or g_N, top) and gravity gradient (*Txz*, bottom) disturbance time series (blue lines) from January 2003 to September 2014 (excluding March 2011, January 2003, September 2004, June 2012) at a selected location (140.2°E 36.85°N). *Txz* represents the largest gravity gradient component. The

uncertainties (blue shading) are propagated based on the estimated *a posteriori* variance of unit weight for each coefficient. In order to isolate the earthquake seismic deformation signal, periodicities associated with the annual, semiannual, and the 161-day S_2 tidal aliasing periods [*Chen et al.,* 2009; *Wang et al.*, 2012b] are simultaneously fitted with a linear trend and the Heaviside step function for the jump at the earthquake epoch (equation 3.1) for each time series. The 161-day period is described in published studies as GRACE S_2 tidal aliasing or tidal errors manifested on the surface of the Earth observed by GRACE [e.g., *Chen et al.,* 2009; *Melachroinos et al.*, 2009; *Moore & King,* 2008; *King et al.,* 2011]. However, it is likely that the error originates from non-conservative forces. Here our approach is to estimate this error from GRACE seismic deformation time series. Figure 3.2 shows that the annual signal dominates both time series, while the two other periodical signals are slightly subordinate. g_N (Figure 3.2, top) decreases significantly at the earthquake epoch, with the estimated earthquake triggered jump as –24±3.9 μGal. For *Txz* (Figure 3.2 bottom), the estimated jump is also substantial at 1.98±0.41 milli-Eötvös (mE). We find that the approach using Heaviside step function can better reveal the seismic gravity and gravity gradient change compared to other methods, and the resulting retrieved signals are less contaminated by the long-term viscoelastic postseismic and other signals.

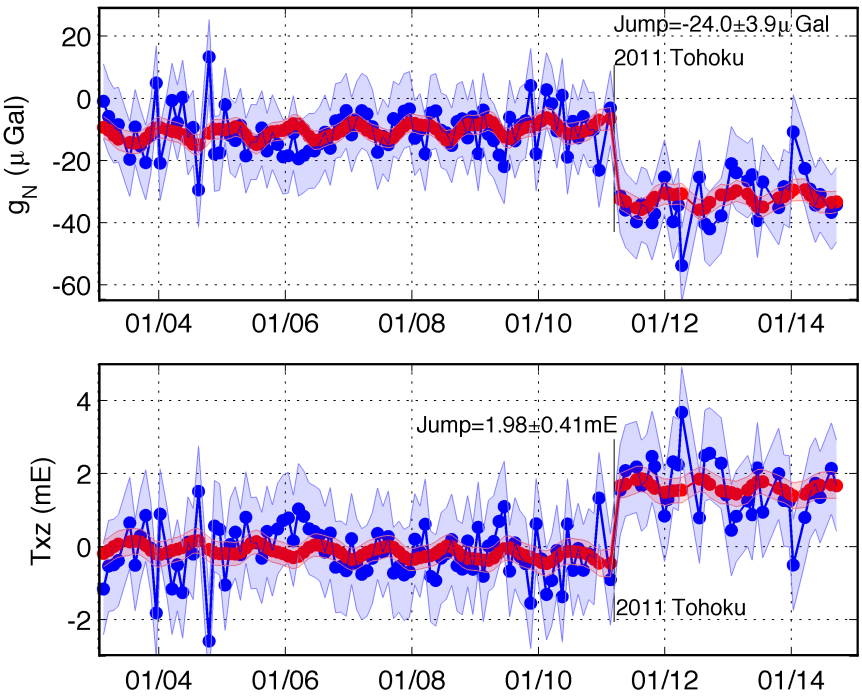

Figure 3.2. Time series of GRACE gravity and gravity gradient disturbances. Blue lines are the gravity disturbance g_N (top) and the gravity gradient disturbance *Txz* (bottom) at 140.2°E 36.85°N, generated from 131 monthly CSR RL05 NMAX 96 solutions up to degree 70 from January 2003 to September 2014. The uncertainties (blue shadings) are propagated based on the estimated *a posteriori* variance of unit weight for each coefficient. The red lines represent the model fits using equation (3.1) including the estimated jumps at the earthquake occurrence.

The direct estimation of the coseismic signal change at the earthquake epoch using the Heaviside step function together with other periodic and linear terms has many advantages compared to other methods. It can better reveal the coseismic signal change without being contaminated by the long term post-seismic signal, at least separate the post-seismic signals after the earthquake month, although it is still affected by the pre-shocks and after shocks within the earthquake month. This method reduces the standard deviation of the coseismic jump compared to the method of subtracting signal of the same month of each year before and after the earthquake. Moreover, the gravity change over

the study region strictly represents the regional signal, as compared to the localization method based on Slepian functions.

3.2 Localized spectral analysis

In this section, we show the benefits of the localized spectral analysis as an efficient method to evaluate the noise level of each component of gravity and gravity gradient change and to guide the practical degree truncation that gives good signal-to-noise ratio. To estimate the localized spectrum of the earthquake-induced gravity and gravity gradient changes, we first compute the gravity and gravity gradient change up to maximum degree 96 for the CSR RL05 NMAX 96 product over the fault region using the Heaviside step function described above. Then we carry out the localized spectral estimates as presented in [*Wieczorek & Simons*, 2005] using Slepian tapering windows centered at the 2011 Tohoku earthquake centroid.

One important benefit of this localized spectral analysis is that it can evaluate the signal and noise level of each component of gravity and gravity gradient as a function of spherical harmonic degree. Assuming the degree variance for the model-predicted gravity and gravity gradient change are the true signal, we can see that both gravity and gravity gradient change induced by earthquakes have higher power for the higher degrees. It's worth mentioning that the dropping of the degree variance staring from degree 81 for the model predicted value does not represent the actual decrease of the degree variance, rather it is the artifacts caused by the localized spectral analysis, which is not reliable for the degrees from $NMAX - L_h$ to $NMAX$ [*Wieczorek and Simons*, 2005], where L_h is the maximum degree, 15, of the Slepian window function. From Figure 3.3, we can see that the GRACE-observed g_N change agrees well with the model prediction up until around

degree 70, although the amplitude is slightly larger than the model prediction. While, the degree variance for GRACE-observed g_E and g_D change (Figure 3.3) increases sharply starting from degrees at around 40, indicating that degrees higher than that are dominated by noise. This demonstrates that north component of gravity contain reliable signal up to much higher degree than the east and down component of gravity change. Same for the gravity gradient change, the north component of GRACE-observed gravity gradient change is showing good consistency with the model prediction until around degree 70. Above degree 70, the GRACE data is much higher than the model prediction, which we interpret as noise. We also notice that *Txy* are noiser compared to *Txx*, *Txz* for degrees between 60 and 70, which might be caused by the term T_λ (partial derivative of *T* with respect to longitude), contaminated by the south-north stripes. One other important application of this localized spectra analysis is that it is an efficient method to guide the choice of practical degree truncation. As shown in Figure 3.3, the degree variance for g_N change keeps in good agreement with the model prediction until around degree 70, based on which, we can choose to discard the spherical harmonic coefficients above degree 70.

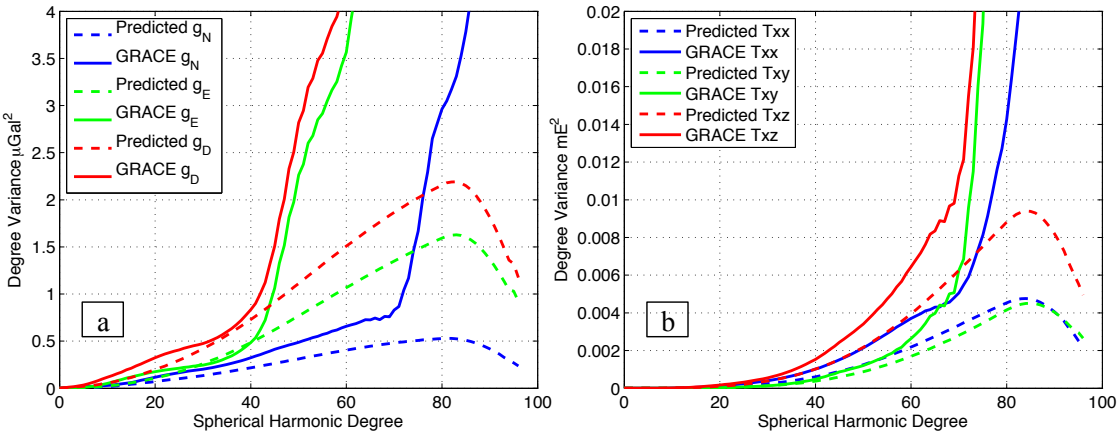

Figure 3.3. Comparison in the spectral domain.
The localized degree variance as a function of spherical harmonic degree is shown for the observed and model-predicted g_N, g_E, g_D change (a), and *Txx*, *Txy*, *Txz* change (b).

3.3 North component of gravity and gravity gradient change

As shown in the localized spectral analysis, the north component of gravity change from GRACE data contained much higher degree signals compared to the east and down component of gravity. Hence, we use only the north component of gravity and gravity gradient changes from GRACE data to isolate large undersea earthquakes, with no decorrelation or spatial filtering of the GRACE data, leading to *improved* spatial resolution to the extent possible. We demonstrate the advantage of these components to reduce *south-north stripes* and preserve high-degree signal in GRACE L2 products.

For GRACE L2 data post-processing, de-striping or decorrection technique is widely used to remove or reduce the high-frequency correlated errors in GRACE temporal gravity field solutions [e.g., *Swenson and Wahr*, 2006, *Duan et al.,* 2009]. However, the de-correlation process may partially eliminate the seismic gravity change signal [*Wang et al.*, 2012a, 2012c] and/or alter the orientation of the spatial pattern, which is the key observation to constrain the dislocation vector orientation. Although Gaussian smoothing

can reduce the ripple effects caused by the band-limited L2 solution, as a low-pass filter it also could smooth out or diminish the desired earthquake-induced high frequency signal. As shown in the next section, our approach using the north component of gravity and the corresponding gravity gradient change can effectively reduce the contamination by the north-south stripes; hence it can better preserve the seismic signal by avoiding the negative effect from de-striping and Gaussian smoothing.

The GRACE-observed and model-predicted gravity and gravity gradient changes corresponding to the 2011 Tohoku earthquake are compared with a resolution commensurate with the GRACE observations. For the GRACE-derived g_N change (Figure 3.5a) up to degree 70, the positive-negative-positive pattern is evident and agrees well with model predictions (Figure 3.5d). The GRACE-observed g_N change is substantial and reaches –24.0 ± 3.9 μGal at 140.2°E 36.85°N (Figure 3.5a), with the magnitude slightly greater than the model prediction, –18.5 μGal. It is evident that larger stripes exist in the GRACE-derived g_E, g_D changes. For the g_E change, although the negative-positive-negative pattern centered over the Tohoku region (Figure 3.5b) is visibly similar to the model prediction (Figure 3.5e), the surrounding error is too large to clearly distinguish the seismic induced signal. Analogous to the g_E change, the surrounding error for the g_D change (Figure 3.5c) is also too large. From the GRACE observation, the north-south stripes occur in g_E, g_D changes, because the KBR measurement is highly sensitive to g_N change but relatively insensitive to g_E, g_D changes. The reason is that the GRACE-measured range-acceleration is linearly related (equation 3.2) to the gravitational force differences projected at the line-of-sight (LOS) direction,

which is the north south direction because of the near-90^0 orbital inclination. This linear relationship is:

$$\ddot{\rho}_{12} = \vec{g}_{12}^{\,i} \cdot \vec{e}_{12}^{\,i} + (\vec{a}_2^{\,i} - \vec{a}_1^{\,i}) \cdot \vec{e}_{12}^{\,i} + (\left|\dot{\vec{r}}_{12}^{\,i}\right|^2 - \dot{\rho}_{12}^2) / \rho_{12} \tag{3.2}$$

where ρ_{12}, $\dot{\rho}_{12}$, $\ddot{\rho}_{12}$ are the inter-satellite range, range rate, and range acceleration respectively. $\vec{g}_{12}^{\,i}$ is the difference between the gravitational force on the satellite 2 and satellite 1. $\vec{e}_{12}^{\,i}$ is the unit line-of-sight position vector. $\vec{a}_1^{\,i}$ and $\vec{a}_2^{\,i}$ are the non-gravitational forces on the satellite 1 and satellite 2, respectively. $\vec{r}_{12}^{\,i}$ is the relative position vector of satellite 2 with respective to satellite 1 in the inertial frame.

For the LOS gravitational difference, $\vec{g}_{12}^{\,i} \cdot \vec{e}_{12}^{\,i}$, we have $\vec{g}_{12}^{\,i} \cdot \vec{e}_{12}^{\,i} = (C_{i,2}^n \vec{e}_{12}^{\,i}) \cdot \vec{g}_2^{\,n} - (C_{i,1}^n \vec{e}_{12}^{\,i}) \cdot \vec{g}_1^{\,n}$. where $C_{i,2}^n$ is the transformation matrix from the north-east-down frame to the inertial frame for satellite 2, and $C_{i,1}^n$ is the transformation matrix for satellite 1. $\vec{g}_2^{\,n}$ is the gravitational vector in the north-east-down frame at the position of satellite 2, and $\vec{g}_1^{\,n}$ is the gravitational vector in the north-east-down frame at the position of satellite 1.

As shown in Figure 3.4 (*right*), the down component of the line-of-sight direction projection vector (the unit LOS position vector), $C_{i,2}^n \vec{e}_{12}^{\,i}$ is small globally, around 0.015. And the east component (Figure 3.4 *middle*) is also small, below 0.044 for latitude within 60 degree, but increases to almost one near two poles due to the orbit configuration of GRACE satellites. Nevertheless, the absolute value of the north component of this position vector (Figure 3.4 *left*) is around one, but drops to almost zero near the poles. Hence, we can see that the line-of-sight direction projection factor, $C_{i,2}^n \vec{e}_{12}^{\,i}$, for east and down component of gravitational force is about two orders of magnitude smaller than that

for the north component of gravitation globally (Figure 3.4) excluding the polar regions. Therefore, the GRACE KBR measurement is about two orders of magnitude less sensitive to the g_E, g_D change signals than to the g_N change signal. In another word, the GRACE-measured range change is mainly driven by the north component of gravity change.

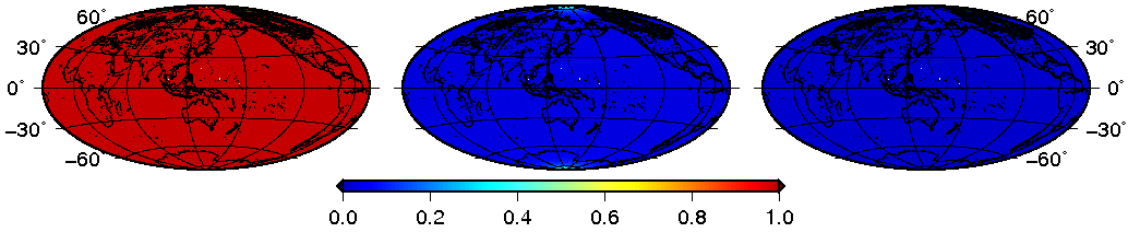

Figure 3.4. The absolute value of the north (*left*), east (*middle*), down (*right*) components of the LOS position vector $C_{i,2}^{n}\vec{e}_{12}^{i}$. The plot is for GRACE satellite 1 in March 2011.

Theoretically speaking, since $g_N = -\partial T / \partial \theta / r$, the g_N change obviously has diminished north-south stripes where the disturbing potential is differentiated along the meridian direction. This is the same for the gravity gradient observables, of which only north-associated components have reduced stripes or correlated errors. The other three components, *Tyy*, *Tyz*, *Tzz*, like g_E, g_D, are basically contaminated by high-frequency correlated error, which is twice of that for the *Txx*, *Txy*, *Txz* components. As first mentioned by *Wang et al.* [2012c], the gravity gradient, *Txx*, dominated by the $T_{\theta\theta}$ term, is less influenced by the south-north stripes. For the *Txz*, the north-south stripes are reduced by T_{θ} and $T_{r\theta}$ terms. Although *Txy* include the T_{λ} term, the dominating term $T_{\theta\lambda}$ helps to diminish the north-south stripes. In conclusion, the gravity and gravity gradient components that are dominated by the derivative of disturbing potential with respect to

the colatitude are much less influenced by the north-south stripes representing high-frequency errors in the current GRACE data products.

The comparison between GRACE-observed and model-predicted gravity gradient change is shown in Figure 3.6. For the *Txx* change (Figure 3.6a), the main negative-positive-negative-positive pattern distributed from Sea of Japan to southeast coast of Kanto matches well with the model prediction (Figure 3.6d). For the *Txy* change (Figure 3.6b), the main negative-positive pattern is also similar with the prediction (Figure 3.6e), even with the analogous '8' shape positive pattern. The *Txz* change (Figure 3.6c) matches the prediction as well, with the maximum change of 2.0±0.4 mE at 140.2°E, 36.95°N, slightly larger than the prediction, 1.5 mE.

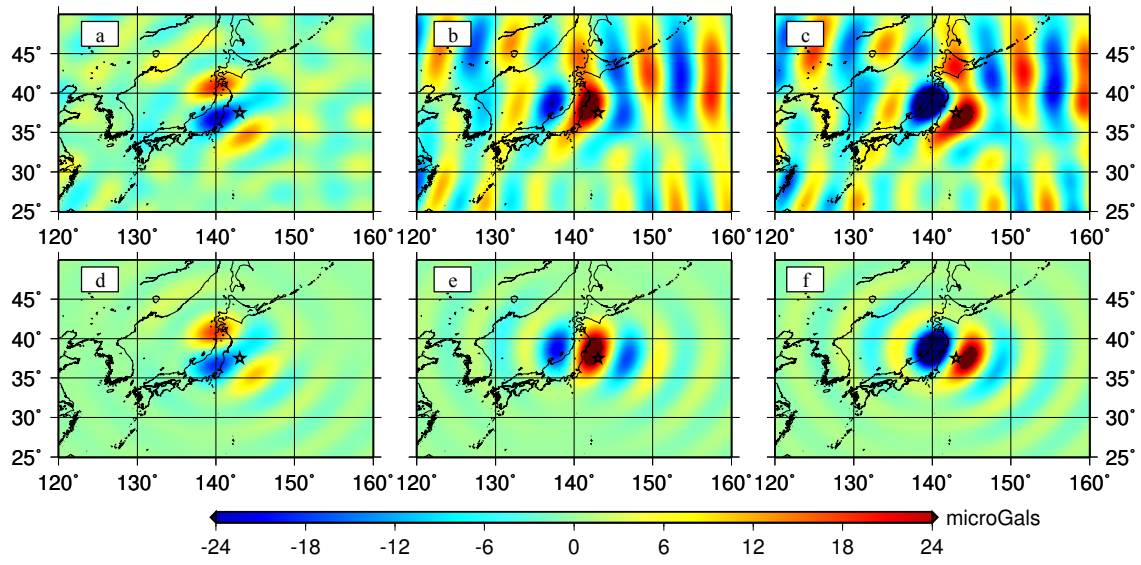

Figure 3.5. Comparison of GRACE-observed and model-predicted coseismic and postseismic (March 2011) gravity changes up to degree 70 from CSR RL05 NMAX 96 product.
(a) ~ (c): GRACE-observed g_N (a), g_E (b), g_D (c) change, respectively. (d) ~ (f): model-predicted g_N (d), g_E (e), g_D (f) change, respectively. The black star is the Global Centroid Moment Tensor Project (GCMT) centroid (143.05°E, 37.52°N) (http://earthquake.usgs.gov/earthquakes/eqinthenews/2011/usc0001xgp/neic_c0001xgp_gcmt.php).

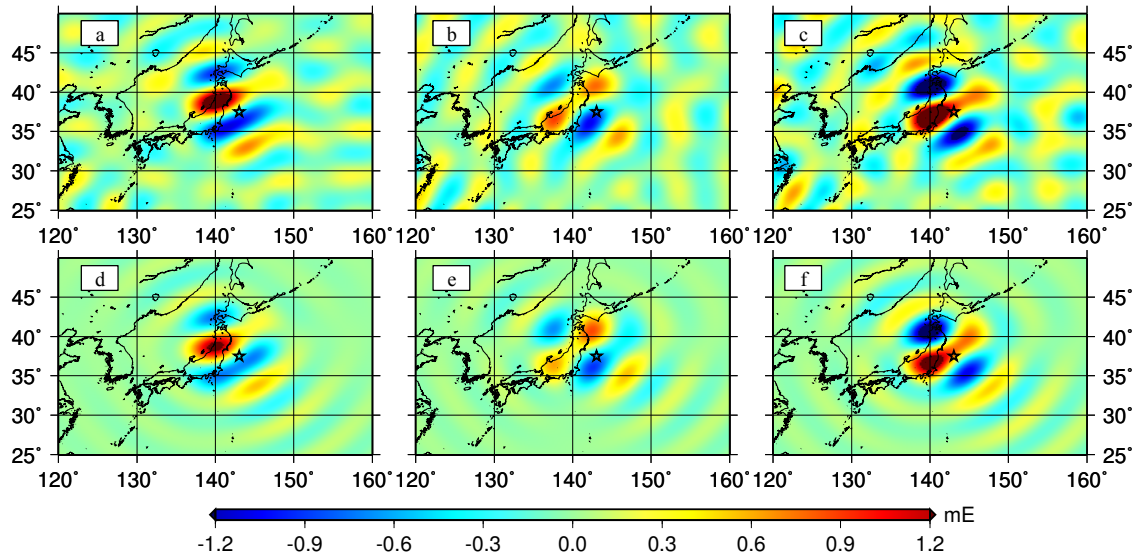

Figure 3.6. Comparison of GRACE-produced and model-predicted gravity gradient change up to degree 70 from CSR RL05 NMAX 96 product.
(a) ~ (c): GRACE-produced *Txx* (a), *Txy* (b), *Txz* (c) change. (d) ~ (f): seismic-model-predicted *Txx* (d), *Txy* (e), *Txz* (f) change. Other descriptions are the same as in Figure 3.5.

Chapter 4. Inversion for Source Parameters

4.1 Inversion for finite fault model with the Simulated Annealing algorithm

This section solves for the finite fault parameters from GRACE data using the simulated annealing algorithm as discussed below. Instead of assuming the source as a point source, here we use a uniform distributed slip model to represent the focal mechanism. We first briefly introduce the simulated annealing algorithm, and then apply this inversion scheme to solve for the source parameters of the 2011 Tohoku earthquake.

4.1.1 Simulated Annealing algorithm

The Simulated Annealing (SA) algorithm [*Kirkpatrick et al.*, 1983; *Goffe et al.*, 1994] is an optimization technique developed to find a global optimum via a procedure analogous to the process of chemical annealing. It is based on the Metropolis-Hastings algorithm, which is a kind of Markov Chain Monte Carlo algorithm designed to generate a sequence of random samples from a target probability distribution [*Wang*, 2012]. The core of the SA algorithm is to sample the Gibbs-Boltzmann distribution, which describes the expected fluctuations of a system's state at a certain temperature. This Gibbs-Boltzmann distribution is generally difficult to be explicitly expressed. Therefore, the Metropolis-Hastings algorithm is used to generate a sequence of samples for approximation.

For the finite model inversion using GRACE data, the goal of the optimization is to find the source parameters that give a minimum model-data misfit. For each trail of source parameters, the forward model-predicted gravity and gravity gradient change are

calculated and compared with the GRACE-derived g_N, *Txx*, *Txy*, and *Txz* change. So, the target function to be minimized is the mean of the relative difference (equation 2.17) for g_N, *Txx*, *Txy*, and *Txz*:

$$\Phi(X) = \left(rd_{g_N} + rd_{T_{xx}} + rd_{T_{xy}} + rd_{T_{xz}} \right) / 4$$

where, X is the vector of to-be-determined parameters, $X = [lat, lon, L, W, S]^T$. *lat, lon, L, W, S* are the latitude, longitude, fault length, width, uniform slip of the finite fault model, respectively. The number of parameters, m, is 5 here.

The SA algorithm procedure is briefly described here. Starting with a given initial temperature, T_0, which is a control parameter, the algorithm generates a group of random vector X within the given upper and lower boundaries. For each random vector X, the forward modeling of the gravity and gravity gradient change corresponding to this fault model are calculated, leading to a value for the target function $\Phi(X)$. If the $\Phi(X)$ is smaller than the previous target function, then the new vector X is accepted. Otherwise, the Metropolis acceptance ratio [*Uzun*, 2013], which depends on the difference of the two target functions and the current temperature, is used as a criterion to accept or reject this new vector X. The next trial of vector X is computed as $X = X_{pre} + r \times V$, where X_{pre} is the previous accepted parameter vector, r is a uniform-distributed random number, and V is the step length vector. The above acceptance-perturbation steps are repeated for $N_S \times m$ times, where N_S is a predefined integer. After that, the step length vector is adjusted according to the ratio of the count of the accepted trails over the count of the rejected trails from the last $N_S \times m$ iterations. This adjustment to the step length vector is repeated for N_T times for the given temperature, where N_T is a predefined integer. Then the temperature is reduced to be $r_T \times T_0$, where r_T is the temperature reduction parameter. This

iteration is repeated until the target function, $\Phi(X)$, dose not change for the last several temperatures.

To get a reliable solution, *Corana et al.* [1987] suggested the following values of the parameters: N_S to be 20, N_T to be the maximum of (100, 5m), and the temperature reduction parameter r_T to be 0.85. The essential parameters for minimizing the target function are the initial temperature T_0, the starting values of parameters, X, and the step length V for X. As pointed out by *Goffe et al.* [1994], the appropriate choice of the initial temperature is important. Because if the initial temperature is too low, the step length would be too small, which might miss the search area containing the global minimum. The method in [*Goffe et al.*, 1994] is a good way to find T_0. First set T_0 to be 10^7 and the temperature reduction parameter, r_T, to be 0.01, and then find the temperature at which the step length begins to decrease as the initial temperature. At each temperature, the step length is chosen correctly if fifty percent of the total evaluations are accepted [*Goffe et al.*, 1994], and that the number of rejected trials may not be excessively more than half of total trials. To further gain confidence on the reliability of the solution, different starting values can be tried to see whether they can produce the same global minimum.

4.1.2 The 2011 Tohoku earthquake

The 11 March 2011 Mw 9.0 Tohoku earthquake ruptured the Okhotsk-Pacific interplate boundary of east Japan offshore up to about 40 m, with a fault area as large as 500×200 km^2 [e.g. *Ammon* et al., 2011; *Ozawa et al.*, 2011; *Simons et al.*, 2011]. Large postseismic slips [*Ozawa et al.*, 2011] occurred with a moment of about 10% of the main shock. Several coseismic slip distribution models were determined using seismic data [*Hayes et al.*, 2011; *Lay et al.*, 2011; *Shao et al.*, 2011], Global Positioning System (GPS) observed

surface displacement data [*Ozawa et al.*, 2011; *Pollitz et al.*, 2011b], combined seismic and GPS data [*Wei et al.*, 2012; *Ammon et al.*, 2011], and combined seismic, GPS and tsunami data [*Simons et al.*, 2011]. However, the estimated location and depth of the average slip differ significantly. Geodetic inversions give the average slip down-dip [*Ozawa et al.*, 2011; *Simons et al.*, 2011; *Ammon et al.*, 2011] of the GCMT hypocenter (20 km depth) closer to land. Seismic inversions tend to give the average slip up-dip [*Shao et al.*, 2011; *Hayes et al.*, 2011; *Wei et al.*, 2012], or even shallower near trench [*Lay et al.*, 2011]. In this section, we show the independent constraint on seismic moment, fault width, rake angle, and centroid location from GRACE data through the innovative method of using only the north component of gravity and gravity gradient change [*Dai et al.,* 2014]. We show that the estimated slip orientation and centroid location are different from GPS/seismic solutions and potentially due to the additional offshore constraint from GRACE data [*Dai et al.,* 2014].

Adopting the GRACE data processing method described in Section 3, we analyze the GRACE L2 products by the Univ. of Texas Center for Space Research (CSR), GFZ German Research Centre for Geosciences, and Jet Propulsion Laboratory (JPL) from January 2004 to February 2013. And we choose to present the results using the CSR L2 data products. We first conduct an analysis of the gravity and gravity gradient disturbance time series over the 0.4° by 0.4° gridded study region using the fitting model (equation 3.1), as shown in Figure 4.1. North component of gravity, g_N (Figure 4.1, top) decreases significantly at the earthquake epoch, with the estimated earthquake triggered jump as –17.6±1.1 μGal. For *Txz* (Figure 4.1 bottom), the estimated jump is also substantial at 1.25±0.09 mEötvös (mE).

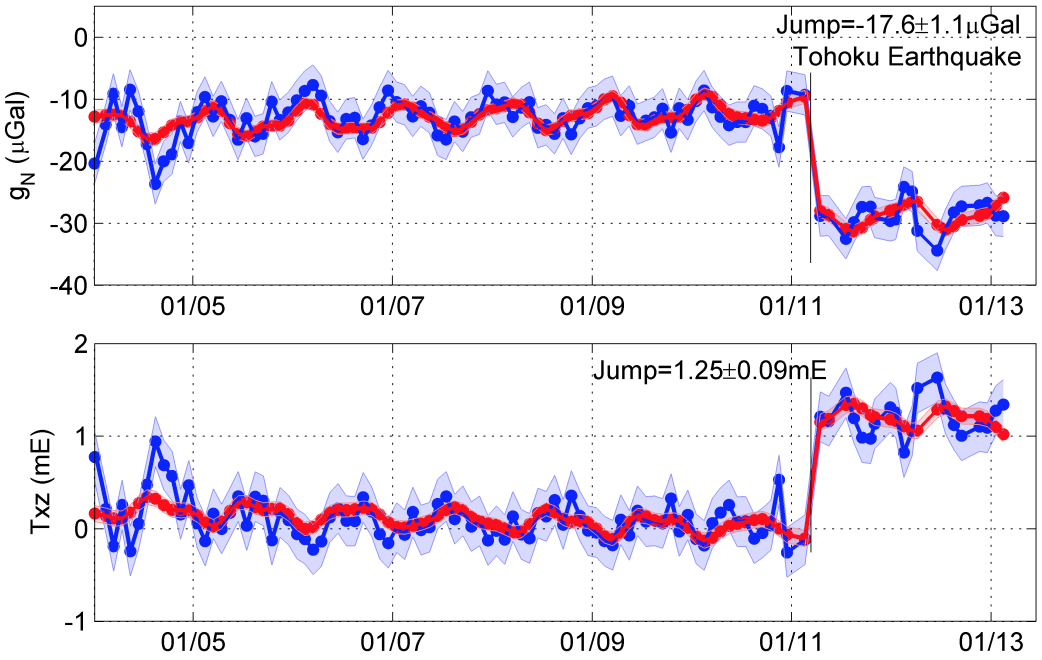

Figure 4.1. Time series of GRACE gravity and gravity gradient disturbances. Blue lines are the CSR RL05 derived gravity disturbance g_N (top) and the gravity gradient disturbance *Txz* (bottom) at the location of apparent maxima (139.6°E, 36.4°N, corresponding to white circles in Figure 4.2a and Figure 4.3c). The uncertainties (blue shadings) are propagated based on the estimated *a posteriori* variance of unit weight for each coefficient. The red lines represent the model fits using equation (3.1) including the estimated jumps at the earthquake occurrence.

As described in section 2.2.1, the coseismic slip distribution model generated using teleseismic body waves and near source GPS observations [*Wei et al.*, 2012], and the postseismic slip distribution model produced using GPS displacement data for 12–25 March 2011 [*Ozawa et al.,* 2011] are adopted to model the gravity and gravity gradient changes. The north component of gravity and gravity gradient change at the Earth's surface due to both solid Earth deformation and the passive response of ocean water is computed up to spherical harmonic degree 60 (Figure 4.2 d ~ f) to be consistent with

GRACE solution. The comparison in both spatial domain and spectral domain for model-predicted and GRACE-derived gravity and gravity gradient change are presented below. For the GRACE-derived g_N change (Figure 4.2a), the positive-negative-positive pattern is evident and agrees well with model predictions (Figure 4.2d). The GRACE-observed g_N change reaches –17.6±1.1 μGal at 139.6°E, 36.4°N (Figure 4.2a), with the magnitude slightly greater than the model prediction, –13.6 μGal. The profile along 140.4°E (Figure 4.4a) also shows good agreement between observed and model predicted g_N, with GRACE-observed magnitude slightly larger than the prediction. By detailed comparison, the spatial patterns of the GRACE observed g_N (Figure 4.2a) is found to be at an orientation of about 10° clockwise of the model predicted g_N orientation (Figure 4.2d), which implies that a different slip vector direction (e.g. rake angle) is preferred by GRACE data. The GRACE-observed gravity gradient change is shown to have good consistency with the model prediction in Figure 4.3. The *Txx* change (Figure 4.3a) matches well with the model prediction (Figure 4.3d), as well as the *Txy* change (Figure 4.3b). The *Txz* change (Figure 4.3c) has the maximum change of 1.25±0.09 mE at 139.6°E, 36.4°N, slightly larger than the prediction, 0.95 mE. Coincide with the orientation of the spatial pattern of g_N in Figure 4.2a, GRACE observed gravity gradient change (Figure 4.3) precedes about 10° clockwise of the model predicted g_N orientation.

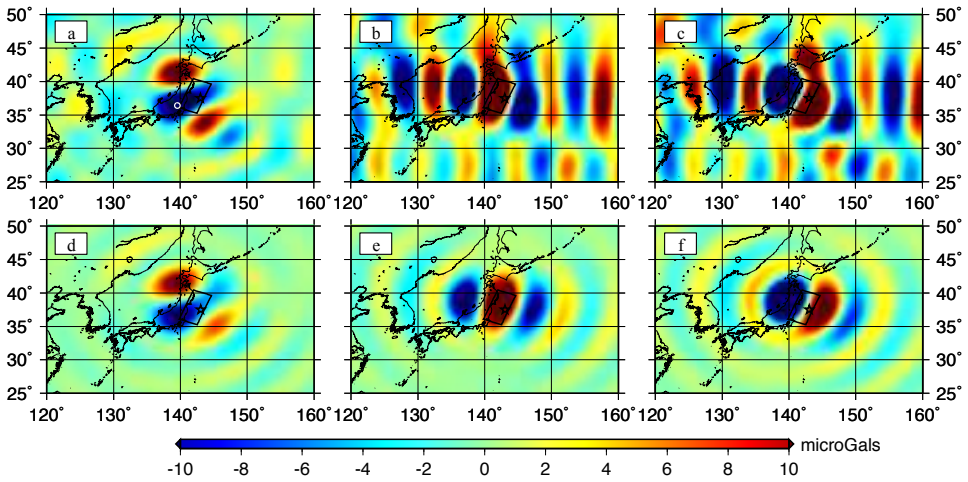

Figure 4.2. Comparison of GRACE-observed and model-predicted coseismic and postseismic (March 2011) gravity changes.
(a)~(c): GRACE-observed g_N (a), g_E (b), g_D (c) change, respectively. (d)~(f): Coseismic and postseismic model predicted g_N (d), g_E (e), g_D (f) change, respectively. The uncertainties for observed g_N, g_E, g_D change are approximately 1.2, 2.5, 2.8 μGal, respectively. The white circle is the location of maxima to show the time series in Figure 4.1. The black rectangle is the coseismic fault plane boundary, and the black star is the GCMT centroid.

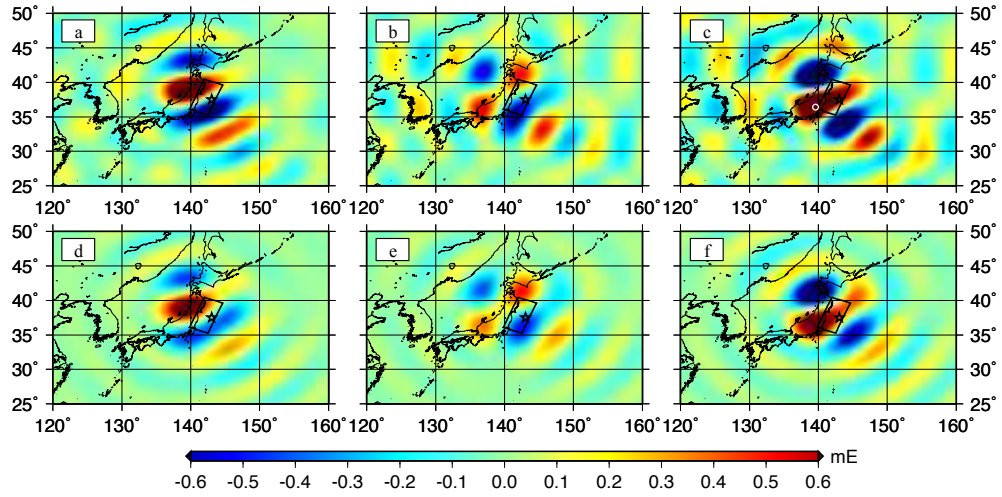

Figure 4.3. Comparison of GRACE-produced and model-predicted gravity gradient change.
(a)~(c): GRACE-produced *Txx* (a), *Txy* (b), *Txz* (c) change. (d)~(f): Coseismic and postseismic model predicted gravity gradient change: *Txx* (d), *Txy* (e), *Txz* (f). Other descriptions are the same as in Figure 4.2.

Figure 4.4b presents the percentage of the degree variance of the observed and model-predicted g_N, *Txx*, *Txy*, *Txz* changes in the study region, showing the consistency between the observed and the model-predicted values. It shows that both gravity and the corresponding gravity gradient changes are dominated by the higher degree signals. Consistent with *Wang et al.*'s [2012c] conclusion for the 2004 Sumatra-Andaman earthquake, Figure 4.4b validates that gravity gradient changes have relatively high power for degrees above 42, about 25% greater than the g_N change. Although gravity gradient can enhance the high frequency details, they are noisier, as demonstrated by their unexpected higher power compared the model prediction for degrees above 48, especially for *Txy*.

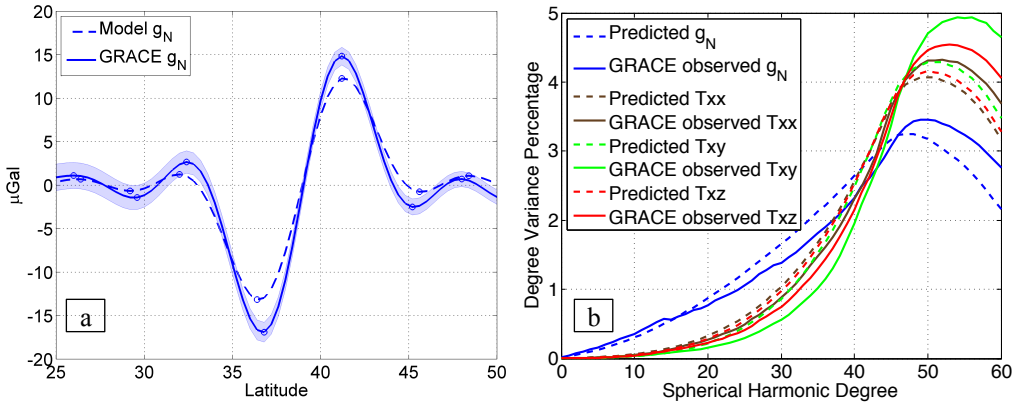

Figure 4.4. Comparison in the spectral domain and along a profile.
(a): Model-predicted and GRACE-observed north component of gravity change g_N along the profile of 140.4°E. Shading denotes the estimated standard deviation; (b): Percentage of the degree variance as a function of spherical harmonic degree, for observed and model predicted north component of gravity change, g_N, and the corresponding gravity gradient changes, *Txx*, *Txy*, and *Txz*.

The sensitivity of GRACE-observed north components of gravity and its corresponding gravity gradient changes to seven fault parameters has been demonstrated by numerous synthetic scenarios (Figures 2.5–2.9). It shows that the spatial orientation of gravity and gravity gradient change rotates in the same direction as either strike or rake angle changes, agreeing with *Han et al.*'s [2011] conclusion that there is a monotonic relationship between gravity change pattern and strike and rake angles for fault with small dip angle. Since the strike angle is well constrained by other kinds of data, such as the orientation of the aftershocks area, and the plate boundary direction, we fixed the strike angle during our inversion. As a result, the rake angle can be effectively constrained by GRACE observations. In addition, the dislocation magnitude and fault width are highly sensitive to the gravity signal. Since there is a trade-off between the fault width, dip angle and fault depth, and as the GRACE-observed signal is least sensitive to

fault depth and most sensitive to fault width, the fault width can be resolved during the inversion while fixing the fault dip angle and depth (Table 4.1).

Using the simulated annealing algorithm [*Kirkpatrick et al.*, 1983; *Goffe et al.*, 1994] and an approach similar to [*Wang et al.*, 2012a] but for a different earthquake, the rake angle, fault location, width, and uniform or average slip magnitude have been resolved with strike angle fixed at 201°, fault dip angle fixed at 10°, and the depth of the top edge of the fault fixed to be at the seafloor. The inversion procedure is to search for the optimal fault parameters that give the minimum relative differences (equation 2.16~2.17), which are the root-mean-square (RMS) of data-model differences divided by RMS of GRACE data. Our inverted uniform slip fault model improves the relative differences with GRACE CSR observation by about 20% as compared with the slip model inverted using GPS and seismic data by *Wei et al.* [2012] and *Ozawa et al.* [2011]. During the inversion, the rake angle quickly converged to its optimal value at 77.0°±2° (Table 4.1). We define the solution uncertainty by using the range (Figure 4.5), which produces no more than 0.1% of the relative differences (equation 2.16), as compared to the optimal solution during the inversion. The GRACE inverted rake angle is about 10° smaller than most of the published estimates. The smaller rake angle indicates that the azimuth of the slip vector (equation 4.1) is about 10° larger than some of the published solutions (Table 4.1) and it is about 5° larger than the published USGS CMT solution (http://earthquake.usgs.gov/earthquakes/eqinthenews/2011/usc0001xgp/neic_c0001xgp_cmt.php), which gives the smaller rake angle than our solution but has a correspondingly small strike angle. The different orientation of our estimated slip model can be explained by the spatial orientation of the observed gravity and gravity gradient changes, which is about 10°

clockwise from the model prediction. The slip vector azimuth (β) is defined as the azimuth of slip vector projected to horizon, positive clockwise from North. Given strike, ϕ, rake λ, dip δ, we have:

$$\beta = \phi - \arctan\left(\sin\lambda\cos\delta / \cos\lambda\right) \approx \phi - \lambda \tag{4.1}$$

The approximation holds when dip angle is small.

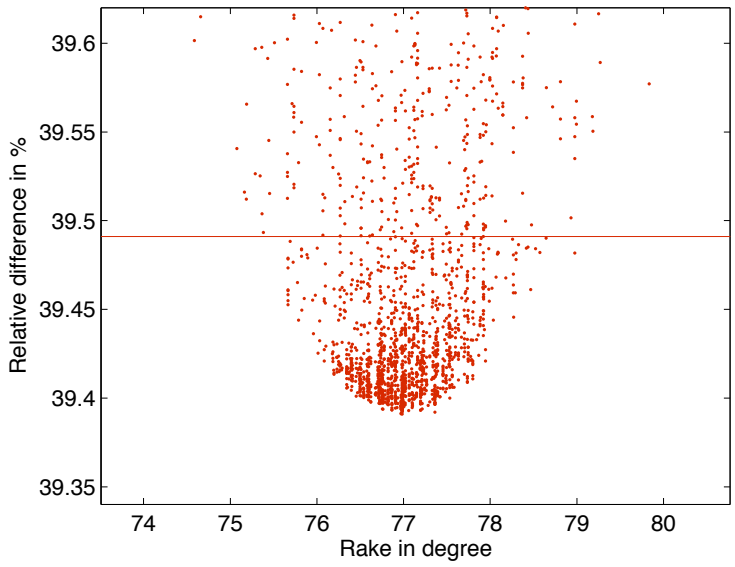

Figure 4.5. Solution uncertainty for rake angle.
Each red dot is a trial of rake angle, fault length, width, slip, and location during inversion. The minimum relative difference would give the optimal solution, which is 77° for rake angle as shown. The red horizontal line is corresponding to 0.1 plus the minimum relative difference. In this figure, the rake angle range [75, 79] can give relative differences lower than the red line. This range is defined as solution uncertainty.

The centroid location is well resolved to be at 142.17±0.05°E, 37.53±0.08°N, shown as a red star in Figure 4.6. As it is well-known, seismic data tend to yield average slip near trench, e.g., the blue contour and blue star [*Wei et al.*, 2012] (Figure 4.6), and GPS data infer a average slip closer to land, as shown by the magenta contour and magenta star (Figure 4.6) [O*zawa et al.*, 2011]. GRACE data resolved location is in-between these two

other solutions in the west-east direction. Although our solution is about 40 km south of the solutions in [*Wei et al.*, 2012] and [O*zawa et al.*, 2011], it centers at the same latitude as the GCMT centroid, and it is 30 km west of the USGS CMT solution. The GRACE-estimated centroid depth (12 km) is relatively smaller than other published values, partially due to the inversion scheme, which fixed the top edge of the fault at the seafloor. The seismic moment converges to its optimal solution well, which is $(6.43\pm0.4)\times10^{22}$ N m (Table 4.1), corresponding to a Mw value of 9.14±0.02, which is larger than estimates of other slip models (Table 4.1), and can be explained by the larger gravity magnitude as observed by GRACE, considering that the GRACE solution contain the afterslip information in March 2011. Estimated fault width is 70±20 km using GRACE data. However, the resolved fault length has large deviations to make relative difference close to its minimum, which is 240±110 km, indicating that, as discussed before, the fault length is relatively hard to be constrained by GRACE data. Since length, width and slip together determine the signal magnitude, the small width indicates a large slip and the larger deviation in length leads to a larger uncertainty for estimated average slip, which is 127±100 m.

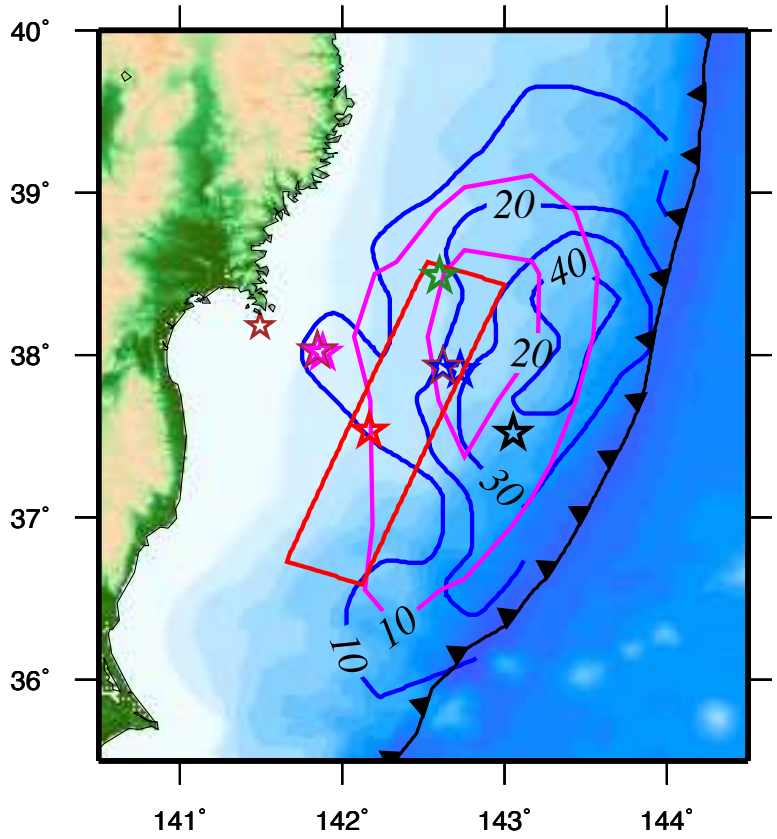

Figure 4.6. Comparison of slip distribution models.
The **black** triangle line is the plate boundary [*Bird*, 2003]. The **black** and green stars are the GCMT and USGS CMT estimated Centroid locations, respectively. The brown star is the centroid location of postseismic slip model [*Ozawa et al.*, 2011]. The slip contours (m) are from the published coseismic slip models: GPS-only model in magenta [*Ozawa et al.*, 2011] and GPS/seismic model in blue [*Wei et al.*, 2012]. The centroid location of these two slip models are denoted as blue and magenta stars, which are outlined with brown color when combined with the postseismic slip model. The contribution of the postseismic slip to centroid location is negligible as shown that the magenta star and the magenta star with brown outline are almost at the same location. The red star is estimated centroid location with the red rectangle as fault boundary using the GRACE CSR data, which is about 40 km south and 40 km west of the centroid location (blue star) by *Wei et al.* [2012].

Model	Data Source	Centroid		Rake angle (°)	Strike angle (°)	Dip (°)	Slip azimuth (°)	M_0 in 10^{22} Nm
		Location	Depth	Ave	Ave	Ave		
Ozawa et al. [2011]	GPS	Magenta star	50 km	87	196	11	109	3.43
Wei et al. [2012]	GPS and Seismic data	Blue star	18 km	89	201*	10*	112	5.31*
GCMT	Long-period mantle waves	**Black star**	20 km	88	203	10	115	5.31
USGS CMT	Seismic data	Green star	10 km	68	187	14	120	4.50
Han et al. [2011]	GRACE Level 1b data	-	17 km	82	196*	10.5	114	5.40
This study	GRACE CSR RL05 data	Red star	12 km	77.0±2	201*	10*	124	6.43± 0.4
This study	CSR RL05 N96	Red beach ball (Fig. 4.15)	16 km	113±0.5	236±0.5	12±0.1	123	4.03± 0.01

Table 4.1. Comparison of Fault Parameters.
*Parameter fixed during inversion.

GRACE observed coseismic gravity change is at much coarser resolution than other geodetic data, namely, GPS or synthetic aperture radar interferometry measured land displacement. However, GRACE directly observes right above the fault area of the March 2011 Tohoku undersea earthquake, providing a better spatial coverage. Here we further illustrate that GRACE observation provides independent constraints on the earthquake source parameters complementary to the on-land GPS and seismic data. Using both onshore and offshore GPS/Acoustic Network data, *Wang et al.* [2013] obtained a slip model (Model 1) with the maximum slip of ~ 48 m at (38.13°N, 143.26°E, 15.5 km), rake 74° at the peak slip, and an average rake of 80°. Using only the onshore GPS data, they obtained a model (Model 4) with the maximum slip of ~23 m at (38.06°N, 142.80°E, 24.4 km), rake 79° at the peak slip, and an average rake of 83°. Both slip models explain the onshore GPS data equally well, but the slip model using the offshore GPS data has been proven to fit the tsunami observations much better than the model with only onshore

GPS data [*Wang et al.*, 2013]. The slip orientation of our model is obviously closer to Model 1 than 4, further demonstrating that the GRACE data is able to provide additional constraint similar to the offshore GPS observation. In addition, the RMS and relative differences (equation 2.17) between the GRACE observation and these two slip model predictions are computed and the results are shown in Table 4.2, showing that GRACE is closer to Model 1 than Model 4, with an RMS of 1.5 and 1.6 μGal for g_N, respectively.

		g_N	*Txx*	*Txy*	*Txz*
CSR solution RMS		3.08 μGal	0.18 mE	0.15 mE	0.23 mE
CSR solution minus Model 1*	RMS	1.5 μGal	0.078 mE	0.086 mE	0.118 mE
	Relative difference	47.75%	43.72%	57.94%	50.42%
CSR solution minus Model 4§	RMS	1.6 μGal	0.093 mE	0.089 mE	0.131 mE
	Relative difference	53.11%	52.01%	60.19%	55.82%

Table 4.2. RMS and relative differences between the GRACE observation and two slip models predictions.
*Model 1 is the slip model [*Wang et al.* 2013] determined using both onshore and offshore GPS/Acoustic Network data
§Model 4 is the slip model [*Wang et al.* 2013] determined using only onshore GPS data

Our new approach can retrieve significantly more enhanced coseimic gravity change signals. We obtained a peak magnitude of –17.6±1.1 μGal (Figure 4.2a) for g_N change, larger than previously published values, e.g., than the peak coseismic g_D change of –7 μGal estimated by *Matsuo and Heki* [2011], and than the peak g_D change of –8.75±1.6 μGal estimated by *Wang et al.* [2012b], even though the seismic gravity change of the component g_D is always larger than the change of other two components, including g_N change. Using an elaborate simulated annealing algorithm inversion scheme and the improved GRACE gravity and gravity gradient observations (g_N, *Txx*, *Txy*, *Txz*), we demonstrated that GRACE data can provide a good constraint to fault seismic moment, fault width, especially for rake angle and centroid location. Our solution produces a

centroid location that is close to the latitude of GCMT solution and the longitude of USGS solution and gives a slip orientation that is about 5^0–10^0 clockwise from published GPS/seismic slip models. Compared to the two slip models given by *Wang et al.* [2013], our slip model is closer to Model 1 that is resolved using both onshore and offshore GPS data than Model 4 which used only onshore GPS data, indicating that GRACE data independently contain reliable signal over the offshore area. However, the question of how the systematic or stochastic error from GRACE data affect the resolved parameters need to be further studied. Nevertheless, our inverted fault model still has around 40% relative difference (39%, 27%, 52%, 40% for g_N, *Txx*, *Txy*, *Txz*) using GRACE observations. This may be due to the fact that our uniform dislocation model is too simple to represent the actual fault mechanism, which is a subject for future studies.

4.2 Inversion of point source parameters for recent large undersea earthquakes

Previous studies [*Han et al.,* 2011, 2013; *Cambiotti & Sabadini*, 2013; *Dai et al.,* 2014] showed the constraint of GRACE data on centroid horizontal location and centroid depth. Here we propose to solve for all source parameters of a point source including centroid depth and location together with the seismic moment tensor, using the north component of gravity and gravity gradient change from GRACE data. The inversion approach is the least-squares adjustment method combined with the simulated annealing algorithm as discussed in section 2.3.1, with its precision evaluated in section 2.4.

4.2.1 The 2004 Sumatra-Andaman and 2005 Nias earthquakes

The 26 December 2004 Sumatra-Andaman (Mw 9.2) megathrust earthquake was the largest earthquake in the last 50 years, and it ruptured about 1500 km of the subduction zone along the India-Burma plate boundary. Three months later, the 28 March 2005 Nias

(Mw 8.6) earthquake ruptured about 300 km at the adjacent Australia-Sunda plate boundary. In this study, we evaluate the cumulative coseismic slip deformation for the two events from GRACE data, considering the short time difference between these two earthquakes.

For the great 26 December 2004 Sumatra-Andaman earthquake, numerous studies have been conducted using seismic waves [*Ammon et al.,* 2005; *Lay et al.*, 2005; *Park et al.,* 2005; *Stein and Okal,* 2005], GPS data [*Vigny et al.,* 2005; *Banerjee et al.,* 2005, 2007], tsunami data [*Tanioka et al.,* 2006; *Fujii and Satake*, 2007; *Geist et al.,* 2007; *Poisson et al.,* 2011], GRACE data [*Han et al.,* 2006; *de Linage et al.,* 2009; Wang *et al.,* 2012c; *Han et al.,* 2013], both seismic waves and GPS offsets [*Rhie et al.,* 2007], and the combination of GPS data and vertical displacements from coral reefs and remote sensing optical images [*Chlieh et al.,* 2007]. As pointed out by *Chlieh et al*. [2007], the source parameters are difficult to be constraint by teleseismic body waves due to the interference between direct and reflected waves caused by the long duration (about 515 second) of rupture. The moment magnitude, M_W, a first-order characteristic of this earthquake, is poorly constrained by purely seismological methods, which ranges between 9 and 9.3 [*Ammon et al.,* 2005; *Lay et al.*, 2005; *Park et al.,* 2005; *Stein and Okal,* 2005]. Also, the seismic moment can be underestimated using the seismic waves with period too short to represent the rupture process [*Lay et al.,* 2005]. The large misfit between the seismological slip model prediction and the near-field displacement measurements reveals the deficit of the slip distribution from seismological data without near-field geodetic data [*Chlieh et al.,* 2007]. In addition, seismic data are inadequate for detecting aseismic slip and postseismic slip [*Chlieh et al.,* 2007; *Han et al.,* 2013]. For the 2004

Sumatra-Andaman earthquake, the aseismic slip, much larger than the total moment of aftershocks, dominates the postseismic deformation one month after the main shock. The former has the moment about 35% of the coseismic moment, and the later has moment less than 1% of the postseismic slip [*Chlieh et al.,* 2007]. Although GPS data can overcome the inadequacy of seismological data in detecting slow/aseismic slip, they are limited by the spatial distribution of the GPS stations. Here we first compare GRACE measurements with the gravity change predicted from the slip model by *Chlieh et al*. [2007], then we solve for the fault parameters using GRACE-derived gravity and gravity gradient change.

For the forward model prediction of gravity changes, we adopt the coseismic slip distribution model given by *Chlieh et al*. [2007] for the 2004 Sumatra-Andaman earthquake and the coseismic slip model by *Konca et al.* [2007] for the 2005 Nias earthquake, which is shown as the red image in Figure 4.14. The coseismic slip model (http://www.tectonics.caltech.edu/slip_history/2004_sumatra/update1/slipAceh_BSSA2007) [*Chlieh et al*., 2007] contains three subsegments, starting from the south part of the India-Burma plate boundary and extending about 1500 km along the trench to northern Andaman Islands. The dip angle for these three subsegments are 12°, 15°, and 17.5° from south to north, which are approximated based on the seismicity-based slab contours [*Ammon et al.,* 2005]. The slip patches are shallower near the trench, and go deeper along the dip direction (toward land). The slip model [*Konca et al.,* 2007] for the 2005 Nias earthquake (http://www.tectonics.caltech.edu/slip_history/2005_sumatra/update2/static_out) is the red image near south Sumatra along the Australia-Sunda plate boundary. Slip distribution model given by *Chlieh et al*. [2007] are generated from near field geodetic

measurements and 39 far-field GPS measurements. The near field geodetic data are about 100 km to 300 km away from the trench, including 23 campaign GPS measurements between 28 January and 19 February 2005, several GPS campaign measurements between September 2003 and February 2005, 12 GPS measurements between 11 and 22 January 2005, vertical displacements of coral reefs on Simeulue Island about 50 km south of the epicenter on 17 and 18 January and 5 February, and vertical displacements from remote sensing optical images. These near field GPS measurements contain about 20 days to 40 days of postseismic displacements, which are used to invert for the 30 days postseismic slip model.

We adopt the earth model in [*Chlieh et al*., 2007] as shown in Table 4.3 and the earth model in [*Konca et al.,* 2007] for the forward prediction of gravity and gravity gradient change corresponding to the coseismic slip model for the 2004 Sumatra-Andaman and the 2005 Nias earthquakes. The thickness of the ocean layer (1.8 km) is estimated as the mean value over the coseismic slip model from the bathymetry data in CRUST2.0 model. Since the provided slip patches' depth is relative to the average elevation of the GPS stations, the depth is re-adjusted to be relative to the ocean floor according to equation (A.1) in appendix A. The down component of gravity change and vertical displacement are computed at a regular 0.1°N by 0.2°E grid on the ocean floor for the solid earth model using the software PSGRN/PSCMP. The surface density change caused by the change of ocean thickness responding to the vertical deformation is calculated using the methodology in section 2.1.1. The gravity change due to solid earth deformation and surface density change at ocean floor is then transformed to geopotential spherical harmonic coefficients up to degree 899. Next, the each component of gravity and gravity

gradient change is computed at a regular grid on Earth's semi-major axis (6378.1363 km) instead of on ocean floor (with the radius as 6376.3 km, equation A.2), from the coefficients up to degree 65 to be commensurable with GRACE data. The effect of ocean response for gravity change is about 30% of that from solid earth. The gravity and gravity gradient change up to degree 65 using the procedure described above for each of the coseismic slip model by *Chlieh et al*. [2007] and *Konca et al.* [2007] are then summed together as shown in Figures 4.9~4.10.

Layer	Vp (km/s)	Vs (km/s)	Density (kg/m^3)	Thickness (km)
Ocean	1.5	0	1020	1.8
Sediment	5	2.5	2600	1.7
Upper Crust	6.6	3.65	2900	2.3
Middle Crust	7.1	3.9	3050	2.5
Lower Crust	8.08	4.473	3375.4	196
Mantle	8.594	4.657	3446.5	-

Table 4.3. Earth Model [*Chlieh et al.,* 2007]

For these giant megathrust earthquakes, we present the gravity and gravity gradient change estimated from the 137 high degree monthly solutions (up to degree 90) of GFZ RL05a NMAX 90 product from April 2002 to August 2014. CSR RL05 NMAX 96 product are also used to study the coseismic gravity change using 138 monthly solutions from April 2002 to September 2014, but shows a worse model-data misfit compared to GFZ RL05a product. Four large earthquakes occurred in Sumatra and its nearby region in the last decade, including the 2004 Sumatra-Andaman (Mw 9.2) and 2005 Nias (Mw 8.6) earthquakes, the 2012 Indian Ocean earthquakes (Mw 8.6 and Mw 8.2), and the 2007 Bengkulu earthquake (Mw8.5). Considering the overlap of the fault area, and three coseismic jumps are estimated simultaneously for time series at each grid point. The 2005

Nias (Mw 8.6) earthquake is not separated from the 2004 Sumatra-Andaman (Mw 9.2) earthquake, due to the short time difference between these two events.

Based on the localized spectral analysis, GFZ RL05a solutions are truncated to degree 65 to retrieve g_N, *Txx, Txy, Txz* (*x, y, z,* is north, west, up direction) time series as shown in Figure 4.7. The uncertainties (blue shading) are standard deviations propagated from the formal error of each coefficient. We can see that g_N significantly decreases by about 34±1.4 μGal, which is by far the highest coseismic signal achievable by innovative GRACE data processing. For *Txz*, the increase is also substantial, about 2.5±0.13 mE. The localized degree variance [*Wieczorek & Simons*, 2005] is carried out using Slepian tapering window centered at the fault area. This localized spectra analysis can evaluate the signal and noise level of each component of gravity and gravity gradient change as a function of degree. We can see that the GRACE-observed g_N change agrees well with the model prediction up until around degree 70, although the amplitude is slightly larger than the model prediction. Same for the gravity gradient change, GRACE-observed value is larger than the model prediction but has good agreement until around degree 65. Above degree 65, the GRACE data is much higher than the model prediction, which we interpret as noise. While, the degree variance of GRACE-observed g_E and g_D change (Figure 4.8a) increases starting from degrees as low as 30, indicating that degrees higher than that are dominated by noise. We can also see that both gravity gradient and gravity change induced by earthquakes have higher power for the higher degrees. One other important application of this localized spectra analysis is that it is an efficient method to guide the choice of practical degree truncation. As shown in Figure 4.8, the degree variance for g_N change keeps in good agreement with the model prediction until around degree 70, so we

choose to discard the spherical harmonic coefficients above degree 65, based on additional comparison in spatial domain.

For the GRACE-derived g_N change, the overall positive-negative-positive pattern over the Aceh region and surrounding ocean is consistent with the slip model prediction. The maximum g_N change is –34±1.4 μGal at 95°E, 4.05°N, almost twice of the model prediction at the same point, –19.4 μGal. GRACE-derived g_N change is larger than the model prediction mainly due to the small shear modulus value (30 GPa) applied in our forward prediction, which underestimate the moment by about half as discussed later. In addition, the orientation of the GRACE-observed pattern rotates slightly anticlockwise with respect to the model-predicted g_N change, which explains the 8° smaller slip azimuth estimated by GRACE data compared to the model prediction as shown later. However, the GRACE-derived g_E (Figure 4.9b) and g_D (Figure 4.9c) change is contaminated by the stripe noise. Coincide with g_N change, the GRACE-derived gravity gradient change (Figure 4.10), *Txx*, *Txy*, *Txz* also matches well with the model prediction, with slightly anticlockwise rotated spatial orientation. The magnitude is larger than the model prediction as well due to the smaller shear modulus, for example, the peak value of *Txz* is at 94.8°E, 4.15°N, 2.53±0.13 mE, larger than the model-predicted *Txz*, 1.36 mE. We also use the CSR RL05 NMAX 60 product to retrieve the gravity and gravity gradient change from 137 monthly solutions from April 2002 to September 2014. We can see that gravity and gravity gradient change (Figures 4.11~4.13) agrees well with the model prediction, even the down component of gravity change has good agreement with model prediction.

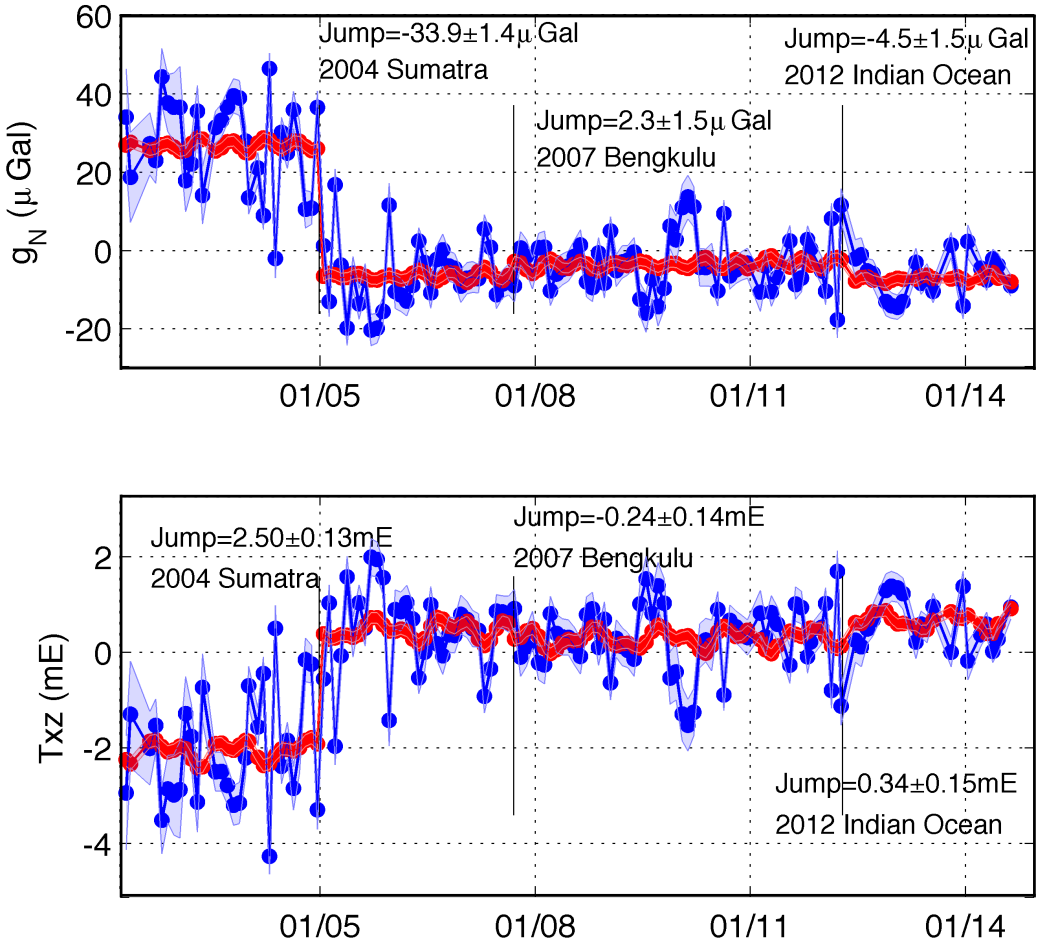

Figure 4.7. Time series of g_N, *Txz* at 95°E 4.05°N.
Blue lines are the g_N (top), *Txz* (bottom) disturbance generated from 137 monthly GFZ RL05a gravity field solutions up to degree 65 from April 2002 to August 2014. The blue shadings are standard deviations propagated from the formal error of each coefficient. The red lines are the fitted value using linear trend, periods, and Heaviside step functions.

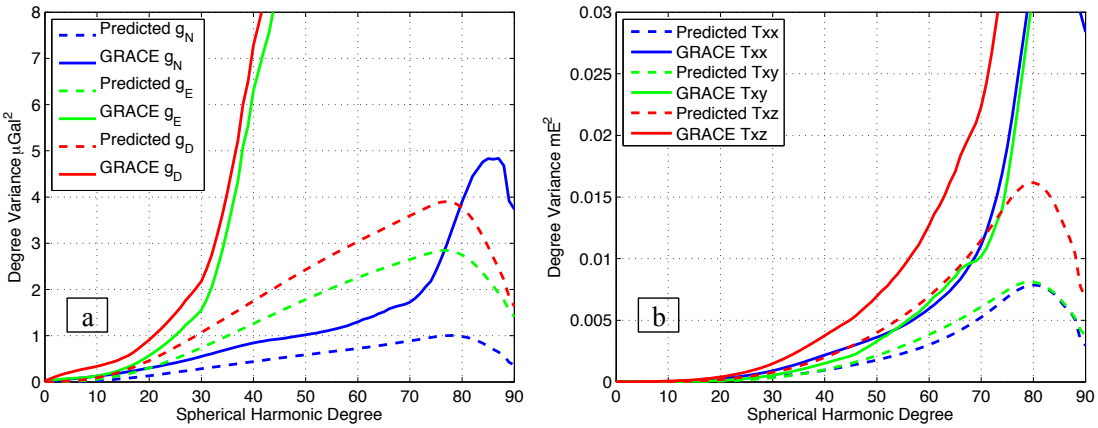

Figure 4.8. Comparison in the spectral domain.
The localized degree variance as a function of spherical harmonic degree is shown for the observed and model-predicted g_N, g_E, g_D change (a), and *Txx*, *Txy*, *Txz* change (b) up to degree 90.

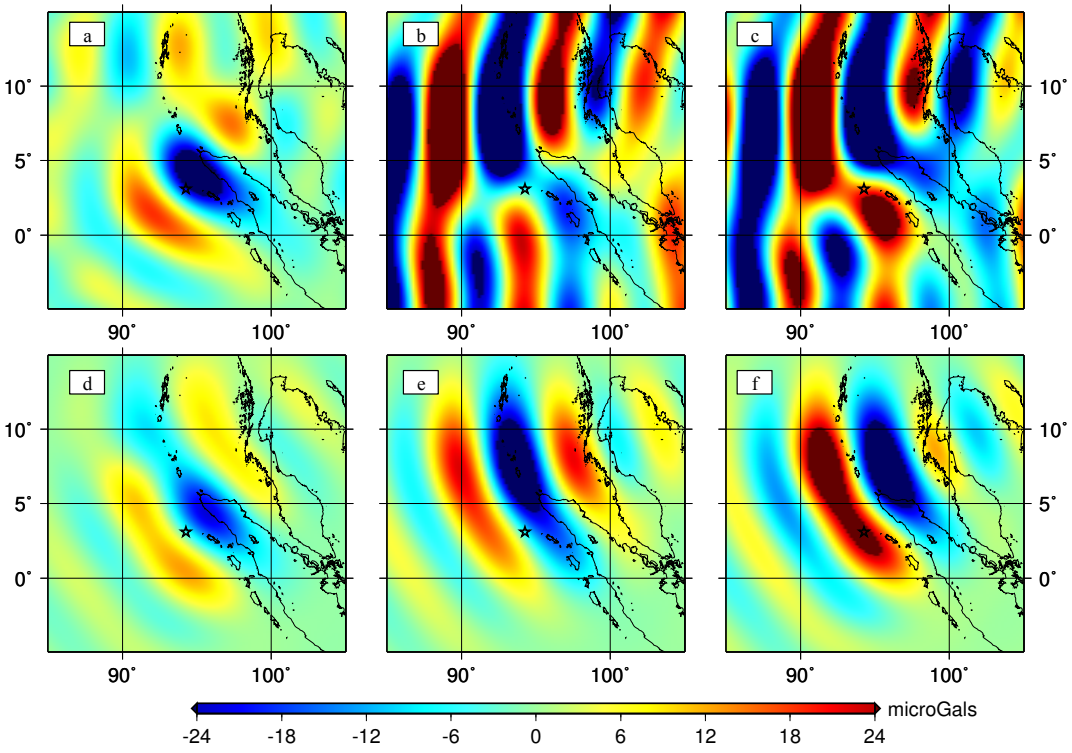

Figure 4.9. Comparison of GRACE-observed and model-predicted coseismic gravity changes up to degree 65 from GFZ RL05a product.
(a) ~ (c): GRACE-observed g_N (a), g_E (b), g_D (c) change. (d) ~ (f): seismic-model-predicted g_N (d), g_E (e), g_D (f) change. The black star is the GCMT centroid (94.26°E, 3.09°N).

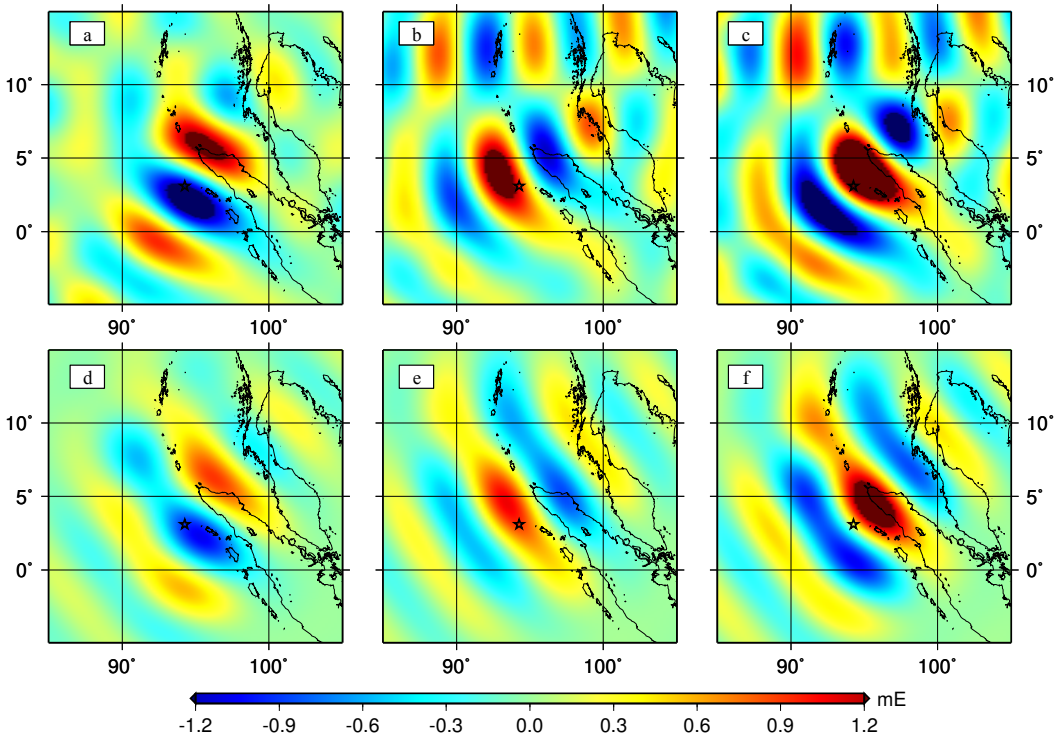

Figure 4.10. Comparison of GRACE-produced and model-predicted gravity gradient change up to degree 65 from GFZ RL05a product.
(a) ~ (c): GRACE-produced *Txx* (a), *Txy* (b), *Txz* (c) change. (d) ~ (f): seismic-model-predicted *Txx* (d), *Txy* (e), *Txz* (f) change. The black star is the GCMT centroid.

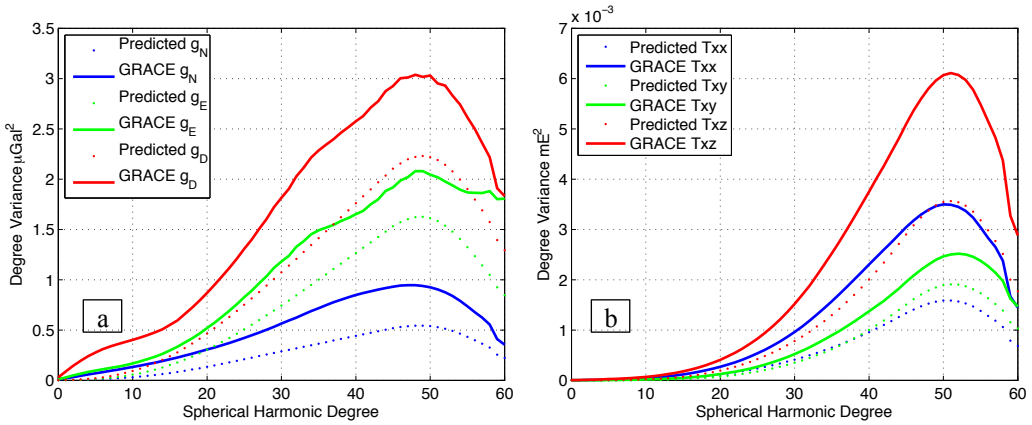

Figure 4.11. Comparison in the spectral domain for CSR RL05 NMAX 60 solution results.
(a) the localized degree variance as a function of spherical harmonic degree for the observed and model-predicted g_N, g_E, g_D change. (b) the localized degree variance for the observed and model-predicted *Txx*, *Txy*, *Txz* change.

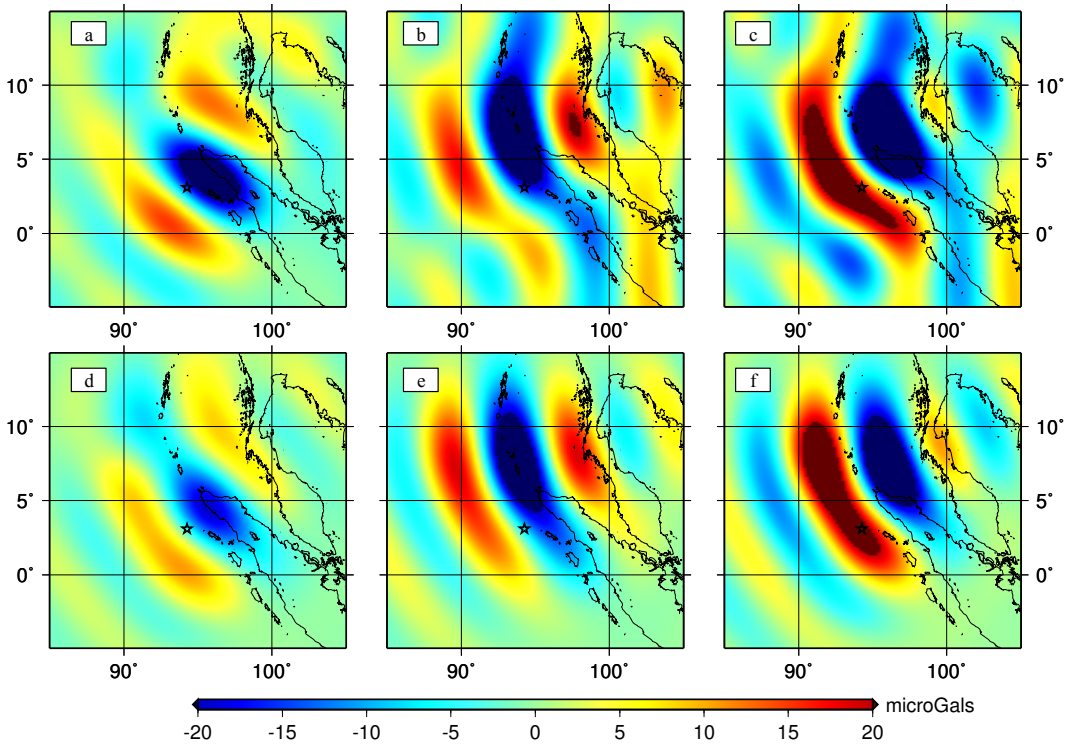

Figure 4.12. Comparison of GRACE-observed and model-predicted coseismic gravity changes up to degree 60 from CSR RL05 NMAX 60 product.
(a) ~ (c): GRACE-observed g_N (a), g_E (b), g_D (c) change. (d) ~ (f): seismic-model-predicted g_N (d), g_E (e), g_D (f) change. The black star is the GCMT centroid.

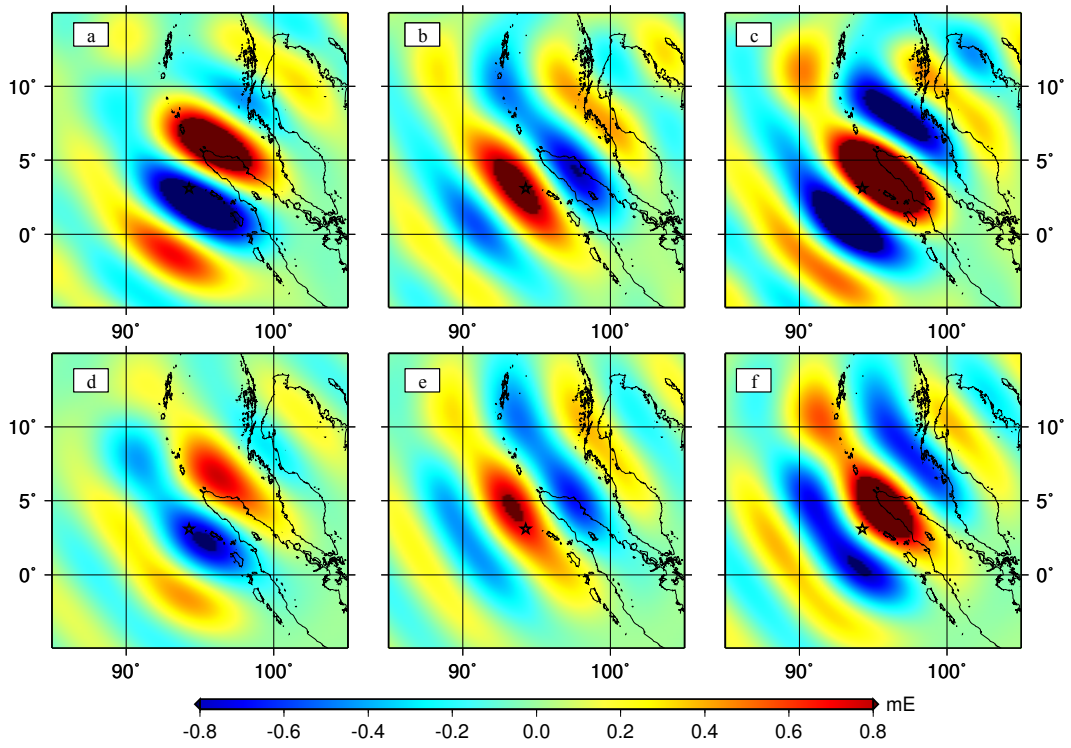

Figure 4.13. Comparison of GRACE-produced and model-predicted gravity gradient change up to degree 60 from CSR RL05 NMAX 60 product.
(a) ~ (c): GRACE-produced *Txx* (a), *Txy* (b), *Txz* (c) change. (d) ~ (f): seismic-model-predicted *Txx* (d), *Txy* (e), *Txz* (f) change. The black star is the GCMT centroid.

Centroid moment tensor inversion is carried out using the least-squares adjustment, and the centroid location and depth are inverted using the simulated annealing algorithm. For our source parameters inversion, we adopted the same earth structure model as in [*Chlieh et al.,* 2007] to reduce the bias caused by structural differences. First-order source parameters are important physical quantities in seismology as well as for application in tsunami warning [*Geist et al.,* 2007]. In the following paragraphs, we compare our estimated source parameters, such as centroid location and depth, seismic moment, dip angle, strike and rake angle, with those from seismic and geodetic data.

The estimated location (red star in Figure 4.14) is remarkably close to the GCMT solution (**black** star, http://www.globalcmt.org/). It is west of the USGS CMT (http://comcat.cr.usgs.gov/earthquakes/eventpage/official20041226005853450_30#scientific_summary, green beach ball), and south of the cumulative coseismic slip models (blue beach ball) [*Chlieh et al.,* 2007; *Konca et al.,* 2007]. *Poisson et al.* [2011] demonstrate that the best model that reproduces the tsunami data among five published slip models is the slip model in [*Rhie et al.,* 2007], which has the peak slip at south of Nicobar Island, close to our centroid location. The northward of the centroid location (blue beach ball) by [*Chlieh et al.,* 2007] may be caused by the constraint from the larger amplitude of GPS measurements in the north part around Nicobar Island and Andaman Island [*Ammon et al.,* 2005; *Chlieh et al.,* 2007]. On the other hand, for the coseismic slip model [*Chlieh et al.,* 2007], the fault geometry of the three segments are fixed to the presumed values, which are based on the geometry of the India-Burma plate interface, i.e. strike angles are approximated according to the direction of the local trench, and dip angles are approximated based on seismicity-based slab contours [*Ammon et al.,* 2005]. The source parameters that are actually constrained by the geodetic data are rake angle, seismic moment, and centroid location. Although the centroid location is estimated from the distribution of slip on each fault patch, it's still constrained to some extent by the presumed fault location [*Lay et al.,* 2010].

Our estimated centroid depth (9.1 km) is much shallower than the depth (28.6 km) resolved using seismic data (GCMT and USGS CMT) and the depth (28.3 km) from geodetic data [*Chlieh et al.,* 2007; *Konca et al.,* 2007]. The underestimation of slip at the updip direction and overestimation of slip at downdip direction (closer to measurements)

from the checkerboard test [*Chlieh et al.,* 2007], might explain the deeper centroid by geodetic data compared to our solution by GRACE data. In addition, the shallow region near trench sediments is thought to accommodate relative plate motions aseismically, as pointed out by *Lay et al.* [2012]. Hence, the aseismic afterslip, which releases the moment about 35% of the coseismic moment [*Chlieh et al.,* 2007], might occur at the shallow region, contributing toward a shallower centroid depth. Finally, the GRACE-solved location is closer to the trench, which indicates a shallow source.

Our estimated centroid moment tensor, with the moment of 6.09×10^{22} Nm, is the total of the coseismic slip of the 2004 Sumatra-Andaman earthquake, the aseismic afterslip and postseismic slip over the following three months, and coseismic slip of the 2005 Nias earthquake. The estimated moment is smaller than the sum (10.37×10^{22} Nm) of the coseismic moment 6.93×10^{22} Nm, one-month postseismic moment 2.44×10^{22} Nm by [*Chlieh et al.,* 2007], and the coseismic moment 1.0×10^{22} Nm [*Konca et al.,* 2007] for the 2005 Nias earthquake. However, considering the strong dip dependence of moment estimates, and the fact that the quantity $\boldsymbol{M_0}$ sin 2δ is better constrained than each of $\boldsymbol{M_0}$ and dip angle (δ) [*Kanamori and Given,* 1981], the total moment by *Chlieh et al*. [2007] and *Konca et al.* [2007] corresponds to 5.4×10^{22} Nm for dip angle of 32°, which is closer to our estimated $\boldsymbol{M_0}$. It is also larger than the cumulative seismic moment (5.01×10^{22} Nm) for the two events by GCMT and USGS CMT. One point to mention is that in Table 4.4, the calculated moment by equation (C.1) shown in parenthesis is only about half of the total of the two published moments by *Chlieh et al*. [2007] and *Konca et al.* [2007]. The reason for the underestimation is that our forward modeling software PSGRN/PSCMP adopts a constant shear modulus, μ, as 30 GPa, for the calculation of seismic moment,

which is smaller than the value used in their evaluation. The value published by *Chlieh et al*. [2007] and *Konca et al.* [2007] should be used for comparing the estimated seismic moment between different solutions; while our underestimated $\boldsymbol{M_0}$ for their slip model explains the smaller magnitude of model prediction for the spatial and spectral comparison.

Dip angle is another important source parameter since the estimation of moment has a strong dependence on dip [*Banerjee et al.,* 2005; *Rhie et al.,* 2007; *Han et al.,* 2011]. The sensitivity test by *Rhie et al.* [2007] shows the dip angle is not well resolved using the long-period teleseismic data and near-field GPS displacements. Our estimated dip angle is 32° (Table 4.4), larger than the mean value (14°) of cumulative coseismic slip models by *Chlieh et al*. [2007] and *Konca et al.* [2007]. Nevertheless our dip angle is close to the dip angles in [*Banerjee et al.,* 2005, 2007] using far-field GPS displacements, which adopt dip angle as 35° for the deeper portion of the segments (30-50 km) based on the dip angles of after shocks and 11° to 18° for the shallow portion of the segments (0-30 km). In addition, *Banerjee et al.* [2005] also show the better model-data fit with the larger dip angle compared to that with the smaller dip angle. Our slip azimuth (equation 4.1) is about 8° clockwise of the GCMT and USGS CMT solution, and 8° anticlockwise of the cumulative slip distribution models by *Chlieh et al*. [2007] and *Konca et al.* [2007]. The fact that the slip azimuth estimated by GRACE data is 8° smaller than that by the cumulative slip models, is evident by the slightly rotated spatial pattern of the GRACE observed gravity and gravity gradient change. The strong correlation between strike and rake angle (Table 4.5) is consistent with the trade-off between these two angles as discussed in the sensitivity test. *Han et al.* [2013] explained that only the difference

between strike and rake angle could be better constrained for low-dip earthquakes, since the two dominant moment tensor components can be approximated to $M_{xz} \approx -M_0 \cos(\phi_s - \lambda)$, $M_{yz} \approx M_0 \sin(\lambda - \phi_s)$, when the dip angle is small, which shows that the strike angle, ϕ_s, and rake angle, λ, are tightly coupled.

Model name	**Data Sources**	**Centroid**		**Strike (°)**	**Dip (°)**	**Rake (°)**	M_0 in 10^{22} Nm
		Location	**Depth**				
Cumulative model (***Chlieh et al.*, 2007; *Konca et al.*, 2007**)	GPS, coral uplift and uplift from satellite images. GPS, coral uplift, teleseismic data	Blue beach ball	28.3 km	340	14	104	6.93 +1.0 (3.76)
GCMT	Long-period mantle waves	**Black** star and beach ball	28.6 km	329	8	110	3.96 +1.05
USGS CMT	Seismic data	Green beach ball	28.6 km	329	8	109	3.96 +1.05
This study	GRZ RL05a	Red star and beach ball	9.1 km	339±0.1	32±0.05	111±0.2	6.09±0.01

Table 4.4. Comparison of Source Parameters.
The additional seismic moment $\boldsymbol{M_0}$ in Orange color is for the 2005 Nias earthquake (http://comcat.cr.usgs.gov/earthquakes/eventpage/centennial20050328160937#scientific_moment-tensor). The $\boldsymbol{M_0}$ in parenthesis, 3.76 $\times 10^{22}$ Nm, is our estimated value from the slip models given by *Chlieh et al*. [2007] and *Konca et al.* [2007], which is smaller than the sum of the two published moments for the same slip models.

	Strike	Dip	Rake	M_0
Strike	1	0.4	1	–0.4
Dip	0.4	1	0.5	–0.4
Rake	1	0.5	1	–0.6
M_0	–0.4	–0.4	–0.6	1

Table 4.5. The correlation between parameters

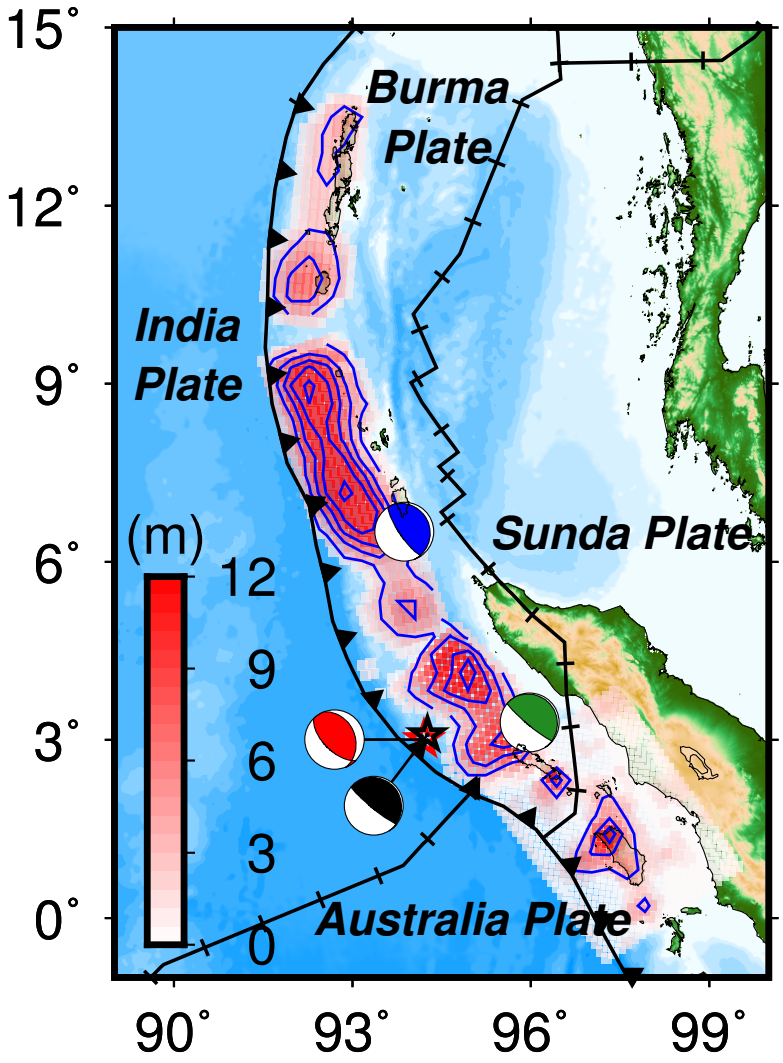

Figure 4.14. Comparison of centroid moment tensor solutions.
The blue slip contours are for the cumulative slip distribution models (red 2D image) [*Chlieh et al.,* 2007; *Konca et al.*, 2007] on the fault plane. The red image along the India-Burma plate boundary is for the slip model by *Chlieh et al*. [2007] for the 2004 Sumatra-Andaman earthquake, and the red 2D map along the Australia-Sunda plate boundary is for the slip model [*Konca et al.,* 2007] of the 2005 Nias earthquake. The blue beach ball represents the centroid location and moment tensor estimated from the cumulative slip distribution models. The GCMT solution is denoted as the **black** beach ball, with location at the **black** star. Green beach ball represents USGS CMT solution and location. Red beach ball is CMT solution from GRACE data, with the location at the red star (94.20°E, 3.00°N, 9.1 km). The thick black line is the plate boundary, with black triangular representing the subduction zone.

4.2.2 The 2011 Tohoku earthquake

For the 11 March 2011 Tohoku earthquake (Mw 9.0), we use the GRACE-derived north component of gravity and gravity gradient change presented in Chapter 3 from CSR RL05 NMAX 96 product to solve for the centroid moment tensor of the earthquake source. As shown, the GRACE-observed g_N, *Txx, Txy, Txz* (*x, y, z,* is north, west, up direction) change can be retrieved up to degree 70, which is by far the highest degree of coseismic signal achievable by GRACE. Here we show the source parameters inverted using the GRACE-observed g_N, *Txx, Txy, Txz* change data.

The estimated centroid location and CMT from this high degree L2 product are basically consistent with the finite fault parameters (denoted as solution 1) inverted using GRACE CSR RL05 NMAX 60 product as shown in section 4.1.2. The location is at 142.2°E, 37.65°N (red beach ball in Figure 4.15), only 13 km away from the centroid location of solution 1 within the error range. The consistency of the two solutions demonstrates the coherence of the two GRACE products, as well as the coherence of the finite fault modeling and the centroid moment tensor modeling. As discussed in section 4.1.2, the GRACE-estimated centroid location is almost parallel in latitude with the GCMT centroid, and about 30 km west of the USGS CMT centroid. Regards to its distance to the coast, GRACE-estimated centroid is in between the location estimated by GPS data only [O*zawa et al.*, 2011] and the location (blue beach ball) estimated by the combined seismic waves data and on-land/offshore GPS data [*Wei et al.*, 2012]. The GRACE-estimated depth (16 km) agrees well with the centroid depth (18 km) by combined seismic data and GPS data [*Wei et al.*, 2012], as well as the centroid depth (17 km) constrained by GRACE KBR data [*Han et al.,* 2011].

The GRACE-estimated seismic moment, $(4.03\pm0.01)\times10^{22}$ Nm, is slightly smaller than the published results. The GRACE-estimated dip angle (12±0.1°) agrees incredibly well with the published results, with difference less than 2 degrees. Although the strike (236±0.5°) and rake angle (113±0.5°) are about 30 degrees larger than the angles inverted from the finite fault model that fixed the strike angle at 201°, considering the strong correlation between the strike and rake angle (Table 4.6), our slip azimuth (123°) is almost the same with the slip azimuth (124°) inverted by solution 1. This slip azimuth is consistent with the earlier conclusion that the GRACE-inverted slip direction is about 10° clockwise from that inverted by GPS and seismic waves data [*Wei et al.*, 2012], only about 3° clockwise from the USGS CMT slip direction. Furthermore, this clockwise rotation of the slip direction is validated by another satellite gravity gradiometry-GOCE measurements [*Fuchs et al.*, 2013].

	Strike	Dip	Rake	M_0
Strike	1	0.4	1	0
Dip	0.4	1	0.2	0.1
Rake	1	0.2	1	0.1
M_0	0	0.1	0.1	1

Table 4.6. The correlation between parameters for SA inversion.

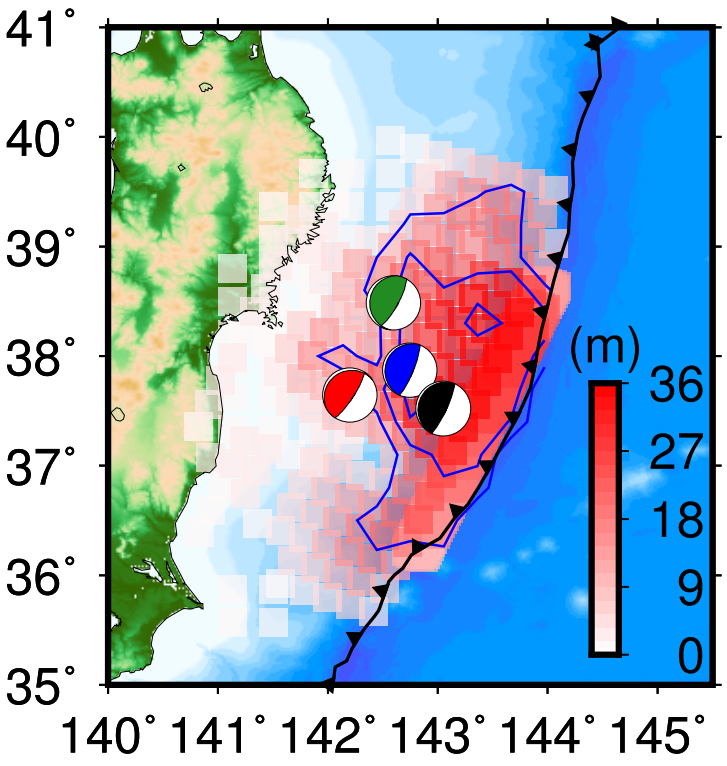

Figure 4.15. Comparison of centroid moment tensor solutions.
The red image overlapped on the topography/bathymetry along the trench is for the cumulative coseismic and postseismic (March 2011) slip model [*Wei et al.*, 2012; *Ozawa et al.,* 2011], with contours represented by the blue lines and CMT denoted by the blue beach ball. Red beach ball is CMT solution from GRACE data (CSR RL05 NMAX 96 product), located at 142.2°E, 37.65°N, with depth as 16 km. Other markings are the same as in Figure 4.14.

4.2.3 The 2010 Maule, Chile earthquake

The 27 February 2010 Maule, Chile (Mw 8.8) earthquake ruptured about 500 km along Nazca-South American plate boundary, with the Nazca oceanic crust subducting under the continent of the South American plate to the east direction. The g_N change would be expected to be smaller for east-west slip earthquakes compared to north-south slip earthquakes. Here we demonstrate the GRACE-observed g_N, *Txx*, *Txy*, *Txz* change for this

real case of east-west slip earthquake. The coseismic gravity and gravity gradient change up to degree 60 are retrieved using 137 monthly solutions from CSR RL05 product from April 2002 to September 2014, excluding the solution for month February 2010.

For the forward model prediction, we start from the USGS finite fault model by *Hayes* [2010] (http://on.doi.gov/yVUcUQ), shown as the red image overlapped on top of the local topography/bathymetry in Figure 4.20. We retrieve the 1-D velocity model by the average of the velocity model over the fault area from CRUST 2.0 model. The average thickness of ocean over the fault plane is 1.3267 km. The provided fault patches' depth is re-adjusted to be relative to the ocean floor by subtracting the ocean thickness from the depth. The upward continuation of the gravity change from ocean floor (with the radius of 6369.4049 m) to Earth's semi-major axis is considered. The difference of the gravity evaluated on ocean floor or on Earth's semi-major axis can be large for some earthquakes as shown in section 2.1.1, especially when the geocentric distance of the ocean floor over the fault area is much smaller than the Earth's semi-major axis, but it's not discussed in many researches [*Han et al.*, 2006; *Matsuo & Heki*, 2011; *Cambiotti and Sabadini*, 2012; *Wang et al.*, 2012b]. The effect of ocean response for gravity change is significant, about 60% of that from solid earth. The gravity and gravity gradient change up to degree 60 corresponding to the finite slip model [*Hayes,* 2010] are then computed as shown in Figures 4.18~4.19.

Layer	Vp [km/s]	Vs [km/s]	Density [kg/m^3]	Thickness [km]
Ocean	1.5	0	1020	1.3267
Sediment	2.2836	1.0898	2092.9	0.7466
Upper Crust	5.9555	3.3835	2696.3	8.5878
Middle Crust	6.5466	3.6977	2887.0	9.3678
Lower Crust	7.1671	3.9668	3083.9	8.9389
Mantle	8.1622	4.6764	3394.7	-

Table 4.7. Earth Model from CRUST 2.0

The time series of gravity and gravity gradient disturbance are fitted with periodicities, linear trend, and the coseismic jump. A posteriori variance of unit weight for each spherical harmonic coefficient is first estimated by fitting the coefficient time series of the CSR RL05 monthly solution with linear trend and periodicities. Then, the uncertainties for gravity and gravity gradient disturbance on each grid point are estimated through error propagation, shown as the blue shadings in Figure 4.16. We can see that the coseismic jump is substantial, with g_N increasing by 10.6±1.3 μGal, and *Txz* decreasing by 0.74±0.11 mE.

The localized degree variance demonstrates the signal and noise level of gravity and gravity gradient change. As shown in Figure 4.17a, the GRACE-observed g_N change agrees with the model prediction with slightly larger magnitude, but the g_E and g_D change goes much higher than the model prediction indicating it's dominated by noise, confirmed as the stripes (Figure 4.18 b~c) in spatial comparison. For the north component of gravity gradient change, they also agree well with the model prediction. Again, the model-predicted north component of gravity and gravity gradient change shows that the degree variance is larger for higher degrees, showing the high frequency characteristics of the coseismic gravity change. For the GRACE-derived g_N change, the quadruple spatial pattern is consistent with the model prediction. The peak g_N change is

10.6±1.3 μGal at 69.4°W 32.45°S as is shown in Figure 4.18a, slightly larger than the predicted value, 7.2 μGal. The north component of gravity gradient change (Figure 4.19) also match well with the model prediction, with peak value of *Txz* as –0.75±0.11 mE at 69.4°W 32.65°S, slightly larger than the model prediction, –0.51mE.

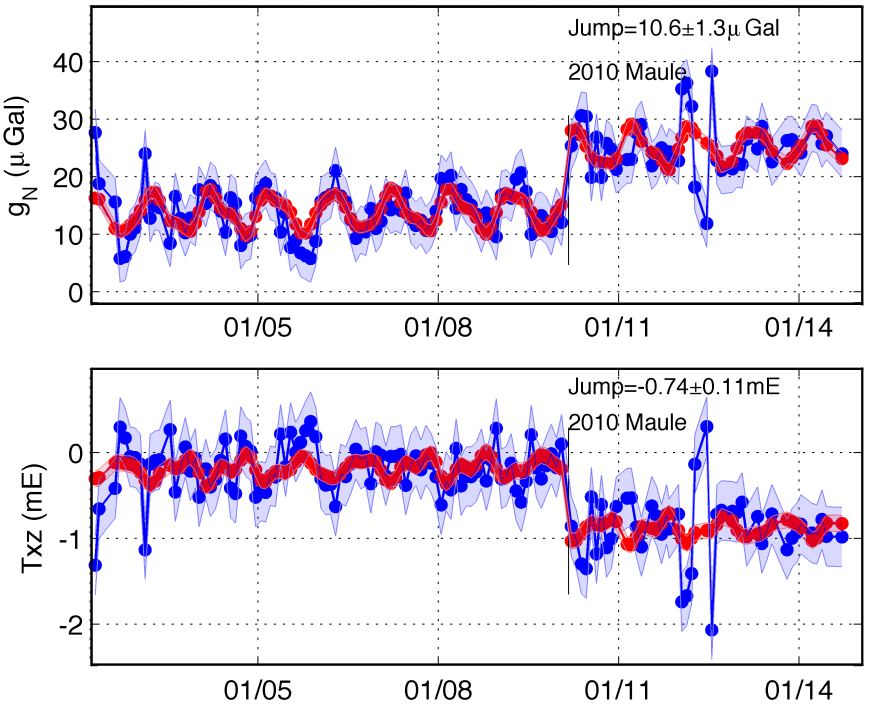

Figure 4.16. Time series at 69.4°W 32.45°S.
Blue lines are the g_N (top), *Txz* (bottom) disturbance generated from 137 monthly CSR RL05 solutions up to degree 60 from April 2002 to September 2014. The blue shadings are uncertainties propagated from the estimated *a posteriori* variance of unit weight for each coefficient. The red lines are the fitted value using linear trend, periods, and Heaviside step functions.

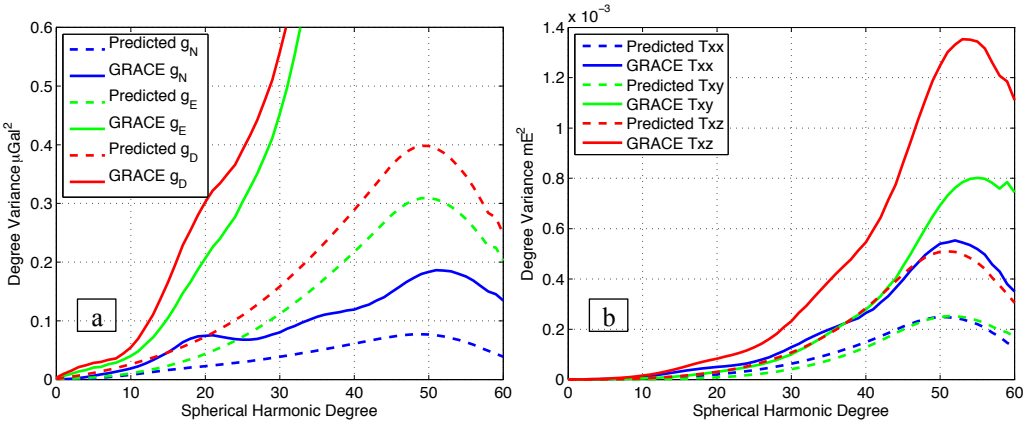

Figure 4.17. Comparison in the spectral domain.
The localized degree variance as a function of spherical harmonic degree is shown for the observed and model-predicted g_N, g_E, g_D change (a), and *Txx*, *Txy*, *Txz* change (b).

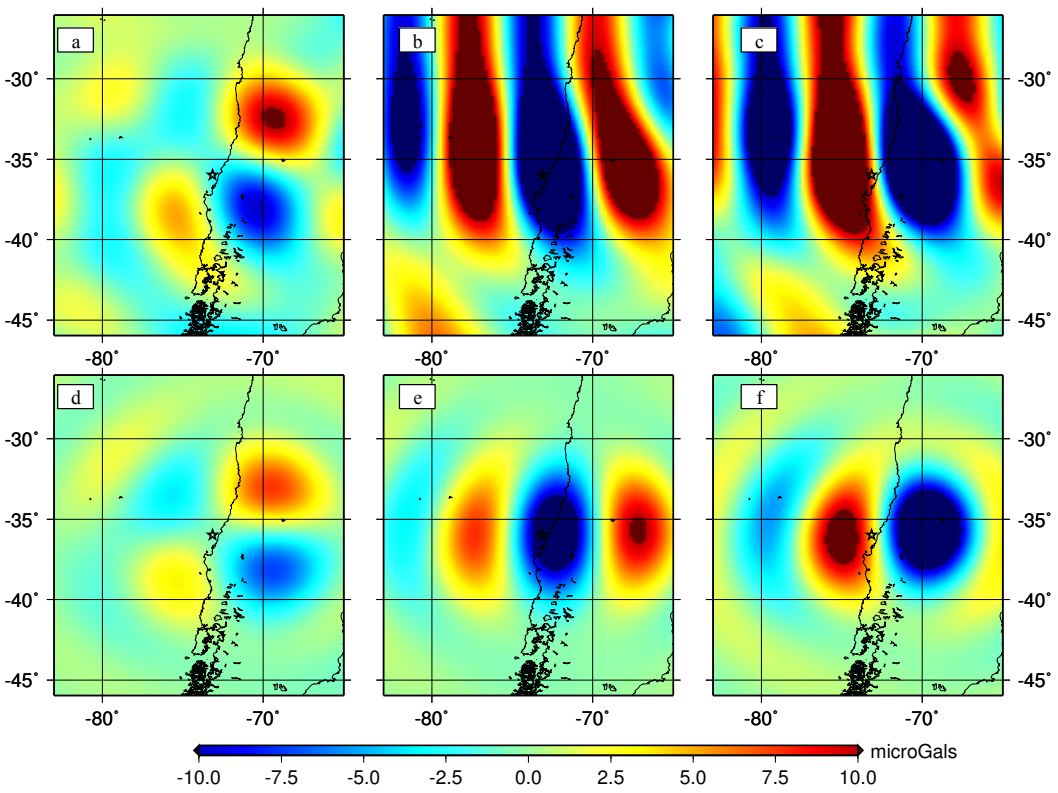

Figure 4.18. Comparison of GRACE-observed and model-predicted coseismic gravity changes up to degree 60 from CSR RL05 product.
(a) ~ (c): GRACE-observed g_N (a), g_E (b), g_D (c) change. (d) ~ (f): seismic-model-predicted g_N (d), g_E (e), g_D (f) change. The black star is the GCMT centroid (73.15°W, 35.98°S).

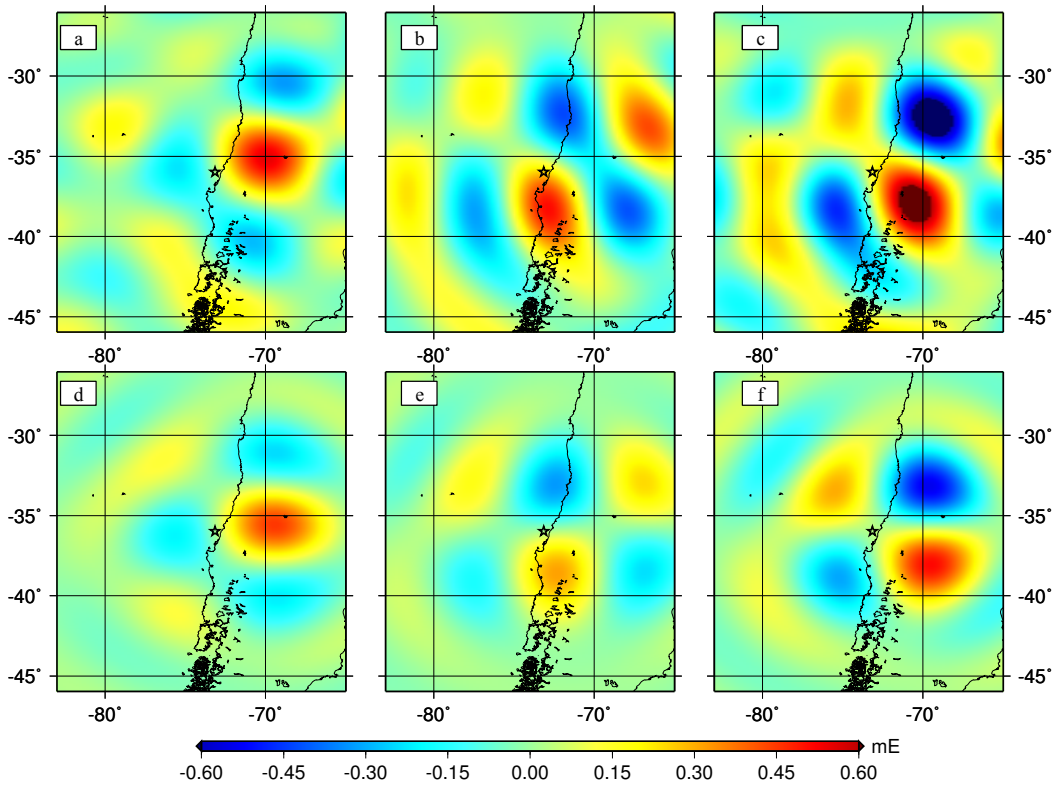

Figure 4.19. Comparison of GRACE-produced and model-predicted gravity gradient change up to degree 60 from CSR RL05 product.
(a) ~ (c): GRACE-produced *Txx* (a), *Txy* (b), *Txz* (c) change. (d) ~ (f): seismic-model-predicted *Txx* (d), *Txy* (e), *Txz* (f) change. The black star is the GCMT centroid.

Although using g_N from GRACE can reduce the noise level, the magnitude of coseismic g_N can be small compared to g_D depending on fault parameters, which may weaken the signal-to-noise ratio of g_N. When the slip vector points in the north/south direction, g_N is close to the magnitude of g_D, for example, the ratio of g_N over g_D is 0.97 (Table 4.8) with strike angle 270° and rake angle 90°. Nevertheless, g_N has smaller magnitude for some fault parameters, e.g., when slip vector points to plumb line, which leads to a ratio of 0.37 (Table 4.8). Another case is when slip vector is along the east-west direction, which gives a ratio as low as 0.35 (strike angle, 0°, rake angle, 90°, Table 4.8). The 2010 Maule, Chile earthquake is a real example for slip vector of this case (GCMT Centroid: strike, 18°, and

rake, 112°), which leads to the ratio of g_N over g_D as small as 0.39. The peak value of GRACE observed g_N for the 2010 Maule, Chile earthquake is 10.6±1.3 μGal (Figure 4.18a), at 69.4°W, 32.45°S, slightly greater than model prediction, 7.2 μGal (Figure 4.18d). Even for this adverse case, the GRACE-derived g_N change still has slightly larger magnitude than the peak g_D change of –8.0 μGal from GRACE data [*Wang et al.,* 2012a], due to the smoothing filter applied for g_D to reduce stripes. Nevertheless, the ratio of g_N over g_D may get further smaller for the east-west slip cases with different dip angles.

Dip angle (°)	Strike angle (°)	Rake angle (°)	g_N/g_D
9	270	90	0.97
9	0	90	0.35
90	200	90	0.37

Table 4.8. Comparison of g_N/g_D for three special cases.
Other fault parameters: fault length 600 km, fault width 300 km, depth 5 km, and slip 2 m.

GRACE-solved centroid location (73.4°W, 35.2°S, red star in Figure 4.20) using CSR RL05 product is northwest of the centroid solved by other data sets [*Hayes,* 2010; *Vigny et al.,* 2011]. For example, it is about 40 km north and 50 km west of the centroid location (blue beach ball) by *Hayes* [2010] from broadband seismic waves, and it is about 20 km west and 80 km north of the GCMT centroid (**black** beach ball). To check the uncertainty on solved source parameters caused by different GRACE L2 data processing, another two L2 products, the latest JPL RL05.1 and GFZ RL05a data products, are also used for the inversion. Both products are truncated at degree 50 to reduce the noise at high degrees. We can see that the GRACE-solved CMT locations by CSR RL05 and JPL RL05.1 products are almost identical to each other, which can be explained by the fact

that the two data products are solved using similar background models and data processing strategies. While the GFZ RL05a product produce a location about 50 km north and 50 km east of that by the CSR RL05 product. The discrepancy on the locations by three data products can to an extent represent the uncertainty of the centroid location inverted from GRACE data. Nevertheless, for this earthquake, GFZ RL05a data product shows a relatively worse noise level on the gravity and gravity gradient change (figures not shown), which is also shown by its worse RMS (e.g. 1.0 μGal for g_N) of data-model differences compared to the RMS (0.93 μGal for g_N) by the JPL RL05.1 product, where the model is the GRACE-inverted CMT solution using each data product.

GRACE-estimated depth (20.7 km) by the three L2 data products are the same, which indicates its small uncertainty. This GRACE-estimated depth is consistent with the published depths from geodetic data [*Vigny et al.,* 2011; *Pollitz et al.,* 2011a], which show major slip locates at the the shallow depth (<25 km). It is also close to the depth from seismic waves data by GCMT. Though, the depth of the highest slip in [*Lorito et al.,* 2011] is deeper around 25–40 km, coherent with the downdip location of the peak slip. The shallow slip given by GRACE and GPS data [*Vigny et al.,* 2011] is in consistency with the generation of a strong tsunami and the numerous aftershocks near the trench. *Koper et al.* [2012] state that there is nearly no relative depth resolution from teleseismic arrival times for a shallow-dipping fault; hence they fix the depth during the inversion.

GRACE-resolved seismic moment, $(2.17\sim2.6)\times10^{22}$ Nm, is very close to the M_0, 2.39×10^{22} Nm, by *Hayes* [2010]. But it's slightly larger than the M_0, $(1.55\sim1.97)\times10^{22}$ Nm, in [*Lorito et al.,* 2011; *Pollitz et al.,* 2011a; *Vigny et al.,* 2011], as well as that by

GCMT and USGS CMT. Nevertheless, GRACE-resolved dip angle (25~26°) is about 8° larger than the average value (18°) of dip angle by seismic waves and that by geodetic data [*Pollitz et al.,* 2011a]. The azimuth of slip direction from CSR RL05 and JPL RL05.1 products is close to that in [*Hayes,* 2010] and that by USGS CMT, while the slip azimuth from GFZ RL05a is about 10° different. As a trial, we also solve for the CMT parameters with location and depth fixed at the GCMT solution. By fixing the centroid location, the estimated slip azimuth is 13° anticlockwise of that in [*Hayes,* 2010], leading to a worse relative difference, 59.5%, compared to the 53.9% from the SA inversion. This test shows that an inaccurate presumed location may affect the solution for the CMT parameters.

Model name	Data Sources	Centroid		Strike (°)	Dip (°)	Rake (°)	Slip azimuth (°)	M_0 in 10^{22} Nm
		Location	Depth					
Hayes, 2010	Seismic waves	Blue beach ball	28.2 km	17	18	107	–91	2.39 (1.22)
GCMT	Seismic waves	**Black** beach ball	23.2 km	19	18	116	–98	1.86
USGS CMT	Seismic waves	Green beach ball	30.0 km	14	19	104	–91	1.81
This study	CSR RL05	Red star and beach ball	20.7 km	9±0.2	26±0.06	99±0.1	–91	2.17±0.006
This study	CSR RL05	Fixed at GCMT	-	346±0.2	25±0.07	90±0.2	–104	1.62±0.005
This study	JPL RL05.1	Yellow star and beach ball	20.7 km	18	26	105	-89	2.6
This study	GFZ RL05a	Magenta beach ball	20.7 km	27	25	106	-81	2.25

Table 4.9. Comparison of Source Parameters.
The $\boldsymbol{M_0}$ in parenthesis, 1.22 $\times 10^{22}$ Nm, is our estimated value from the slip models given by *Hayes* [2010], which is smaller than the published moment for the same slip models due to the smaller shear modulus adopted in our forward modeling software.

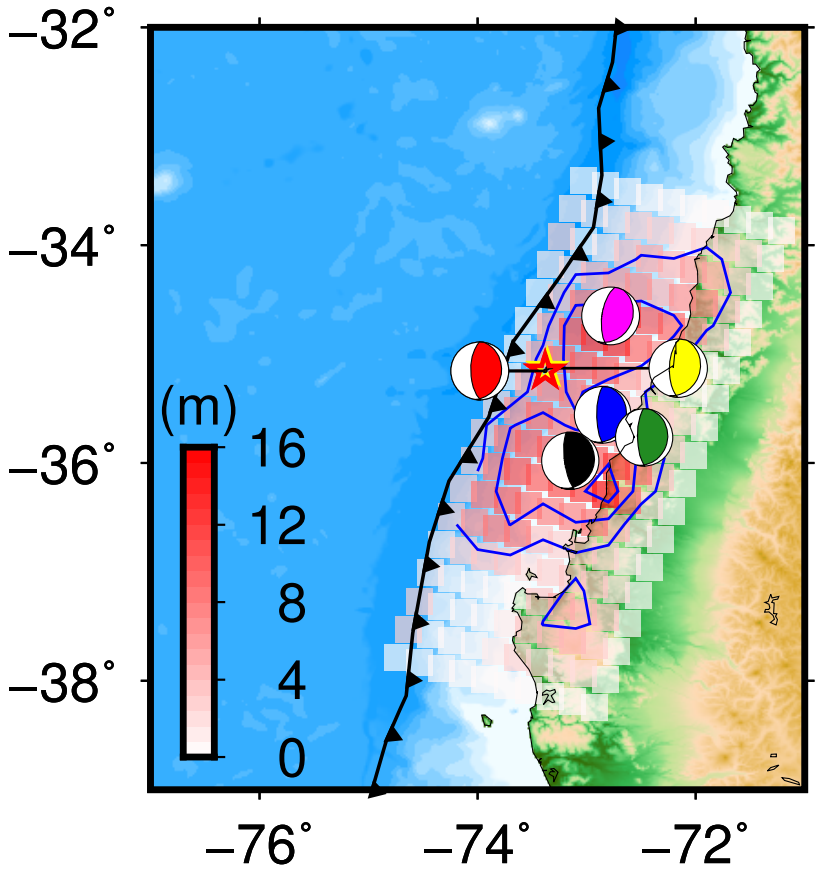

Figure 4.20. Comparison of centroid moment tensor solutions.
The red image overlapped on the topography/bathymetry along the Nazca/South American plate boundary is for the slip model by *Hayes* [2010], with contours represented by the blue lines and CMT denoted by the blue beach ball. Red beach ball is CMT solution from GRACE CSR RL05 product, located at 73.4°W, 35.2°S (red star), with depth as 20.7 km. Yellow star is the location (73.4°W, 35.1°S, 20.7km) of CMT solution (yellow beach ball) from GRACE JPL RL05.1 product, which is almost overlapped by the red star since they are only about 4 km apart. Magenta beach ball is the CMT solution from GRACE GFZ RL05a data product, located at 72.8°W, 34.6°S, with depth as 20.7 km. Other markings are the same as in Figure 4.14. USGS CMT (green beach ball) is from http://earthquake.usgs.gov/earthquakes/eqinthenews/2010/us2010tfan/neic_tfan_cmt.php.

	Strike	Dip	Rake	M_0
Strike	1	0	0.9	–0.2
Dip	0	1	–0.1	0.6
Rake	0.9	–0.1	1	–0.2
M_0	–0.2	0.6	–0.2	1

Table 4.10. The correlation between parameters for SA inversion using CSR RL05 data

4.2.4 The 2012 Indian Ocean earthquakes

The 11 April 2012 Indian Ocean (Mw 8.6 and Mw 8.2) earthquakes ruptured within the Indian Oceanic plate near the India-Australia plate boundary off the west coast of northern Sumatra. These strike-slip earthquakes occurred in the diffuse deformation zone at the India-Australia plate boundary are consistent with the tectonic activities over this region [*McGuire and Beroza,* 2012]. The Australia plate is moving faster northward subducting under the Sunda trench; while the India plate is moving northward at slower rate resisted by the Himalayan front. This differential movement rate of about 1cm/year along south-north direction results in the detachment of the Australia plate from the India plate [*Delescluse et al.,* 2012]. The mainshock of Mw 8.6 is the largest strike-slip earthquake on record [*Delescluse et al.,* 2012; *McGuire and Beroza,* 2012; *Meng et al.,* 2012; *Royer,* 2012; *Yue et al.,* 2012], and the aftershock occurred just two hours later with the magnitude of Mw 8.2. These large intraplate strike-slip earthquakes raise debates about the depth for strike-slip faulting [*McGuire and Beroza,* 2012; *Meng et al.,* 2012], as well as discussions on whether it is dominated by east-west right-lateral slips [*Meng et al.,* 2012; *Yue et al.,* 2012; *Yadav et al.,* 2013] or meridian-aligned left-lateral slips [*Delescluse et al.,* 2012; *Shao et al.,* 2012].

Because of its remote offshore location, the geodetic constraints on the static fault geometry are limited [*Meng et al.,* 2012]; thus only seismological data are used to invert

for the focal mechanisms. Although there are some remote GPS stations accessible at about 500-1200 km north of faults, they are only used for the detection of coseismic displacements and validation of the slip model by seismic data [*Yadav et al.,* 2013]. Hence, GRACE data become an important source of independent constraint on the coseismic static deformation. Although the gravity change for vertical strike-slip earthquakes is expected to be small, we show that the coseismic gravity change from GRACE is still considerable, up to –5.7±0.7 μGal for g_N and 0.26±0.03 mE for *Txz*. In this section, we present the source parameters resolved from the coseismic g_N, *Txx*, *Txy*, *Txz* change derived from CSR RL05 monthly geopotential solutions.

Three products are used to estimate the coseismic gravity and gravity gradient change. The first product is generated by *Shang et al.* [2015] using the improved energy integral approach [*Guo et al.*, 2015; *Shang et al.*, 2015], denoted as OSU product, which includes 124 monthly solutions from January 2003 to December 2013. The second product is the 137 monthly solutions from CSR RL05 NMAX 60 product from April 2002 to September 2014. The third product is 137 monthly solutions from GFZ RL05a NMAX 90 product from April 2002 to August 2014. All solutions are truncated to degree 40 based on the localized spectral analysis and the signal's spatial pattern. The RMS of the difference between GRACE-estimated g_N, *Txx, Txy, Txz* and model prediction are evaluated as shown in Table 4.12, where the model is the GRACE-inverted CMT solution using each data product, with centroid location fixed at GCMT solution. It shows that GFZ RL05a gives the worst RMS, while the CSR RL05 and OSU product produce the similar small RMS. In addition, we try the case of estimating only two coseismic jumps for CSR RL05 product and neglecting the jump at the 2007 Bengkulu earthquake,

since the 2007 Bengkulu earthquake has smaller seismic moment and its fault area is relatively further apart. However the RMS of this case is shown to be slightly worse than the case of considering the three coseismic jumps simultaneously. Here, we choose to show the results for the CSR RL05 product using least-squares adjustment for three coseismic jumps.

The cumulative slip model composed of the complex four-fault slip model by *Yue et al.* [2012] for the Mw 8.6 mainshock and the GCMT solution of the Mw 8.2 aftershock are adopted to predict the gravity and gravity gradient change. Since *Yue et al.*'s slip model (http://equake-rc.info/media/srcmod/_fsp_files/s2012SUMATR01YUEx.fsp) gives coordinates for top-center of each subfault, it is necessary to be converted to the left top point of each patch [*Freymueller et al.,* 2014] to be consistent with the forward modeling PSGRN/PSCMP software. The 1-D velocity model is interpolated by estimating the mean velocity model from CRUST 2.0 model over the fault area. The average ocean thickness over the fault area is 4.0 km. The upward continuation of gravity change from ocean floor (with the radius as 6374085.221 m) to Earth's semi-major axis is considered. The effect of ocean response for gravity change is significant, the same magnitude of that from solid earth. The gravity and gravity gradient up to degree 40 corresponding to the finite slip model [*Yue et al.,* 2012] are then computed.

Layer	Vp [km/s]	Vs [km/s]	Density [kg/m^3]	Thickness [km]
Ocean	1.5	0	1020	4.0156
Soft sediment	2.24	1.07	2169	1.2878
Hard sediment	3.2	1.6	2300	0.3171
Upper Crust	5	2.5	2600	1.7
Middle Crust	6.6	3.65	2900	2.3
Lower Crust	7.1	3.9	3050	2.5
Mantle	8.15	4.65	3350	-

Table 4.11. Earth Model from CRUST 2.0.

RMS of the residual	**g_N (μGal)**	***Txx* (mE)**	***Txy* (mE)**	***Txz* (mE)**
OSU	**0.77**	**0.024**	**0.017**	**0.030**
CSR RL05	**0.76**	**0.024**	**0.017**	**0.032**
CSR RL05*	**0.88**	**0.030**	**0.018**	**0.037**
GFZ RL05a	**1.01**	**0.028**	**0.023**	**0.037**

Table 4.12. Comparison of different GRACE products.
CSR RL05* use the CSR RL05 product, but different fitting model for the time series. Instead of estimating three coseismic jumps like the other three cases, this case only estimate two jumps corresponding to the 2004 Sumatra-Andaman and 2005 Nias earthquakes and the 2012 Indian Ocean earthquakes.

The localized spectral analysis is first carried out to evaluate the signal and noise level of GRACE-derived gravity and gravity gradient change. As shown in Figure 4.22, the GRACE-observed g_N, *Txx, Txz* change agrees well with the model prediction with slightly larger amplitude up to degree 55. While the localized degree variance of *Txy* change goes up since degree 45 and that for g_E and g_D change goes straight up since around degree 25. Guided by the localized spectral comparison, we use only the north component of gravity and gravity gradient change up to degree 40 to study the coseismic signal.

As shown the Figure 4.23, the GRACE-derived g_N change agrees well with the cumulative slip model prediction in spatial pattern and signal magnitude. The peak g_N change is at 88.4°E, 3.45°N about –5.7±0.7 μGal (Figure 4.23a), slightly larger to the model prediction at the same location, –3.7 μGal. The smaller magnitude for the model prediction is consistent with the smaller seismic moment M_0 (9.53×10^{21} Nm) compared to the GRACE-resolved M_0 (10.13×10^{21} Nm). Similar characteristic goes to the north component of gravity gradient change, which is up to 0.26±0.03 mE at 88.6°E, 3.35°N for *Txz*, slightly larger than the model-predicted 0.18 mE. All three components of the north component of gravity gradient change have the comparable spatial pattern with the slip model prediction.

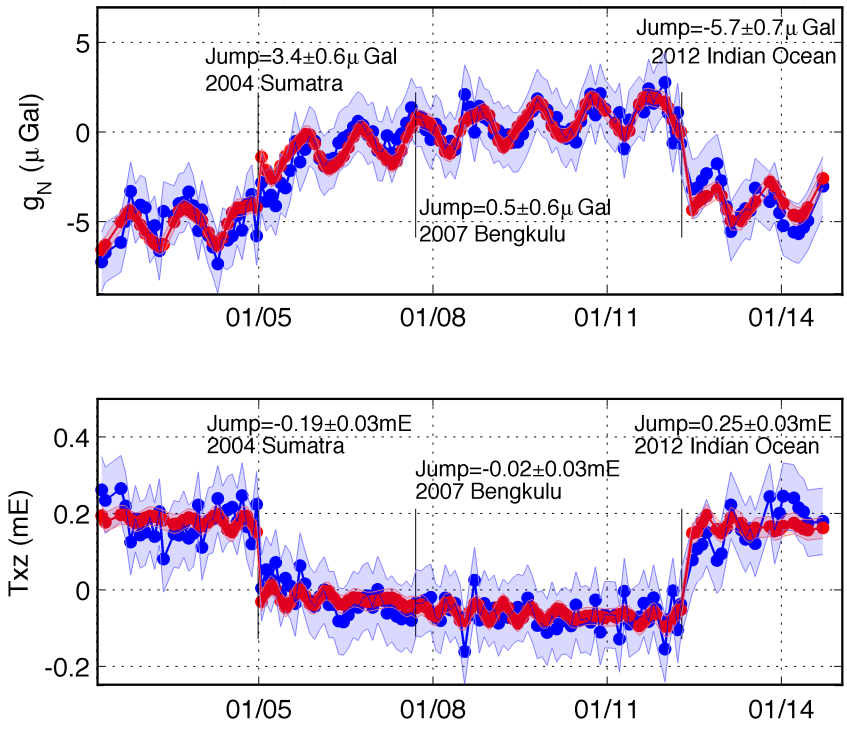

Figure 4.21. Time series of g_N, *Txz* at 88.4°E 3.45°N.
Blue lines are the g_N (top), *Txz* (bottom) disturbance generated from 137 monthly CSR RL05 solutions up to degree 40 from April 2002 to September 2014. The blue shadings are uncertainties propagated from the estimated a posteriori variance of unit weight for each coefficient. The red lines are the fitted value using linear trend, periods, and Heaviside step functions.

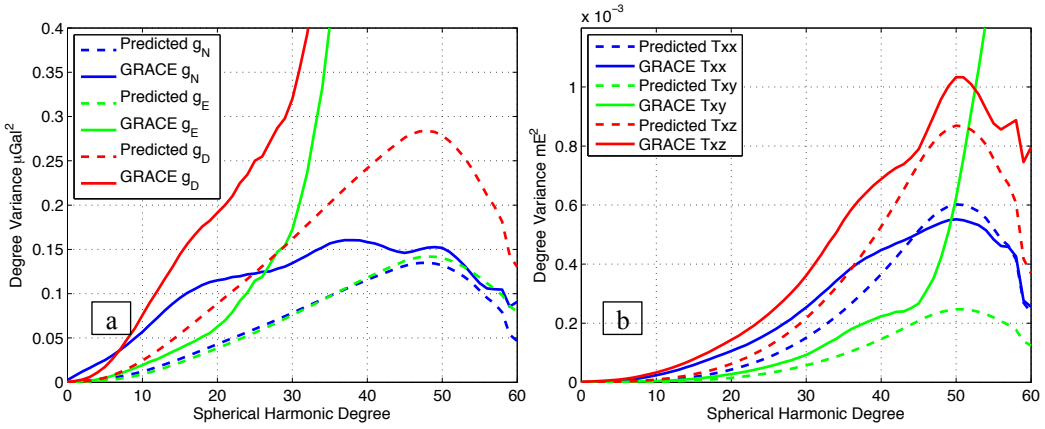

Figure 4.22. Comparison in the spectral domain.
The localized degree variance as a function of spherical harmonic degree is shown for the observed and model-predicted g_N, g_E, g_D change (a), and *Txx*, *Txy*, *Txz* change (b).

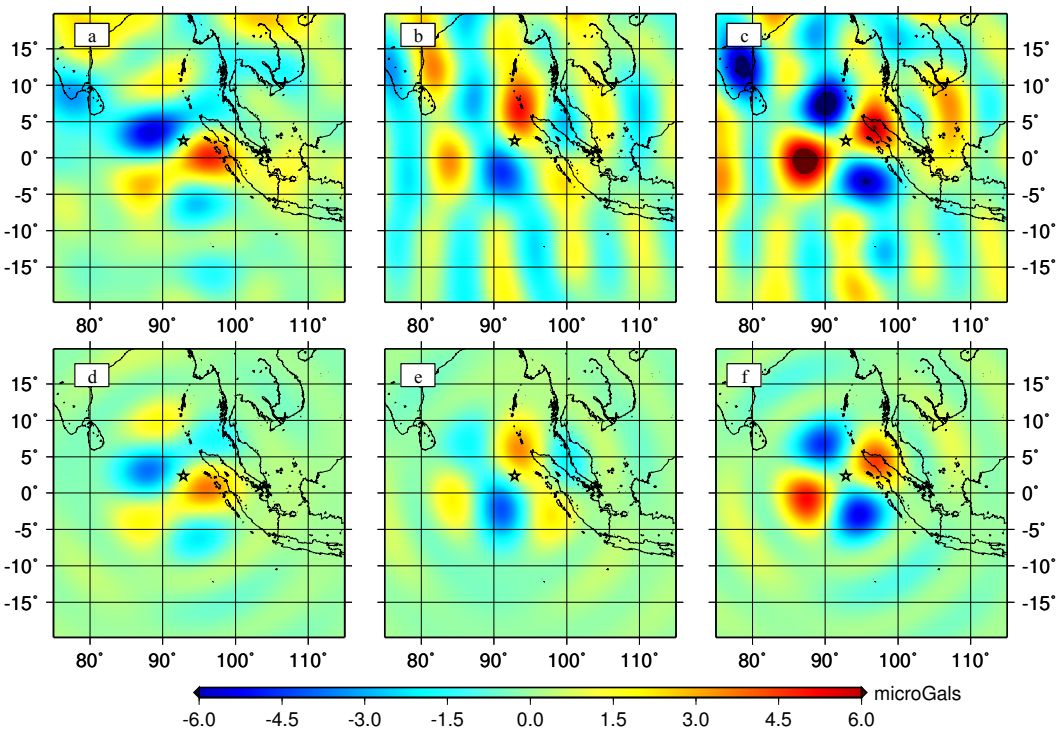

Figure 4.23. Comparison of GRACE-observed and model-predicted coseismic gravity changes up to degree 40.
(a) ~ (c): GRACE-observed g_N (a), g_E (b), g_D (c) change. (d) ~ (f): Coseismic-model-predicted g_N (d), g_E (e), g_D (f) change. The black star is the GCMT centroid (92.82°E, 2.35°N).

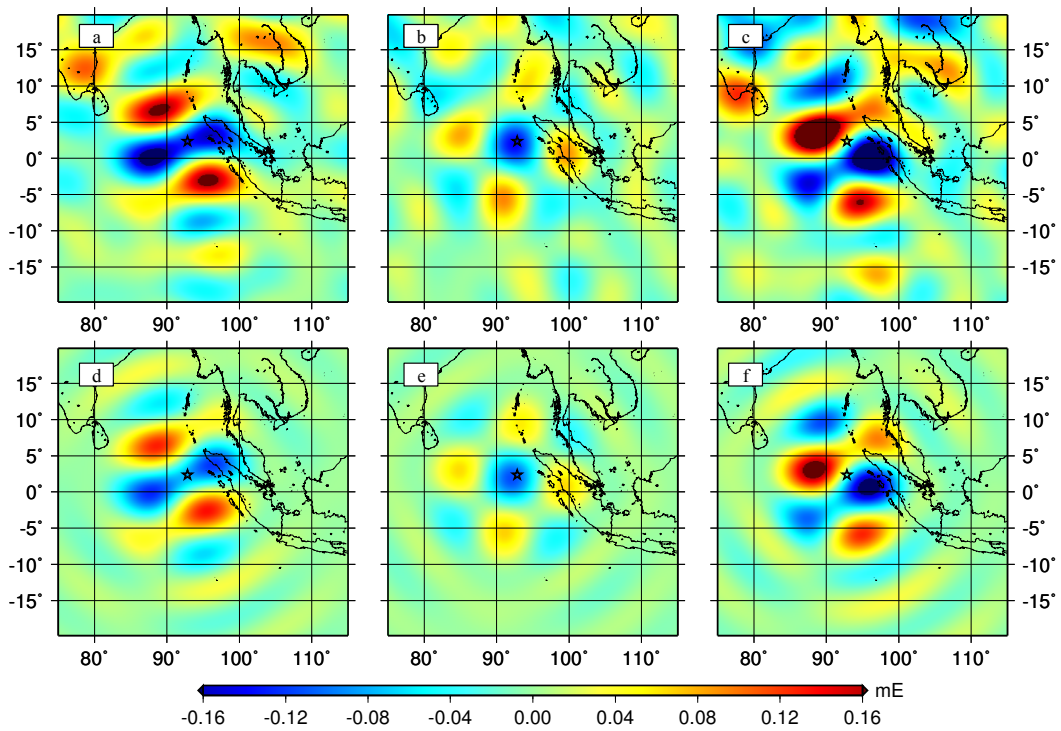

Figure 4.24. Comparison of GRACE-produced and model-predicted gravity gradient change up to degree 40.
(a) ~ (c): GRACE-produced *Txx* (a), *Txy* (b), *Txz* (c) change. (d) ~ (f): Coseismic-model-predicted *Txx* (d), *Txy* (e), *Txz* (f) change. The black star is the GCMT centroid.

As discussed above, three products are all carried out to solve for the source parameters with centroid location fixed at GCMT solution. The CMT parameters agree amazingly well within these three products, especially for strike angle. The rake angle also has the small variation of only 1-2°, while a slightly larger divergence for moment and dip angle are shown by the smaller value given by OSU product.

McGuire and Beroza [2012] point out that the centroid depths (more than 40 km) of the two shocks are too large to be explained by the frictional failure theory in oceanic lithosphere, rather to be explained by the thermal runaway mechanism. Analysis in [*Meng et al.,* 2012] also indicates a deeper source in oceanic lithosphere. The depth

resolved in [*Yue et al.,* 2012] using broadband teleseismic waves and the surface waves is shallower with slips mainly distributed at the thin oceanic crust and uppermost mantle layer, giving the centroid depth at around 26.4 km. In this study, we fixed the centroid depth at the GCMT depth of 45.6 km.

The solved M_0 (10.13×10^{21}Nm) from CSR RL05 product, the cumulative moment for both the mainshock and the aftershock, is close to the other published values. The M_0 is slightly smaller than the cumulative M_0 by GCMT solution (12.03×10^{21}Nm), USGS CMT solution (10.7×10^{21}Nm, http://earthquake.usgs.gov/earthquakes/eqinthenews/2012/usc000905e/neic_c000905e_cmt.php), and the published moment of the cumulative slip model (16.79×10^{21}Nm). Our dip angle is also consistent with the dip angle given by other solutions, just about 4-5° smaller. As shown in Table 4.14, the correlation between dip and moment is about zero for this vertical strike-slip source, indicating the independency of the estimated dip angle and moment.

The rupture process of these intraplate earthquakes over the diffuse deformation zone is very complicated, and it raises discussions on whether it is dominated by east-west right-lateral slips [*Meng et al.,* 2012; *Yue et al.,* 2012; *Yadav et al.,* 2013] or meridian-aligned left-lateral slips [*Delescluse et al.,* 2012; *Shao et al.,* 2012]. Numerous preliminary results characterize the fault as a meridian-aligned left-lateral strike-slip [*Shao et al.,* 2012], which is consistent with the nearly north-south orientation of fracture zones of magnetic anomalies [*Yadav et al.,* 2013] and gravity anomalies data [*Delescluse et al.,* 2012] and can be explained by the northwest-southeast compression due to the relative northward movement between Australia plate and India plate [*Delescluse et al.,* 2012; *Yadav et al.,* 2013]. These meridian-aligned left-lateral slips are also theoretically predicted by the

inferred Coulomb stress change distribution assuming these strike-slip earthquakes are induced by the stress change following the 2004 Sumatra and 2005 Nias earthquakes [*Delescluse et al.,* 2012]. Nevertheless, the back projection source imaging from seismic data shows that the rupture of faults is dominated by east-west right-lateral slip [*Meng et al.,* 2012; *Yue et al.,* 2012], which might be explained by the enhanced slab pull force on the Australia plate at the Sunda trench [*Delescluse et al.,* 2012; *Yue et al.,* 2012]. The east-west right-lateral slip model is further validated by the consistency with the remote offshore GPS offsets [*Yadav et al.,* 2013]. Coherent with the fault plane by *Yue et al.* [2012], the GRACE-solved CMT also indicates an east-west right-lateral strike slip with strike angle as 292°. The reason why the strike angle by GRACE and GCMT solution is about 180° larger than that by *Yue et al.* [2012] and USGS CMT solution is that, for this nearly vertical strike-slip source, the dip direction is almost vertical and it is slightly tilted toward north for the former solutions and toward south for the latter as shown in Figure 4.25. Taking into consideration of this 180° difference, GRACE-solved slip direction is amazingly consistent with the slip azimuth by other data, only 1-2° different from the GCMT and USGS CMT solutions and 5° different from the cumulative model.

Model name		Data Sources	Centroid		Strike (°)	Dip (°)	Rake (°)	Slip azimuth (°)	M_0 in 10^{21} Nm
			Location	Depth					
Yue et al., 2012	Mainshock Mw 8.6	Seismic waves	-	26.4 km	108	85	184		13.9 (6.64)
GCMT	Aftershock Mw 8.2	Seismic waves	-	54.7 km	107	83	183		2.89
Cumulative model (*Yue et al.*, 2012 & GCMT)		Seismic waves	Blue star and beach ball	30.9 km	107	85	184	287	16.79 (9.53)
GCMT (for mainshock)		Seismic waves	**Black** star and beach ball	45.6 km	289	85	166	110	9.14 +2.89
USGS CMT (for mainshock)		Seismic data	Green star and beach ball	40.0 km	109	84	165	291	8.5 +2.2
This study		OSU	Fixed	45.6 km (F)	292	74	177	113	9.62
This study		CSR RL05	Fixed	45.6 km (F)	292± 0.04	80± 0.09	178± 0.06	112	10.11± 0.01
This study		CSR RL05*	Fixed	45.6 km (F)	292	82	182	112	10.08
This study		GFZ RL05a	Fixed	45.6 km (F)	292	79	179	112	10.09

Table 4.13. Comparison of Source Parameters.
The additional seismic moment $\boldsymbol{M_0}$ in Orange color is for the aftershock (Mw 8.2) that occurred two hours after the mainshock (Mw 8.6); The GCMT solution is available at http://www.globalcmt.org and the USGS CMT solution for the aftershock is from http://earthquake.usgs.gov/earthquakes/eqinthenews/2012/usc00090da/neic_c00090da_cmt.php. The $\boldsymbol{M_0}$ in parenthesis, 6.64×10^{21} Nm, is our estimated value from the slip models given by *Yue et al.* [2012], which is smaller than the published moment for the same slip models due to the smaller shear modulus (30 GPa) adopted in our forward modeling software. CSR RL05* is the same as in Table 4.12.

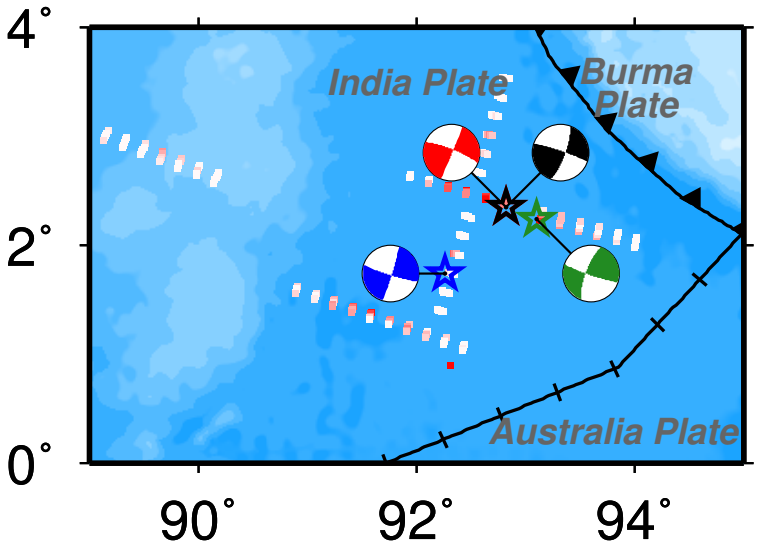

Figure 4.25. Comparison of centroid moment tensor solutions.
The white/red dot is the fault patches projected to the Earth's surface for the cumulative slip model by *Yue et al.* [2012] for mainshock and GCMT solution for aftershock, with its CMT located at the blue star and represented by the blue beach ball. Red beach ball is CMT solution from GRACE CSR RL05 data, fixed at the GCMT location (**black** star). Other markings are the same as in Figure 4.14.

	Strike	Dip	Rake	M_0
Strike	1	0.2	0.2	0
Dip	0.2	1	0.4	0
Rake	0.2	0.4	1	0
M_0	0	0	0	1

Table 4.4.14. The correlation between parameters for SA inversion.

4.2.5 The 2007 Bengkulu earthquake

The 12 September 2007 Bengkulu earthquake (Mw 8.5) occurred off the west coast of Bengkulu, Indonesia [*Konca et al.,* 2008; *Borrero et al.,* 2009; *Gusman et al.,* 2010]. It ruptured the plate interface at the Sumatra subduction zone where the Australia plate is subducting beneath the Sunda plate, with the strike angle parallel to the Sunda trench.

The relatively small seismic moment of this event renders it to be by far the smallest earthquake detectable by GRACE data. To crosscheck the reliability of the coseismic signal, three products for GRACE data are used to estimate the gravity and gravity gradient change corresponding to this 2007 Bengkulu earthquake. The first product is generated by *Shang et al.* [2015] using the improved energy integral approach [*Guo et al.*, 2015; *Shang et al.*, 2015], denoted as OSU product, which includes 124 monthly solutions from January 2003 to December 2013. The second product is the 137 monthly solutions from CSR RL05 NMAX 60 product from April 2002 to September 2014. The third product is 137 monthly solutions from GFZ RL05a NMAX 90 product from April 2002 to August 2014. All solutions are truncated to degree 40 based on the localized spectral analysis. The RMS of the model-data misfit for g_N, *Txx, Txy, Txz* are evaluated as shown in Table 4.16, where the model is the GRACE-inverted CMT parameters for each product. OSU product seems to give the lowest noise level with the smallest RMS, while GFZ RL05a product gives the worst model-data misfit. Considering the comparison of the residual RMS as well as the comparison in spatial domain, we choose to present the gravity and gravity gradient change from OSU GRACE data product.

The slip distribution model by *Konca et al.* [2008] is used to model the GRACE-commensurable gravity and gravity gradient change. This published slip model (http://www.tectonics.caltech.edu/slip_history/2007_s_sumatra/ssumatra-update.html) is the joint inversion of teleseismic waveforms, GPS and InSAR data. Fault patch's location is given on the center of each patch, so it is converted to the left top point to be consistent with the forward modeling PSGRN/PSCMP software. The earth model is interpolated from the CRUST2.0 model as displayed in Table 4.15. The average ocean thickness over

the fault area is 1.3 km. The upward continuation of gravity change from ocean floor (with the radius as 6376758.506 m) to Earth's semi-major axis is considered. The effect of ocean response for gravity change is about 46% of that from solid earth. The gravity and gravity gradient up to degree 40 corresponding to the finite slip model [*Konca et al.,* 2008] are then computed.

Layer	Vp [km/s]	Vs [km/s]	Density [kg/m^3]	Thickness [km]
Ocean	1.5	0	1020	1.285
Soft sediment	2.209	1.053	2081.8	0.824
Hard sediment	3.905	2.038	2390.3	0.295
Upper Crust	5.901	3.3	2691.6	6.360
Middle Crust	6.6	3.694	2900	6.371
Lower Crust	7.188	3.988	3072	6.434
Mantle	8.156	4.656	3370	-

Table 4.15. Earth Model from CRUST 2.0

The localized degree variance shows the consistency and the difference between GRACE-derived and model-predicted gravity and gravity gradient change. From Figure 4.27, we can see that the g_N has lower noise level compared to g_E, g_D change as always. Nevertheless, the difference between the GRACE-observed and model-predicted g_N is still large for both the low degree part and high degree part, which indicates the GRACE noise level is relatively high for this comparatively small earthquake. For the north component of gravity gradient change, the GRACE-derived *Txx, Txy, Txz* change agrees with the model prediction with larger magnitude for degree below 50. With additional comparison in spatial domain by different maximum truncation degree, we choose to use the spherical harmonic coefficients below 40 to solve for fault mechanisms. As shown in Figures 4.28 and 4.29, the spatial pattern of the GRACE-derived gravity and gravity

gradient change for north components has good consistency with the model prediction. The g_N change is up to 1.7±0.2 μGal (Figure 4.28) three times larger than the model prediction, 0.5 μGal, and *Txz* change is up to 0.09±0.01 mE at 101.4°E, 1.95°S, twice of the model-predicted 0.04 mE. The smaller magnitude of the model prediction is consistent with the approximately in half underestimated seismic moment for the given slip model as shown in Table 4.17. Nevertheless, the surrounding noise is relatively high for this small earthquake, as also indicated in the localized spectral analysis. For example, for the g_N change (Figure 4.28a), there is an abnormal positive signal west coast of North Sumatra, which is absent in the model prediction (Figure 4.28d). Similarly, over the same region, there is uncategorized negative signal for *Txz* (Figure 4.29c) change. Due to this large surrounding noise, it is not suggested to solve for the source location since the noise can be mistakenly treated as a signal and produce wrong source parameters.

RMS of the residual	g_N (μGal)	*Txx* (mE)	*Txy* (mE)	*Txz* (mE)
OSU	0.50	0.016	0.016	0.022
CSR RL05	0.54	0.017	0.015	0.023
GFZ RL05a	0.69	0.023	0.017	0.029

Table 4.16. Comparison of different GRACE products.

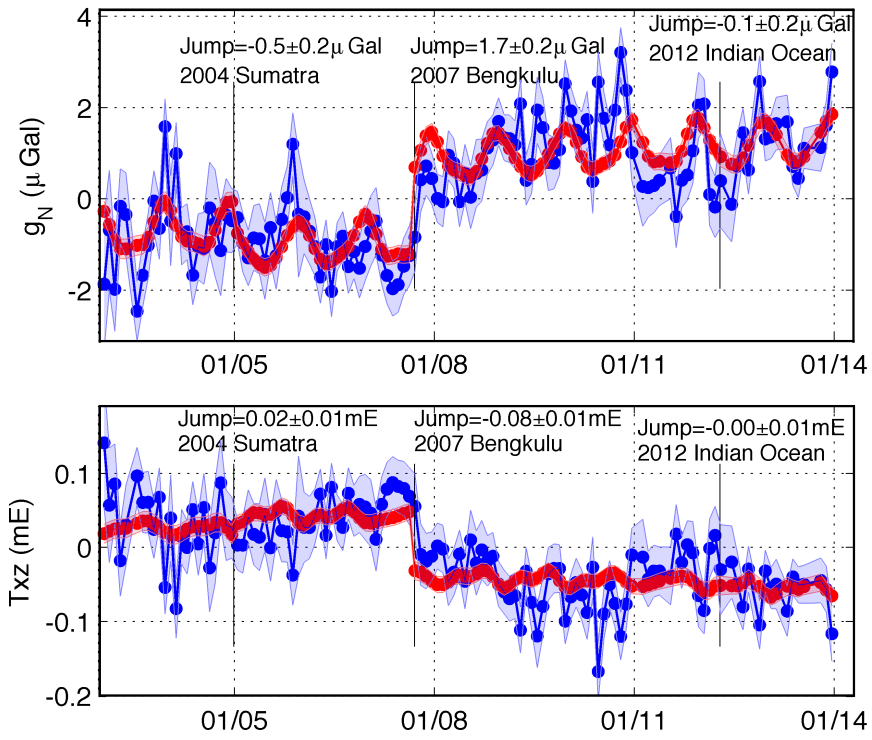

Figure 4.26. Time series of g_N, *Txz* at 100.6°E 7.95°S.
Blue lines are the g_N (top), *Txz* (bottom) disturbance generated from 124 monthly OSU gravity field solutions up to degree 40 from January 2003 to December 2013. The blue shadings are uncertainties propagated from the formal error of each coefficient. The red lines are the fitted value using linear trend, periods, and Heaviside step functions.

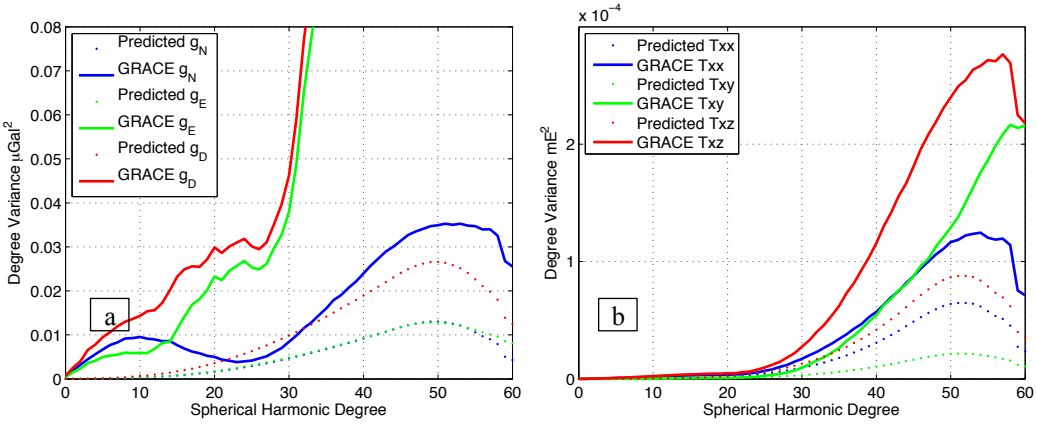

Figure 4.27. Comparison in the spectral domain.
The localized degree variance as a function of spherical harmonic degree is shown for the observed and model-predicted g_N, g_E, g_D change (a), and *Txx*, *Txy*, *Txz* change (b).

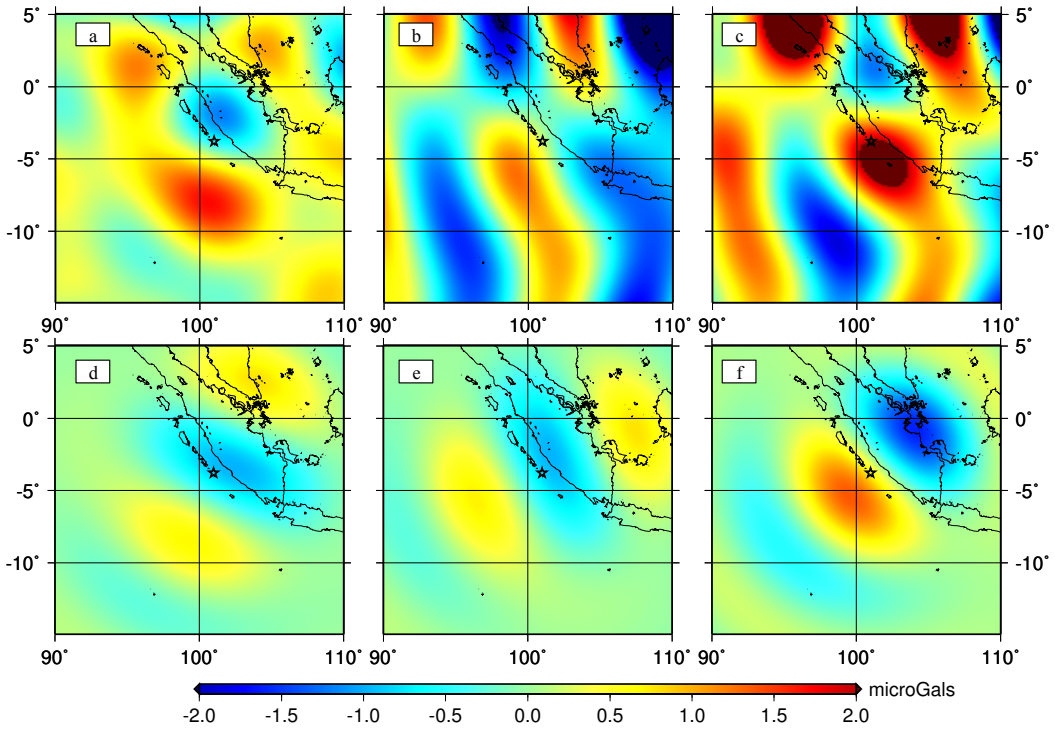

Figure 4.28. Comparison of GRACE-observed and model-predicted coseismic gravity changes.
(a) ~ (c): GRACE-observed g_N (a), g_E (b), g_D (c) change. (d) ~ (f): Coseismic-model-predicted g_N (d), g_E (e), g_D (f) change. The black star is the GCMT centroid (100.99°E, 3.78°S).

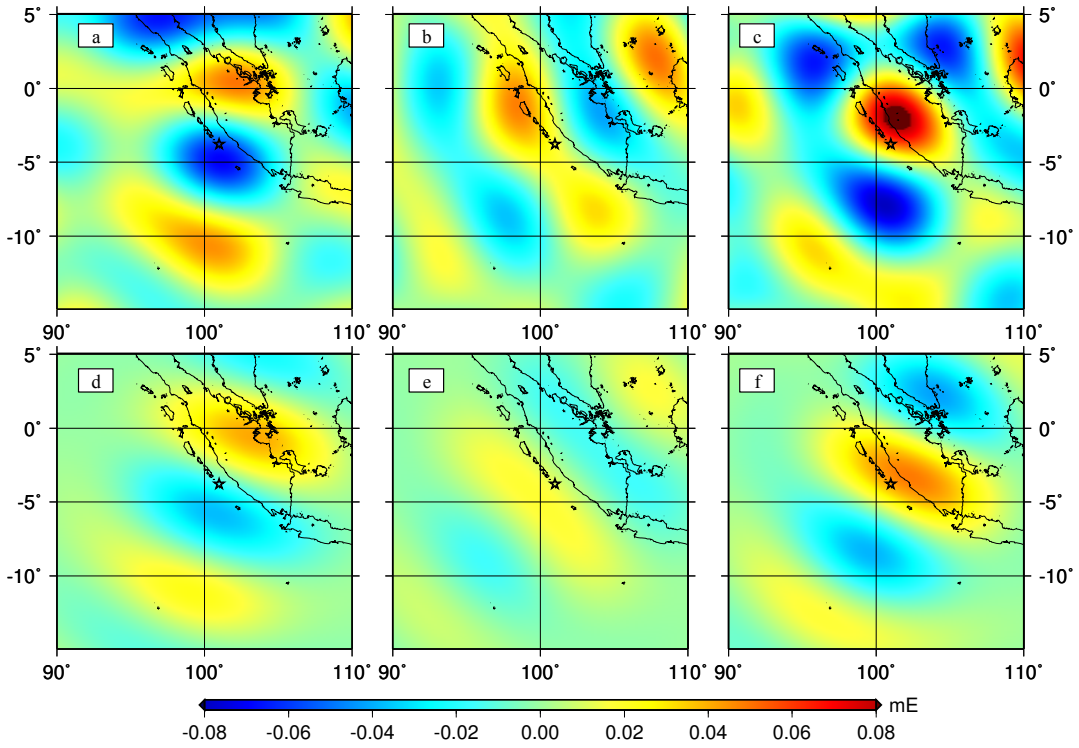

Figure 4.29. Comparison of GRACE-produced and model-predicted gravity gradient change.
(a) ~ (c): GRACE-produced *Txx* (a), *Txy* (b), *Txz* (c) change. (d) ~ (f): Coseismic-model-predicted *Txx* (d), *Txy* (e), *Txz* (f) change. The black star is the GCMT centroid.

As discussed above, due to the large surrounding noise, we choose only to solve for the centroid moment tensor while fix the centroid location at the GCMT solution. All three products are used for the inversion. We can see that the divergence for three angles form the three products is large, e.g. the difference is up to 11° for strike angle, 10° for dip angle, and 36° for rake angle. This larger variation for the solved source parameters, compared to the case for the 2012 Indian Ocean earthquakes, indicates again that the noise level from GRACE data is relatively high for this magnitude Mw 8.5 earthquake. Hence the large variation should be considered when interpret the GRACE-inverted

source angles. Nevertheless, the self-consistency for the seismic moment is good from these three products of GRACE data.

For the seismic moment, GRACE-inverted M_0 from all three products is systematically smaller than that from GCMT solution (6.71×10^{21}Nm) and that (4.47×10^{21}Nm) in [*Konca et al.,* 2008], with GFZ RL05a producing the closest M_0 (4.16×10^{21}Nm) to that in [*Konca et al.,* 2008]. The GRACE-solved dip angle is larger than the published values, with the closest dip angle as 18° from CSR RL05 product. Considering the trade-off relationship between M_0 and dip angle, larger dip angle indicates smaller moment, further improving the consistency of GRACE-estimated M_0 with the published values. During the three products, the OSU product produces the closest strike and rake angles with other results, e.g. rake angle (108°) is in-between the value given by GCMT and *Konca et al.* [2008] and it's only 2° larger than the rake angle by the joint inversion using tsunami waveforms and InSAR data in [*Gusman et al.,* 2010]; but the strike angle is about 20° smaller causing the at least 16° smaller slip azimuth. On the other hand, the slip azimuth from CSR RL05 and GFZ RL05a is consistent with the slip azimuth by GCMT and *Konca et al.* [2008], but the individual strike and rake angle are about 20~30° smaller.

Model name	Data Sources	Centroid		Strike (°)	Dip (°)	Rake (°)	Slip azimuth (°)	M_0 in 10^{21} Nm
		Location	Depth					
Konca et al., 2008	GPS, SAR, Teleseismic data	Blue beach ball	36 km	324	15	99	225	4.47 (2.39)
GCMT	Seismic waves	**Black** beach ball	24.4 km	328	9	114	214	6.71
This study	OSU	Red beach ball	24.4 km	308	28	108	198	3.09
This study	CSR	-	24.4 km	299	18	72	228	3.16
This study	GFZ RL05a	-	24.4 km	297	28	80	218	4.16

Table 4.17. Comparison of Source Parameters.
The $\boldsymbol{M_0}$ in parenthesis, 2.39×10^{21} Nm, is our estimated value from the slip models given by *Konca et al.* [2008], which is smaller than the published moment for the same slip models due to the smaller shear modulus adopted in our forward modeling software.

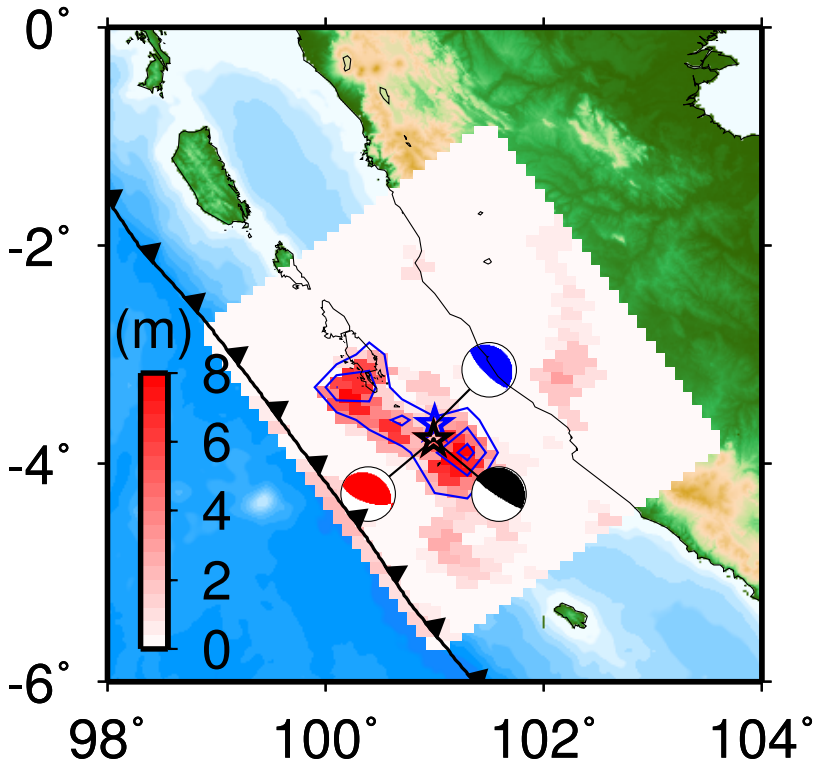

Figure 4.30. Comparison of CMT solutions.
The white/red 2D map and blue slip contours are for the slip distribution model [*Konca et al.*, 2008] at the Sunda/Australia plate boundary, with its CMT located at the blue star and represented by the blue beach ball. Red beach ball is CMT solution from GRACE data (OSU product). Other markings are the same as in Figure 4.14.

Chapter 5. Conclusions

Innovative GRACE data processing is developed in this study by conducting the localized spectral analysis and by using the north component of gravity and gravity gradient change. The Heaviside step function is applied to isolate coseismic jump from the time series of gravity and gravity disturbance over the fault region. This method of direct analysis on the regional gravity time series can reduce the effect from the long-term trend of gravity variation, the seasonal variations, and the random noise. The localized spectral analysis is used as an efficient method for guiding the truncation of the maximum spherical harmonic degree for high degree solutions, as well as evaluating the noise level of each component of gravity and gravity gradient change. The new approach of using only the north component of gravity and gravity gradient change from GRACE geopotential solutions is shown to have the advantage of reducing south-north stripes and preserving high-degree signals in GRACE L2 products, leading to improved spatial resolution to the extent possible. The benefit of these north components in the way of preserving high degree signals and reducing stripes is demonstrated in both the spectral domain and the spatial domain. The north component of gravity and gravity gradient change can suppress the south-north stripes because GRACE KBR measurement is highly sensitive to g_N change but relatively insensitive to g_E, g_D changes due to the orbit configuration of the two satellites. Another way to explain the suppression on the south-north stripes is from the equation of the north component of gravity and gravity gradient

change, which reduces the stripes by the derivative of disturbing potential along the meridian direction.

In this study, we show the linear relationship between the surface displacement and north component of gravity and gravity gradient change with the seismic moment tensor. The design matrix of this linear algorithm is realized based on the output of Wang's PSGRN/PSCMP software. By establishing the observation model for gravity change and surface displacement as a linear function of the double-couple moment tensor, the point source parameters are resolved through the least-squares adjustment. Considering that the coseismic deformation and gravity change is a non-linear function of the centroid depth and location, the simulated annealing algorithm is applied to solve for the location. This inversion method is validated through simulation to evaluate its accuracy and viability. The comparison of source parameters inverted from simulated GPS data and GRACE data and their combination is analyzed to demonstrate the distinctive constraint from different data sets, and to show the contribution of GRACE data on offshore seismic deformation. The inversion from simulated GRACE data shows larger errors for the east and down components of moment tensor (M_{yz}, M_{zz}), and the inversion from simulated GPS data tend to produce worse precision for M_{xz}, M_{yz} component, which implies that GRACE data and GPS data can compensate each other on the constraint of moment tensor. The combination of GRACE and GPS data gives a better precision for each component of source parameters. In addition, the joint solution significantly reduces the correlation between dip angle and seismic moment compared to the solution by GRACE data only or the solution by GPS data only.

Sensitivity of GRACE data over offshore seismic deformations is illustrated by simulation, as well as by the comparison of slip models from real data inversion. First, to test the influence of the GPS stations' spatial distribution, the simulation using GPS data excluding the five seafloor sites is carried out, showing that the precision got worsen badly with the standard deviation of the inverted source parameters increased for about one order of magnitude. Without the offshore displacement data, the centroid location inverted using SA algorithm from onshore GPS data has much larger error (1km) along the east-west direction, ten times of the error along the north south direction, explained by the lack of stations along the east-west direction of the source. By measuring right above the fault area, GRACE data can proved good constraint on centroid locations, and it can overcome the inadequacy caused by the poor configuration of GPS stations as shown by the small errors (0.1km) along all three directions for GRACE-only inversion. On the other hand, the comparison between the GRACE-estimated fault model with the two GPS slip models is illustrated to show the offshore constraint from GRACE data. Compared to the two slip models given by *Wang et al.* [2013], GRACE-estimated slip model is closer to Model 1 that is resolved using both onshore and offshore GPS data than Model 4 which used only onshore GPS data, indicating that GRACE data independently contain reliable signal over the offshore area.

The GRACE-inverted source parameters generally agree well with the slip models estimated using other data sets, including seismic, GPS, or combined data. For the 2004 Sumatra-Andaman and 2005 Nias earthquakes, GRACE data infer a shallower centroid depth (9.1 km), which may be explained by the closer-to-trench centroid and by the aseismic slip over the shallow region. For the 2011 Tohoku earthquake, GRACE-

estimated centroid location and slip azimuth from two different GRACE data products and two different forward modeling are consistent with each other, demonstrating the coherence of the CSR RL05 NMAX 60 and CSR RL05 NMAX 96 products, as well as the coherence of the finite fault modeling and the point-source moment tensor modeling. The slip direction from GRACE data shows a clockwise rotation compared to the slip direction by GPS and seismic waves data, which is also observed by GOCE measurements [*Fuchs et al.*, 2013]. The centroid location inverted from GRACE data for the 2011 Tohoku and 2010 Maule, Chile earthquakes are both westwards of other solutions, which might be caused by systematic errors from GRACE data. The GRACE-estimated dip angles are larger than that from GPS/seismic data, about 18° larger for the 2004 Sumatra-Andaman and 2005 Nias earthquakes, about 8° larger for the 2010 Maule, Chile earthquake, and about 3~20° larger for the 2007 Bengkulu earthquake. These differences potentially show the additional offshore constraint from GRACE data, compared to GPS/seismic data.

The strong correlation between strike and rake angle is presented for the small-dip thrust earthquakes. Hence, the slip azimuth is better constraint from GRACE data compared to the strike and rake angle individually. This correlation between strike and rake angle is significantly reduced for the vertical strike-slip earthquakes. The correlation between dip and moment for the vertical strike-slip earthquakes is also much smaller than that for small-dip earthquakes. In addition, the correlation between dip angle and seismic moment is also significantly reduced in the joint solution of GRACE and GPS data.

References

Aki, K., and P. G. Richard (2002), Quantitative Seismology, second edition, *University Science Books*, Sausalito, California.

Alterman, Z., H. Jarosch, C. Pekeris (1959), Oscillations of the Earth, *Proc. Roy. Soc. London, A,* 252, 80–95.

Amante, C., and B. W. Eakins (2009), ETOPO1 1 Arc-Minute Global Relief Model: Procedures, Data Sources and Analysis, NOAA Technical Memorandum NESDIS NGDC-24, 19 pp, March 2009.

Ammon, C. J., C. Ji, H. K. Thio, D. Robinson, S. D. Ni, V. Hjorleifsdottir, H. Kanamori, T. Lay, S. Das, D. Helmberger, G. Ichinose, J. Polet, and D. Wald (2005), Rupture process of the 2004 Sumatra-Andaman earthquake, *Science*, 308, 1133–1139.

Ammon, C. J., T. Lay, H. Kanamori, and M. Cleveland (2011), A rupture model of the 2011 off the Pacific coast of Tohoku Earthquake, *Earth Planets Space*, 63, 693–696.

Banerjee, P., F. Pollitz, and R. Bürgmann (2005), Size and duration of the great 2004 Sumatra-Andaman earthquake from far-field static offsets, *Science*, 308, 1769–1772.

Banerjee, P., F. Pollitz, B. Nagarajan, and R. Bürgmann (2007), Coseismic slip distributions of the 26 December 2004 Sumatra-Andaman and 28 March 2005 Nias earthquakes from GPS static offsets, *Bull. Seism. Soc. Am.,* 97 (1A), S86–S102.

Bassin, C., G. Laske, and G. Masters (2000), The Current Limits of Resolution for Surface Wave Tomography in North America, *EOS Trans AGU*, 81, F897.

Bilek, S. L., K. Satake, and K. Sieh (2007), Introduction to the special issue on the 2004 Sumatra-Andaman earthquake and the Indian Ocean tsunami, *Bull. Seism. Soc. Am.*, 97, S1–S5.

Bird, P. (2003), An updated digital model of plate boundaries, *Geochemistry Geophysics Geosystems*, 4(3), 1027, doi:10.1029/2001GC000252.

Borrero, J. C., R. Weiss, E. A. Okal, R. Hidayat, Suranto, D. Arcas, and V. V. Titov (2009), The tsunami of 12 September 2007, Bengkulu Province, Sumatra, Indonesia: Post-tsunami survey and numerical modeling, *Geophys. J. Int.*, 178, 180–194.

Broerse, T., R. Riva, and B. Vermeersen (2014), Ocean contribution to seismic gravity changes: the sea level equation for seismic perturbations revisited, *Geophys. J. Int.*, 199, 1094–1109, doi: 10.1093/gji/ggu315.

Cambiotti, G., A. Bordoni, R. Sabadini, and L. Colli (2011), GRACE gravity data help constraining seismic models of the 2004 Sumatran earthquake, *J. Geophys. Res.,* 116, B10403, doi:10.1029/2010JB007848.

Cambiotti, G. and R. Sabadini (2012), A source model for the great 2011 Tohoku earthquake (Mw=9.1) from inversion of GRACE gravity data, *Earth & Planet. Sci. Lett.*, 335–336, 72-79.

Cambiotti, G., and R. Sabadini (2013), Gravitational seismology retrieving Centroid-Moment-Tensor solution of the 2011 Tohoku earthquake, *J. Geophys. Res. Solid Earth*, 118, 183–194, doi:10.1029/2012JB009555.

Chen, J. L., C. R. Wilson, and K.-W. Seo (2009), S2 ocean tide aliasing in GRACE time-variable gravity solutions, *J. Geod.,* 83(7), 679–687, doi:10.1007/s00190-008-0282-1.

Chlieh, M., J.P. Avouac, V. Hjorleifsdottir, T. A. Song, C. Ji, K. Sieh, A. Sladen, H. Hebert, L. Prawirodirdjo, Y. Bock, and J. Galetzka (2007), Coseismic Slip and Afterslip of the Great Mw 9.15 Sumatra-Andaman Earthquake of 2004, *Bull. Seism. Soc. Am.*, 97 (1A), S152-S173.

Corana, A., M. Marchesi, C. Martini, and S. Ridella (1987), Minimizing multimodal functions of continuous variables with the 'simulated annealing algorithm', *ACM Transactions on Mathematical Software*, 13, 262-280.

Dahlen, F. A., and Jeroen Tromp (1998), Theoretical Global Seismology, *Princeton University Press*, Princeton, New Jersey.

Dai, C., C. K. Shum, R. Wang, L. Wang, J. Guo, K. Shang, and B. Tapley (2014), Improved constraints on seismic source parameters of the 2011 Tohoku earthquake from GRACE gravity and gravity gradient changes, *Geophys. Res. Lett.,* 41, 1929–1936, doi:10.1002/2013GL059178.

de Linage, C., L. Rivera, J. Hinderer, J.-P. Boy, Y. Rogister, S. Lambotte, and R. Biancale (2009), Separation of coseismic and postseismic gravity changes for the 2004 Sumatra–Andaman earthquake from 4.6 yr of GRACE observations and modelling of the coseismic change by normal-modes summation, *Geophys. J. Int.*, 176, 695–714, doi:10.1111/j.1365-246X.2008.04025.x.

Delescluse, M., N. Chamot-Rooke, R. Cattin, L. Fleitout, O. Trubienko, and C. Vigny (2012), April 2012 intra-oceanic seismicity off Sumatra boosted by the Banda-Aceh megathrust, *Nature*, 490, 240–244.

Duan, X.J., J.Y. Guo, C.K. Shum, and W. van der Wal (2009), On the postprocessing removal of correlated errors in GRACE temporal gravity field solutions, *J. Geodesy*, 83, 1095-1106, DOI 10.1007/s00190-009-0327-0.

Dziewonski, A., and D. L. Anderson (1981), Preliminary reference Earth model, *Phys. Earth Planet. Inter.,* 25, 297–356.

Freymueller, J., J. Dong, and W. Sun (2014), Comparing Calculations of Far-Field Coseismic Deformation, *AGU fall meeting*, San Francisco, California, USA, 15-19 December, 2014.

Fuchs, M. J., J. Bouman, T. Broerse, P. Visser, and B. Vermeersen (2013), Observing coseismic gravity change from the Japan Tohoku-Oki 2011 earthquake with GOCE gravity gradiometry, *J. Geophys. Res. Solid Earth*, 118, 5712–5721, doi:10.1002/jgrb.50381.

Fujii, Y., and K. Satake (2007), Tsunami source of the 2004 Sumatra– Andaman earthquake inferred from tide gauge and satellite data, *Bull. Seism. Soc. Am.*, 97 (1A), S192–S207.

Geist, E. L., V. V. Titov, D. Arcas, F. F. Pollotz, and S. L. Bilek (2007), Implications of the 26 December 2004 Sumatra–Andaman earthquake on tsunami forecast and assessment models for great subduction zone earthquakes, *Bull. Seism. Soc. Am.,* 97 (1A), S249–S270.

Goffe, William L., Gary D. Ferrier, and John Rogers (1994), Global optimization of statistical functions with simulated annealing, *Journal of Econometrics*, 60, 65–99.

Goiginger, H., E. Hoeck, D. Rieser, T. Mayer-Guerr, A. Maier, S. Krauss, R. Pail, T. Fecher, T. Gruber, J.M. Brockmann, I. Krasbutter, W.-D. Schuh, A. Jaeggi, L. Prange, W. Hausleitner, O. Baur, and J. Kusche (2011), The combined satellite-only global gravity field model GOCO02S, *2011 General Assembly of the European Geosciences Union*, Vienna, Austria, April 4-8, 2011.

Guo, J.Y., K. Shang, C. Jekeli, and C. Shum (2015), On the energy integral formulation of gravitational potential differences from satellite-to-satellite tracking, *Celest. Mech. Dyn. Astr,* doi:10.1007/s10569-015-9610-y, in press.

Gusman, A. R., Y. Tanioka, T. Kobayashi, H. Latief, and W. Pandoe (2010), Slip distribution of the 2007 Bengkulu earthquake inferred from tsunami waveforms and InSAR data, *J. Geophys. Res.*, 115, B12316, doi:10.1029/2010JB007565.

Han, S.-C., C. Shum, M. Bevis, C. Ji, and C. Kuo (2006), Crustal dilatation observed by GRACE after the 2004 Sumatra-Andaman earthquake, *Science*, 313(5787), 658–661.

Han, S.-C., J. Sauber, and S. Luthcke (2010), Regional gravity decrease after the 2010 Maule (Chile) earthquake indicates large-scale mass redistribution, *Geophys. Res. Lett*., 37, L23307, doi:10.1029/2010GL045449.

Han, S.-C., J. Sauber, and R. Riva (2011), Contribution of satellite gravimetry to understanding seismic source processes of the 2011 Tohoku-Oki earthquake, *Geophys. Res. Lett.*, 38, L24312, doi:10.1029/2011GL049975.

Han, S.-C., R. Riva, J. Sauber, and E. Okal (2013), Source parameter inversion for recent great earthquakes from a decade-long observation of global gravity fields, *J. Geophys. Res.,* 118, 1240–1267, doi:10.1002/jgrb.50116.

Hayes, G. (2010), Finite fault model, updated results of the Feb. 27, 2010 Mw 8.8 Maule, Chile earthquake, available at: http://earthquake.usgs.gov/earthquakes/eqinthenews/2010/us2010tfan/finite_fault.php. (last accessed January 12 2015).

Hayes, G.P. (2011), Rapid source characterization of the Mw 9.0 off the Pacific coast of Tohoku earthquake, *Earth Planets Space*, 63, 529–534, doi:10.5047/eps.2011.05.012.

Heki, K., and K. Matsuo (2010), Coseismic gravity changes of the 2010 earthquake in central Chile from satellite gravimetry, *Geophys. Res. Lett.,* 37, L24306, doi:10.1029/2010GL045335.

Ji, C., D.J. Wald, and D.V. Helmberger (2002), Source description of the 1999 Hector Mine, California, earthquake, part I: wavelet domain inversion theory and resolution analysis, *Bull. Seism. Soc. Am.,* 92, 1192–1207.

Kanamori, H., and J. W. Given (1981), Use of long-period surface waves for rapid determination of earthquake source parameters, *Phys. Earth Planet. Inter.,* 27, 8–31, doi:10.1016/0031-9201(81)90083-2.

King, M. A., L. Padman, K. Nicholls, P. J. Clarke, G. H. Gudmundsson, B. Kulessa, and A. Shepherd (2011), Ocean tides in the Weddell Sea: New observations on the Filchner-Ronne and Larsen C ice shelves and model validation, *J. Geophys. Res.,* 116, C06006, doi:10.1029/2011JC006949.

Kirkpatrick, S., C.D. Gelatt Jr., and M.P. Vecchi (1983), Optimization by simulated annealing, *Science*, 220, 671–680, doi:10.1126/science.220. 4598.671.

Konca, A. Ozgun, V. Hjorleifsdottir, T. A. Song, J.P. Avouac, D. V. Helmberger, C. Ji, K. Sieh, R. Briggs, A. Meltzner (2007), Rupture kinematics of the 2005, Mw 8.6, Nias-Simeulue earthquake from the joint inversion of seismic and geodetic data, *Bull. Seism. Soc. Am.,* 97 (1A), S307–S322, doi: 10.1785/0120050632.

Konca, A. O., J-P. Avouac, A. Sladen, A. J. Meltzner, K. Sieh, P. Fang, Z. Li, J. Galetzka, J. Genrich, M. Chlieh, D. H. Natawidjaja, Y. Bock, E. Fielding, C. Ji, and D. V. Helmberger (2008), Partial rupture of a locked patch of the Sumatra megathrust during the 2007 earthquake sequence, *Nature*, 456, 631-635, doi:10.1038/nature07572.

Koper, K. D., A. R. Hutko, T. Lay, and O. Sufri (2012), Imaging short-period seismic radiation from the 27 February 2010 Chile (MW 8.8) earthquake by back-projection of P, PP, and PKIKP waves, *J. Geophys. Res.*, 117, B02308, doi:10.1029/ 2011JB008576.

Lay, T., H. Kanamori, C. J. Ammon, M. Nettles, S. N. Ward, R. C. Aster, S. L. Beck, S. L. Bilek, M. R. Brudzinski, R. Butler, H. R. DeShon, G. Ekstrom, K. Satake, and S. Sipkin (2005), The great Sumatra-Andaman earthquake of 26 December 2004, *Science,* 308, 1127–1133.

Lay, T., C. J. Ammon, H. Kanamori, K. D. Koper, O. Sufri, and A. R. Hutko (2010), Teleseismic inversion for rupture process of the 27 February 2010 Chile (Mw 8.8) earthquake, *Geophys. Res. Lett.,* 37, L13301, doi:10.1029/ 2010GL043379.

Lay, T., C. Ammon, H. Kanamori, L. Xue, and M. Kim (2011), Possible large near-trench slip during the 2011 Mw 9.0 off the Pacific coast of Tohoku Earthquake, *Earth Planets Space*, 63, 687–692.

Lay, T., H. Kanamori, C. J. Ammon, K. D. Koper, A. R. Hutko, L. Ye, H. Yue, and T. M. Rushing (2012), Depth-varying rupture properties of subduction zone megathrust faults, *J. Geophys. Res.,* 117, B04311, doi:10.1029/2011JB009133.

Li, J., and W.B. Shen (2011), Investigation of the Co-seismic gravity field variations caused by the 2004 Sumatra-Andaman earthquake using monthly GRACE data, *Journal of Earth Science*, 22, 2, 280-291.

Li, J., and Jianli Chen (2013), Effect of Topography on Coseismic Gravity Changes and Verification from GRACE, *Asia-Pacific Space Geodynamics* (APSG) Symposium, the Ohio State University, Columbus, Ohio, USA, October 14–17, 2013.

Li, Jin, and W.B. Shen (2015), Monthly GRACE detection of coseismic gravity change associated with 2011 Tohoku-Oki earthquake using northern gradient approach, *Earth, Planets and Space*, 67, 1.

Lorito, S., F. Romano, S. Atzori, X. Tong, A. Avallone, J. McCloskey, M. Cocco, and A. Piatanesi (2011), Limited overlap between the seismic gap and coseismic slip of the great 2010 Chile earthquake, *Nat. Geosci.,* 4, 173–177, doi:10.1038/ngeo1073.

Matsuo, K., and K. Heki (2011), Coseismic gravity changes of the 2011 Tohoku-Oki earthquake from satellite gravimetry, *Geophys. Res. Lett.*, 38, L00G12, doi:10.1029/2011GL049018.

McGuire, J., and G. Beroza (2012), A rogue earthquake off Sumatra, *Science*, 336, 1118–1119.

Melachroinos, S., J. Lemoine, P. Tregoning, and R. Biancale (2009), Quantifying FES2004 S_2 tidal model from multiple space-geodesy techniques, GPS and GRACE, over North West Australia, *J. Geod.,* 83(10), 915–923.

Meng, L., J.-P. Ampuero, J. Stock, Z. Duputel, Y. Luo, and V. C. Tsai (2012), Earth-quake in a maze: Compressional rupture branching during the 2012 Mw 8.6 Sumatra earthquake, *Science*, 337, 724–726.

Moore, P., and M. A. King (2008), Antarctic ice mass balance estimates from GRACE: Tidal aliasing effects, *J. Geophys. Res.,* 113, F02005, doi:10.1029/2007JF000871.

Okada, Y. (1985). Surface deformation due to shear and tensile faults in a half-space, *Bull. Seism. Soc. Am.,* 75, 1135-1154.

Okada, Y. (1992), Internal deformation due to shear and tensile faults in a half-space, *Bull. Seism. Soc. Am.,* 82, 1018–1040.

Ozawa, S., T. Nishimura, H. Suito, T. Kobayashi, M. Tobita, and T. Imakiire (2011), Coseismic and postseismic slip of the 2011 magnitude-9 Tohoku-Oki earthquake, *Nature*, 475, 373–376, doi:10.1038/nature10227.

Panet, I., F.F. Pollitz, V. Mikhailov, M. Diament, P. Banerjee, and K. Grijalva (2010), Upper mantle rheology from GRACE and GPS postseismic deformation after the 2004 Sumatra-Andaman earthquake, *Geochem. Geophys. Geosyst.*, 11, Q06008, doi:10.1029/2009GC002905.

Park, J., T. R. A. Song, J. Tromp, E. Okal, S. Stein, G. Roult, E. Clevede, G. Laske, H. Kanamori, P. Davis, J. Berger, C. Braitenberg, M. Van Camp, X. Lei, H. P. Sun, H. Z. Xu, and S. Rosat (2005), Earth's free oscillations excited by the 26 December 2004 Sumatra-Andaman earthquake, *Science,* 308, 1139–1144.

Pollitz, F. (1996), Coseismic deformation from earthquake faulting on a layered spherical Earth, *Geophys. J. Int.,* 125, 1-14.

Pollitz, F. F., et al. (2011a), Coseismic slip distribution of the February 27, 2010 Mw 8.8 Maule, Chile earthquake, *Geophys. Res. Lett.,* 38, L09309, doi:10.1029/2011GL047065.

Pollitz, F. F., R. Bürgmann, and P. Banerjee (2011b), Geodetic slip model of the 2011 M9.0 Tohoku earthquake, *Geophys. Res. Lett.*, 38, L00G08, doi:10.1029/2011GL048632.

Poisson B., C. Oliveros, R. Pedreros (2011), Is there a best source model of the Sumatra 2004 earthquake for simulating the consecutive tsunami? *Geophys. J. Int.,* 185, 1365–1378.

Rhie, J., D. Dreger, R. Bürgmann, and B. Romanowicz (2007), Slip of the 2004 Sumatra–Andaman earthquake from joint inversion of long period global seismic waveforms and GPS static offsets, *Bull. Seism. Soc. Am.,* 97 (1A), S115–S127.

Royer, J.-Y. (2012), Earth science: When an oceanic tectonic plate cracks, *Nature*, 490(7419), 183–185.

Sato, M., T. Ishikawa, N. Ujihara, S. Yoshida, M. Fujita, and A. Asada (2011), Displacement above the hypocenter of the 2011 Tohoku-Oki earthquake, *Science*, 332, 1395, doi:10.1126/science.1207401.

Seno, T., and K. Hirata (2007), Did the 2004 Sumatra–Andaman earthquake involve a component of tsunami earthquakes? *Bull. Seism. Soc. Am.,* 97, no. 1A, S296–S306.

Shang, K., .J.Y. Guo, C.K. Shum, C. Dai, and J. Luo (2015), GRACE time-variable gravity field recovery using an improved energy balance approach, *Earth Planet. Sci. Lett.,* under review.

Shao, G., X. Li, C. Ji, and T. Maeda (2011), Focal mechanism and slip history of the 2011 Mw 9.1 off the Pacific coast of Tohoku earthquake, constrained with teleseismic body and surface waves, *Earth Planets Space*, 63, 559–564, doi:10.5047/eps.2011.06.028.

Shao, G., X. Li and C.Ji (2012), Preliminary Result of the Apr 11, 2012 Mw 8.64 sumatra Earthquake,http://www.geol.ucsb.edu/faculty/ji/big_earthquakes/2012/04/10/sumatra.html. (last accessed January 13, 2015).

Simons, F., F. Dahlen, and M. Wieczorek (2006), Spatiospectral concentration on a Sphere, *SIAM Review*, 48(3), 504–536, doi:10.1137/S0036144504445765.

Simons, F. J., J. C. Hawthorne, and C. D. Beggan (2009), Efficient analysis and representation of geophysical processes using localized spherical basis functions, *Proc. SPIE*, 7446, 74460G, doi:10.1117/12.825730.

Simons, M., et al. (2011), The 2011 magnitude 9.0 Tohoku-Oki earthquake: Mosaicking the megathrust from seconds to centuries, *Science*, 332, 1421–1425, doi:10.1126/science.1206731.

Stein, S., and E. A. Okal (2005), Speed and size of the Sumatra earthquake, *Nature,* 434, 581–582.

Sun, W., Okubo, S., (1993), Surface potential and gravity changes due to internal dislocations in a spherical earth— I. Theory for a point dislocation, *Geophys. J. Int.*, 114, 569–592.

Swenson, S., and J. Wahr (2006), Post-processing removal of correlated errors in GRACE data, *Geophys. Res. Lett.*, 33, L08402.

Takahashi, N., S. Kodaira, T. Tsuru, J.O. Park, Y. Kaneda, K. Suyehiro, H. Kinoshita, S. Abe, M. Nishino, R. Hino (2004), Seismic structure and seismogenesis off Sanriku region, northeastern Japan, *Geophys. J. Int.*, 159, 129-145.

Tanioka, Y., Yudhicara, T. Kusunose, S. Kathiroli, Y. Nishimura, S. Iwasaki, and K. Satake (2006), Rupture process of the 2004 great Sumatra-Andaman earthquake estimated from tsunami waveforms, *Earth Planets Space*, 58, 203–209.

Tanioka, Y., and K. Satake (1996), Tsunami generation by horizontal displacement of ocean bottom, *Geophys. Res. Lett.*, 23, 891–894.

Tapley, B. D., S. Bettadpur, J. C. Ries, P. F. Thompson, and M. M. Watkins (2004), GRACE measurements of mass variability in the Earth system, Science, 305, 503–505.

Uzun, Sibel (2013), Estimating Parameters of Subsurface Structures from Airborne Gravity Gradiometry Data Using a Monte-Carlo Optimization Method, *OSU Report No. 506*, Div. of Geodetic Sciences, School of Earth Sciences, The Ohio State University, Columbus, OH, USA.

Vigny, C., W. Simons, S. Abu, R. Bamphenyu, C. Satirapod, N. Choosakul, C. Subarya, A. Socquet, K. Omar, H. Abidin, and B. Ambrosius (2005), GPS in SE Asia provides unforeseen insights on the 2004 megathrust earthquake, *Nature*, 436, 201–206.

Vigny, C., et al. (2011), The 2010 Mw 8.8 Maule megathrust earthquake of central Chile, monitored by GPS, *Science*, 332, 1417–1421, doi:10.1126/science.1204132.

Wang, L., C. Shum, F. Simons, A. Tassara, K. Erkan, C. Jekeli, A. Braun, C. Kuo, H. Lee, and D. Yuan (2012a), Coseismic slip of the 2010 Mw 8.8 Great Maule, Chile, earthquake quantified by the inversion of GRACE observations, *Earth & Planet. Sci. Lett.*, 335–336, 167–179.

Wang, L., C. Shum, F. Simons, B. Tapley, and C. Dai (2012b), Coseismic and postseismic deformation of the 2011 Tohoku-Oki earthquake constrained by GRACE gravimetry, *Geophys. Res. Lett.*, 39, L07301, doi:10.1029/2012GL051104.

Wang, L., C. Shum, and C. Jekeli (2012c), Gravitational gradient changes following the 2004 December 26 Sumatra–Andaman Earthquake inferred from GRACE, *Geophys. Jl. Inter.*, 191 (3), 1109–1118, doi: 10.1111/j.1365-246X.2012.05674.x

Wang, Lei (2012), Coseismic Deformation Detection and Quantification for Great Earthquakes Using Spaceborne Gravimetry, *OSU Report No. 498*, Div. of Geodetic Sciences, School of Earth Sciences, The Ohio State University, Columbus, OH, USA.

Wang, R., F. Lorenzo-Martin, and F. Roth (2006), PSGRN/PSCMP - a new code for calculating co- and post-seismic deformation, geoid and gravity changes based on the viscoelastic-gravitational dislocation theory, *Computers and Geosciences*, 32, 527-541. DOI:10.1016/j.cageo.2005.08.006.

Wang, R., S. Parolai, M. Ge, M. Ji, T.R. Walter and J. Zschau (2013), The 2011 Mw 9.0 Tohoku-Oki Earthquake: Comparison of GPS and Strong-Motion Data, *Bull. Seism. Soc. Am.*, 103 (2B), 1336-1347, doi:10.1785/0120110264.

Wei, Shengji, R. Graves, D. Helmberger, J.P. Avouac, and J. Jiang (2012), Sources of shaking and flooding during the Tohoku-Oki earthquake: A mixture of rupture styles, *Earth & Planet. Sci. Lett.*, 333–334, 91–100.

Wessel, P., and W. H. F. Smith (1991), Free software helps map and display data, *Eos Trans. AGU*, 72(41), 441, doi:10.1029/90EO00319.

Wieczorek, M.A., and F.J. Simons (2005), Localized spectral analysis on the sphere, *Geophys. J. Int.*, 162, 655–675.

Yadav, R. K., B. Kundu, K. Gahalaut, J. Catherine, V. K. Gahalaut, A. Ambikapthy, and M. S. Naidu (2013), Coseismic offsets due to the 11 April 2012 Indian Ocean earthquakes (Mw 8.6 and 8.2) derived from GPS measurements, *Geophys. Res. Lett.,* 40, 3389–3393, doi:10.1002/grl.50601.

Yue, H., T. Lay, and K. Koper (2012), En échelon and orthogonal fault ruptures of the 11 April 2012 great intraplate earthquakes, *Nature*, 490, 245–249, doi:10.1038/nature11492.

Appendix A. Depth of the Slip Model

About the coordinates of fault patches given by GPS measurements, the depth of each sub-fault is relative to the average elevation of GPS stations [*Ji et al.*, 2002]. The reason is that during the inversion for fault parameters using GPS measurements, a one-dimensional velocity model is used, which means all GPS stations are considered located on the same spherical surface (horizon plane) and the fault geometry is built based on the same assumption (personal communication with Shengji Wei, Caltech). In a horizontal flat Earth model, depth is relative to the horizontal plane. When we apply this to a spherical earth model, this depth would represent the radial distance from each fault patches' location to its radial surface projection. Since the provided fault segments' depth is relative to the average elevation of GPS stations that being used, these fault patches' depth needs to be adjusted to be relative to ocean floor for modeling the gravity change on sea floor due to the solid earth deformation.

We can first compute the average geocentric radial distance of Japan GPS stations, R_{GPS}, which is the reference surface of the fault model. Then the radial distance of the fault patch is, $R_{GPS} - dep$, where dep is the depth of each fault patch of the given slip distribution model inverted from GPS data. As shown in Figure A.1, the slip's depth relative to ocean bottom, dep_{ob}, can be calculated as: $dep_{ob} = R_{ocean\ bottom} - (R_{GPS} - dep) = dep - (R_{GPS} - R_{ocean\ bottom})$, where $R_{ocean\ bottom}$ is the radial distance of ocean bottom. Assume GPS stations are located on the geoid, i.e. $R_{GPS} = R_{Geoid}$, we have

$$dep_{ob} = dep - h_{ocean\ thickness} \tag{A.1}$$

where $h_{ocean\ thickness}$ is the ocean thickness, $h_{ocean\ thickness} = R_{Geoid} - R_{ocean\ bottom}$. R_{Geoid} is the radial distance of the geoid at the fault patch location.

For the upward continuation of the gravity change from the ocean floor to Earth's semi-major axis, the geocentric distance of ocean bottom needs to be calculated. We first compute the geocentric distance of points on the Earth ellipsoid over the fault area, then compute the radial distance of the ocean bottom. Given the geocentric coordinate of the epicenter (e.g. longitude as 142.8°, latitude, φ_c, as 38.05°, depth, 24 km, http://tectonics.caltech.edu/slip_history/2011_taiheiyo-oki/), the geocentric distance of the radial projection of the epicenter onto the WGS84 (World Geodetic System 1984) ellipsoid can be computed as:

$$R_{ellipsoid} = \sqrt{x^2 + z^2}$$

Where,

$$x = a\cos\varphi \Big/ \sqrt{1 - e^2 \sin^2\varphi}\ ,\quad z = a\left(1 - e^2\right)\sin\varphi \Big/ \sqrt{1 - e^2 \sin^2\varphi}$$

φ is the geodetic latitude of the radial projection of the epicenter on the ellipsoid, which can be computed from its geocentric latitude, $\tan\varphi = \tan\varphi_c / \left(1 - e^2\right)$. a is the semi-major axis, and e is the first eccentricity of the Earth ellipsoid.

Then the geocentric distance of the local geoid at the fault region is: $R_{Geoid} = R_{ellipsoid} + N$, where N is the geoid undulation. Neglecting the geoid undulation, the geocentric distance of ocean bottom would be:

$$R_{ocean\ bottom} = R_{Geoid} - h_{ocean\ thickness} = R_{ellipsoid} - h_{ocean\ thickness} \tag{A.2}$$

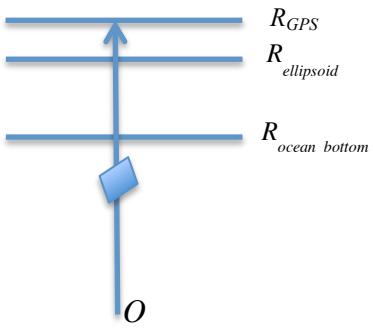

Figure A.1. The diagram for different geocentric radial distances

Appendix B. Derivation of Gravity Disturbance and Gravity Gradient Tensor Disturbance from Spherical Harmonic Coefficients

The disturbing gravitational potential, *T*, difference between GRACE L2 product and the GOCO02S reference field, can be computed by

$$T = \frac{GM}{R}\left(\sum_{n=2}^{\infty}\sum_{m=0}^{n}\left(\frac{R}{r}\right)^{n+1}\left(\Delta\overline{C}_{nm}\cos m\lambda + \Delta\overline{S}_{nm}\sin m\lambda\right)\overline{P}_{nm}\left(\cos\theta\right)\right) \tag{B.1}$$

GM the gravitational constant multiplied by the mass of the Earth, m^3/s^2.

R the Earth's semi-major axis as defined in GRACE L2 solution, 6378136.3 m.

$\Delta\overline{C}_{nm}$ and $\Delta\overline{S}_{nm}$ the spherical harmonic coefficients difference, unitless.

$\overline{P}_{nm}$ the fully normalized associated Legendre function, unitless.

r the radius, meter.

θ the colatitude, degree.

λ the longitude, degree.

Based on equation (B.1), the first derivatives of *T* with respect to r, θ and λ can be easily derived:

$$T_r = -\frac{GM}{R^2}\left(\sum_{n=2}^{\infty}(n+1)\left(\frac{R}{r}\right)^{n+2}\sum_{m=0}^{n}\left(\Delta\overline{C}_{nm}\cos m\lambda + \Delta\overline{S}_{nm}\sin m\lambda\right)\overline{P}_{nm}\left(\cos\theta\right)\right) \tag{B.2}$$

$$T_\theta = -\frac{GM}{R}\left(\sum_{n=2}^{\infty}\left(\frac{R}{r}\right)^{n+1}\sum_{m=0}^{n}\left(\Delta\overline{C}_{nm}\cos m\lambda + \Delta\overline{S}_{nm}\sin m\lambda\right)\overline{P}'_{nm}\left(\cos\theta\right)\sin\theta\right) \tag{B.3}$$

$$T_{\lambda}=\frac{GM}{R}\left(\sum_{n=2}^{\infty}\left(\frac{R}{r}\right)^{n+1}\sum_{m=0}^{n}m\left(-\Delta\overline{C}_{nm}\sin m\lambda+\Delta\overline{S}_{nm}\cos m\lambda\right)\overline{P}_{nm}\left(\cos\theta\right)\right) \tag{B.4}$$

And the second derivatives of T with respect to r,θ and λ are:

$$T_{rr}(r,\theta,\lambda)=\frac{GM}{R^{3}}\left(\sum_{n=2}^{\infty}(n+1)(n+2)\left(\frac{R}{r}\right)^{n+3}\sum_{m=0}^{n}\left(\Delta\overline{C}_{nm}\cos m\lambda+\Delta\overline{S}_{nm}\sin m\lambda\right)\overline{P}_{nm}\left(\cos\theta\right)\right) \tag{B.5}$$

$$T_{r\theta}(r,\theta,\lambda)=\frac{GM}{R^{2}}\left(\sum_{n=2}^{\infty}(n+1)\left(\frac{R}{r}\right)^{n+2}\sum_{m=0}^{n}\left(\Delta\overline{C}_{nm}\cos m\lambda+\Delta\overline{S}_{nm}\sin m\lambda\right)\overline{P}'_{nm}\left(\cos\theta\right)\sin\theta\right) \tag{B.6}$$

$$T_{r\lambda}(r,\theta,\lambda)=\frac{GM}{R^{2}}\left(\sum_{n=2}^{\infty}(n+1)\left(\frac{R}{r}\right)^{n+2}\sum_{m=0}^{n}m\left(\Delta\overline{C}_{nm}\sin m\lambda-\Delta\overline{S}_{nm}\cos m\lambda\right)\overline{P}_{nm}\left(\cos\theta\right)\right) \tag{B.7}$$

$$T_{\theta\theta}(r,\theta,\lambda)=\frac{GM}{R}\left(\sum_{n=2}^{\infty}\left(\frac{R}{r}\right)^{n+1}\sum_{m=0}^{n}\left(\Delta\overline{C}_{nm}\cos m\lambda+\Delta\overline{S}_{nm}\sin m\lambda\right)\left(\overline{P}''_{nm}\left(\cos\theta\right)\sin^{2}\theta-\overline{P}'_{nm}(\cos\theta)\cos\theta\right)\right) \tag{B.8}$$

$$T_{\theta\lambda}(r,\theta,\lambda)=\frac{GM}{R}\left(\sum_{n=2}^{\infty}\left(\frac{R}{r}\right)^{n+1}\sum_{m=0}^{n}m\left(\Delta\overline{C}_{nm}\sin m\lambda-\Delta\overline{S}_{nm}\cos m\lambda\right)\overline{P}'_{nm}\left(\cos\theta\right)\sin\theta\right) \tag{B.9}$$

$$T_{\lambda\lambda}(r,\theta,\lambda)=-\frac{GM}{R}\left(\sum_{n=2}^{\infty}\left(\frac{R}{r}\right)^{n+1}\sum_{m=0}^{n}m^{2}\left(\Delta\overline{C}_{nm}\cos m\lambda+\Delta\overline{S}_{nm}\sin m\lambda\right)\overline{P}_{nm}\left(\cos\theta\right)\right) \tag{B.10}$$

The gravity disturbance vector in the local north-east-down (NED) frame can be expressed as (equation 2.32 in *Chen* [2007]):

$$g_{N}=-T_{\theta}/r=GM/R^{2}\left(\sum_{n=2}^{\infty}\left(R/r\right)^{n+2}\sum_{m=0}^{n}\left(\Delta\overline{C}_{nm}\cos m\lambda+\Delta\overline{S}_{nm}\sin m\lambda\right)\overline{P}'_{nm}\left(\cos\theta\right)\sin\theta\right) \tag{B.11}$$

$$g_{E}=T_{\lambda}/(r\sin\theta)=GM/(R^{2}\sin\theta)\left(\sum_{n=2}^{\infty}\left(R/r\right)^{n+2}\sum_{m=0}^{n}m\left(-\Delta\overline{C}_{nm}\sin m\lambda+\Delta\overline{S}_{nm}\cos m\lambda\right)\overline{P}_{nm}\left(\cos\theta\right)\right) \tag{B.12}$$

$$g_{D}=-T_{r}=GM/R^{2}\left(\sum_{n=2}^{\infty}(n+1)\left(R/r\right)^{n+2}\sum_{m=0}^{n}\left(\Delta\overline{C}_{nm}\cos m\lambda+\Delta\overline{S}_{nm}\sin m\lambda\right)\overline{P}_{nm}\left(\cos\theta\right)\right) \tag{B.13}$$

The gravity gradient disturbance (full tensor) in the local pole-oriented frame (LPOF) (the convention of GOCE standard) that is defined as: the *x*-axis is directed to the North,

the *y*-axis to the West, and the *z*-axis upwards, can be further derived as (equation (3) in [*Ditmar and Klees*, 2002]):

$$T_{xx}(r,\theta,\lambda) = T_r(r,\theta,\lambda)/r + T_{\theta\theta}(r,\theta,\lambda)/r^2 \tag{B.14}$$

$$T_{xy}(r,\theta,\lambda) = T_{yx}(r,\theta,\lambda) = \left(-\cot\theta T_\lambda(r,\theta,\lambda) + T_{\theta\lambda}(r,\theta,\lambda)\right)/(r^2\sin\theta) \tag{B.15}$$

$$T_{xz}(r,\theta,\lambda) = T_{zx}(r,\theta,\lambda) = T_\theta(r,\theta,\lambda)/r^2 - T_{r\theta}(r,\theta,\lambda)/r \tag{B.16}$$

$$T_{yy}(r,\theta,\lambda) = T_r(r,\theta,\lambda)/r + \cot\theta T_\theta(r,\theta,\lambda)/r^2 + T_{\lambda\lambda}(r,\theta,\lambda)/(r^2\sin^2\theta) \tag{B.17}$$

$$T_{yz}(r,\theta,\lambda) = T_{zy}(r,\theta,\lambda) = (r\sin\theta)^{-1}\left(T_\lambda(r,\theta,\lambda)/r - T_{r\lambda}(r,\theta,\lambda)\right) \tag{B.18}$$

$$T_{zz}(r,\theta,\lambda) = T_{rr}(r,\theta,\lambda) \tag{B.19}$$

Appendix C. Retrieve Centroid Moment Tensor and Location From Finite Fault Slip Distribution Model

Given a slip distribution model, which has the slip parameters on each fault patch, the centroid moment tensor can be calculated. The centroid moment tensor is the sum of every point source moment tensor on each fault patch.

$$\mathbf{M} = \begin{bmatrix} M_{xx} & M_{xy} & M_{xz} \\ M_{xy} & M_{yy} & M_{yz} \\ M_{xz} & M_{yz} & M_{zz} \end{bmatrix}, \text{ where } M_{xx} = \sum_{i=1}^{ns} M_{xx,i} \tag{C.1}$$

ns is the number of fault patches, $M_{xx,i}$ is the *xx* component of moment tensor for patch *i*. The same summation is done for each component of moment tensor.

The centroid location is computed as the weight sum of every point source location on each fault patch.

$$\varphi = \sum_{i=1}^{ns} \varphi_i M_{0,i} \Big/ \sum_{i=1}^{ns} M_{0,i}\ ,\ \lambda = \sum_{i=1}^{ns} \lambda_i M_{0,i} \Big/ \sum_{i=1}^{ns} M_{0,i}\ ,\ depth = \sum_{i=1}^{ns} depth_i M_{0,i} \Big/ \sum_{i=1}^{ns} M_{0,i} \tag{C.2}$$

φ the latitude of the centroid, degree.

λ the longitude of the centroid, degree.

(φ_i , λ_i , $depth_i$, $M_{0,i}$) is the latitude, longitude, depth, seismic moment of every point source on each fault patch.